Interaction between Organophosphorus and Oxide Surface for Air Pollution Control

by

Eulalia Yuen-Yi Siu

A Dissertation Presented in Partial Fulfillment
of the Requirements for the Degree
Doctor of Philosophy

Approved April 2011 by the
Graduate Supervisory Committee:

Jean M. Andino, Chair
Erica S. Forzani
Kiril Hristovski
David R. Nielsen
Robert Pfeffer

ARIZONA STATE UNIVERSITY

May 2011

ABSTRACT

The release of organophosphorus compounds (OPs) and subsequent exposure to these compounds is of concern to humans and the environment. The goal of this work was to control the concentrations of gaseous OPs through interaction with sorbent oxides. Experimental and computational methods were employed to assess the interactions of dimethyl phosphite (DMHP), dimethyl methylphosphonate (DMMP), dimethyl ethylphosphonate (DMEP), diethyl ethylphosphonate (DEEP), and triethyl phosphate (TEP) with amorphous silica (a-silica), γ-alumina, and monoclinic zirconia (m-zirconia) for applications in air pollution control. Interactions of the selected OPs with a-silica were chosen as a baseline to determine the applicability of the computational predictions. Based on the a-silica results, computational methods were deemed valid for predicting the trends among materials with comparable interactions (e.g. –OH functionality of a-silica interacting with the phosphonyl O atoms of the OPs). Computational evaluations of the interactions with the OPs were extended to the oxide material, m-zirconia, and compared with the results for γ-alumina. It was hypothesized that m-zirconia had the potential to provide for the effective sorption of OPs in a manner superior to that of the a-silica and the γ-alumina surfaces due to the surface charges of the zirconium Lewis acid sites when coordinated in the oxidized form. Based on the computational study, the predicted heats of adsorption for the selected OPs onto m-zirconia were more favorable than those that were predicted for γ-alumina and a-silica. Experimental studies were carried out to confirm these computational results. M-zirconia nanoparticles were

synthesized to determine if the materials could be utilized for the adsorption of the selected OPs. M-zirconia was shown to adsorb the OPs, and the heats of adsorption were stronger than those determined for commercial samples of a-silica. However, water interfered with the adsorption of the OPs onto m-zirconia, thus leading to heats of adsorption that were much weaker than those predicted computationally. Nevertheless, this work provides a first investigation of m-zirconia as a viable sorbent material for the ambient control of the selected gaseous OPs. Additionally, this work represents the first comparative study between computational predictions and experimental determination of thermodynamic properties for the interactions of the selected OPs and oxide surfaces.

ACKNOWLEDGMENTS

First and foremost, I would like to acknowledge my advisor and committee chair, Dr. Jean M. Andino, for her guidance and mentorship. I am grateful for her support on both a professional and a personal level. Her direction has greatly influenced my professional development and prepared me for a successful future. Next, I would like to thank my committee members, Dr. Erica Forzani, Dr. Kiril Hristovski, Dr. Dave Nielsen, and Dr. Robert Pfeffer. They have provided me with helpful and constructive feedback and helped shape my dissertation.

I would like to thank past and present members of the Andino research laboratory, including graduate students Joel Francis, Tingting Gao, Yanmei Song, Donglai Lu, Teresa Sun, Monique Rodriguez, Selisa Rollins, Brian Clevinger, Jonathan Pham, Jan Wuttig, and undergraduate students Akezhi Samuel Jo-Madugu, Dave Latshaw, and Abel Cardenas for their support. I would also like to express my gratitude to Fred Pena, David Wright, Tim Karcher, Si Phrasavath, and other chemical engineering faculty members for their aid in my research and in my coursework over the years. My deepest appreciation goes to my friends and family who have been extremely supportive throughout my academic journey. In particular, I would like to thank my parents, Ophelia Ngai and K.L. Siu, and my sister Eugenia Siu. Lastly, I would like to acknowledge the NSF GK-12 Fellowship, the NASA Space Grant Fellowship, and the U.S. Air Force for their financial support.

TABLE OF CONTENTS

LIST OF TABLES

Table Page

LIST OF FIGURES

Figure Page

Figure Page

Figure Page

CHAPTER 1

INTRODUCTION

1.1 Problem Statement and Significance

Organophosphorus (OP) compounds are widely used as pesticides in agricultural environments[9,10]; an estimated 70 million pounds of OP pesticides are released annually[11]. Parkinson's disease and health risks in children have been linked to exposure to OP compounds in agricultural communities[12,13]. Overexposure can lead to the inhibition of acetylcholinesterase and result in the accumulation of the neurotrasmitting agent acetylcholine[14]. The effects of acetylcholine accumulation include neurological, neuropsychological, and neurophysiological dysfunctions[15]. As a result, OP compounds have also been employed as nerve agents in chemical warfare. Regardless of the intended uses, the release of OP compounds are of great concern, especially when one considers their toxicities in combination with their other characteristics (e.g. volatility, persistence, reactivity) [16].

OP compounds are semivolatile[17]. Upon release, they can persist in the lower atmosphere for significant time periods. As an example, the OP compound dimethyl methylphosphate has a reported gas-phase rate constant of 1.11×10^{-11} cm^3 $molecule^{-1}$ s^{-1} at 298 K with respect to atmospheric reactions with hydroxyl radicals[18]. This corresponds to a tropospheric lifetime of 1.04 days, given a hydroxyl radical concentration of 10^6 molecules cm^{-3} [19]. Although other OP compounds have different lifetimes, it is the atmospheric persistence of the smaller OPs, together with their volatility that permits these compounds to be dispersed by natural transport mechanism (e.g. wind) from the site of release[20].

Additionally, it is important to note that the released OPs are subject to reaction in the atmosphere. The primary decomposition reactions of gaseous OPs can lead to the formation of hazardous secondary species. For example, the reaction of dichlorvos, a widely used and highly toxic insecticide, leads to the formation of phosgene, a stable and highly toxic secondary species[9]; the reaction of dimethyl methylphosphate leads to the formation of pollutants such as carbon monoxide, in addition to other stable and undesirable phosphorous-containing and non-phosphorous-containing products (e.g. $CH_3OP(O)(CH_3)OH$ and formaldehyde, respectively)[21].

The control of gas-phase OPs is particularly challenging given the low concentrations that are needed to produce adverse effects and are present in the ambient (i.e. pg/m^3 to ng/m^3 of air). For comparison, concentrations that are typically found in the aqueous phase (e.g. rain, fog, wastewater) are in the ng/L to μg/L range, i.e. three to six orders of magnitude higher than the highest gas-phase concentration[20]. The ability to control the presence of gaseous OP compounds at the point of release as opposed to after the point at which they have dispersed and reduced to even lower concentrations can greatly reduce the adverse impacts on humans and on air quality.

The goal of this work is to control the concentrations of gaseous OPs through interaction with sorbent materials. The effectiveness of the sorbent materials are investigated through closely coupled computational and experimental techniques. The computational results provide a basis for predicting the chemical interactions

of different OP/sorbent pairs and ultimately for selecting the base sorbent material for synthesis and eventual use in controlling ambient OP concentrations.

1.2 Background

The interactions of OPs with organic and inorganic materials have been investigated in previous studies[22-107]. In particular, these studies are primarily focused on dimethyl methylphosphonate (DMMP) as the representative molecule for OP compounds. However, a majority of these studies are limited to qualitative evaluations to answer questions such as whether interactions occurred, at what sites, and whether decomposition occurred. Some studies were able to categorize the interaction mechanisms into either weakly reversible physisorption or strongly irreversible chemisorption[23,24,25]. However, published papers utilize different measures to classify the strength of interaction. For example, "strong" interactions may be indicated by a higher amount of adsorption, evidence for a reaction, or through the magnitude of an IR shift. These conclusions were strictly qualitative since they did not differentiate between the varying energies of physisorption and chemisorption (which span more than an order of magnitude). Hence, determining the energies of interaction would allow for a quantitative comparison of materials using the same basis. The available literature on both organic and inorganic materials are reviewed in the following sections.

1.2.1 Inorganic Materials

Inorganic materials that have been evaluated for the interactions with OPs include carbonaceous materials, metals, metalloids, and oxides. These materials are modified (i.e. doped and functionalized) in some cases.

1.2.1.1 Carbon

Carbonaceous materials in the form of single wall carbon nanotubes, modified single wall carbon nanotubes, activated carbon, and impregnated activated carbon have been investigated[22-23]. Studies on the interaction of dimethyl methylphosphonate (DMMP) with single wall carbon nanotubes concluded that a reversible interaction occurred between the P=O group of the OP molecule and the surface of the carbon nanotubes. The interaction was attributed to the partial negative charge on the phosphonyl O atom[22,26,27]. The reversible interaction suggested weak binding (e.g. physisorption) between the OP and the sorbent material. The performance of modified single wall carbon nanotubes for interaction with DMMP was also investigated. Single wall carbon nanotubes modified with the fluorinated substituent, hexafluroisopropanol (HFIP), was reported to form hydrogen bonds with the surface bound HFIP[28,29]. Hydrogen bonding is also characterized as a weaker physisorption process (as compared to chemisorption)[30,31]. Activated carbon materials, either unmodified or modified with chromium, copper, silver, and triethylenediamine, were shown to exhibit an affinity for DMMP[23,32,33]. In the study of the interaction between DMMP and activated carbon impregnated with Cu(II) 1,1,1,5,5,5-hexafluoroacetylacetonate,

the DMMP strongly interacted with (i.e. was chemisorbed to) the surface. These conclusions were indicated by the higher uptake of DMMP onto the Cu impregnated carbon as compared to the unmodified activated carbon of a higher surface area, as well as by the formation of reaction products[23].

1.2.1.2 Metals and metalloids

Pure metalloids or modified metals with surface functionality have also been utilized in a few studies[34,35]. Porous silicon was investigated for its ability to interact with OPs such as DMMP, diethyl ethylphosphonate (DEEP), and triethyl phosphonate (TEP)[34]. Capillary condensation of these OPs occurred in the pores of the material, yet the strength of interaction was not reported[34]. Hydrogen bonding was reported for the interaction of DMMP with gold surfaces that were modified with -OH and -COOH tail groups[36,37,35]. Stronger hydrogen bonding occurred between the OPs studied and the gold modified with the –COOH tail group, and weaker hydrogen bonding was observed with the –OH tail group. The comparison of "stronger" versus "weaker" was made based on the differences noted in the IR shifts of the P=O feature. The OP surface interactions with the gold modified with the $–CH_3$ tail groups were relatively lower than with the other modified gold surfaces[36,37,35].

1.2.1.3 Oxides

The utility of oxides have been investigated extensively; oxides have been utilized by themselves, as mixed oxides, doped with metal, as zeolites, and hybridized with organics.

Pure oxides that have been reported to interact with OPs include Al_2O_3, TiO_2, SiO_2, WO_3, Y_2O_3, CeO_2, FeO, CuO, In_2O_3, SnO_2, and MgO. Both physisorption and chemisorption of DMMP onto Al_2O_3 have been reported at room temperature[38,39,40,41,24]. Chemisorption was confirmed by the formation of an Al-O-P bond[39]. According to Mitchell et al., physisorption occurred with surface –OH groups and chemisorption occurred with Al Lewis acid sites[41,24]. Physisorption and chemisorption were also observed for the interaction between TiO_2 and OPs including DMMP, TMP, and sarin at room temperature[42,43,44,45,46,47,48,49,50,51]. The extent of chemisorption was dependent upon the number of active sites which were dehydrated on the TiO_2 surface[44,46]. Samples which were heated to higher temperatures led to more dehydrated surfaces with a higher occurrence of unassociated –OH sites. The OP compounds chemisorb on these unassociated –OH sites[44,46]. Physisorption of OP compounds onto SiO_2 has been reported, except for in one case where the surface of SiO_2 was heavily hydrated[52,53,54,55]. The physisorption of DMMP onto SiO_2 occurred via the two methoxy O atoms on DMMP, and the interaction was concluded to be fast and reversible when the material was heated above 150°C[52,53,55]. In the case of WO_3, the extent of physisorption as opposed to chemisorption when exposed to DMMP and TMP was dependent upon the temperature at which the gas and the surface interacted[56,57,58,59,60,61,62,63]. At 10°C, reversible interaction of DMMP with WO_3 was reported; increased temperatures (e.g. up to 400°C) led to chemisorption coupled with decomposition[56,57,58,63]. The OP/WO_3 interaction involved adsorption via the P=O functionality with a surface water layer, W

Lewis acid sites, or –OH Bronsted acid sites[59,60,61,62]. In the case of Y_2O_3, CeO_2 and FeO, only the chemisorption of DMMP was observed, and these interactions at room temperature led to decomposition[63,64,65,66,67,68]. For these oxides, chemisorption of the OP was also expected to occur at temperatures higher than room temperature[63]. For some oxides, interactions with OPs have only been investigated at elevated temperatures. CuO and In_2O_3 were investigated at 400°C. Poor recovery of the material was reported after exposure to OPs, thus suggesting that chemisorption occurred at the elevated temperature[63]. Similarly, SnO_2 demonstrated chemisorption of DMMP at temperatures of 400°C and 500°C[63,69,70]. In the case of MgO, chemisorption coupled with decomposition of DMMP, TEP, and trimethyl phosphonate (TMP) occurred at 150°C[71].

Selected oxides have been mixed and investigated for their ability to interact with OPs. CeO_2 and FeO were mixed, and their ability to attract OP compounds was compared with the performance of the pure oxide materials[66,67]. OP compounds were able to chemisorb onto the pure oxide materials, and decomposition of the OPs was detected. When the oxides were mixed at room temperature, the decomposition of DMMP was enhanced. Additional studies on other mixed oxides were restricted to elevated temperatures. SnO_2 and ZnO were mixed with oxides such as MoO_3, Sb_2O_3, NiO, Co_3O_4, Nb_2O_5, CaO, In_2O_3 and MgO. DMMP was observed to interact with all of the mixed oxides at 350 or 400°C[72,73,74,75]. As indicated previously, the chemisorption of DMMP onto pure SnO_2 at elevated temperatures was observed. The physisorption of DMMP at elevated temperatures was observed when SnO_2 was mixed with MoO_3 or Sb_2O_3[72,73].

Alternately, mixed SnO_2 / CaO and SnO_2 / MgO enhanced the decomposition of DMMP [75]. Chemisorption coupled with decomposition of DMMP was also concluded for mixed ZnO/CaO and ZnO/MgO[75].

Materials such as copper clusters, gold nanoparticles, mixed gold and platinum, and platinum have been supported on the surface of TiO_2 and tested for their ability to attract OPs to the surface[76,77,78]. As indicated previously, several OP compounds were found to physisorb and chemisorb to the pure TiO_2, and the extent of chemisorption was dependent upon the degree of dehydration of the surface. Chemisorption coupled with decomposition was the only interaction reported for DMMP onto TiO_2 doped with metals[76,77,78]. In the case where TiO_2 was doped with gold, mixed gold and platinum, and platinum, chemisorption of the OP was reported for temperatures as low as 100K[78].

The interactions of DMMP with the zeolites, NaY and ZSM-5, have also been investigated [79,80,81]. Similar to other oxides, both NaY and ZSM-5 were used in their pure zeolite forms or modified in an attempt to enhance their performance[79,80,81]. In the case of NaY, physisorption of DMMP was reported; the same conclusions were also drawn for NaY modified with tetrapropylammonium and with CeO_2[79,81]. Likewise, DMMP interaction with ZSM-5 was also reversible. ZSM-5 modified with silver yielded a similar response[80].

The interactions of DMMP with SiO_2 hybridized with organic materials have also been reported [25,82]. These hybrid organic / inorganic materials exist as Langmuir-

Blodgett films of trisilanolphenyl polyhedral oligomeric silsesquioxane. Once the DMMP gas diffused into the film, the DMMP physisorbed (via hydrogen bonds) onto the inorganic component of the surface [25,82].

1.2.2 Organic Materials

Organic materials that have been studied for their interaction with OPs include polymers, salts, and biological materials.

1.2.2.1 Polymers

Numerous studies have been reported for the utility of polymers for the interactions with OPs; most of these studies surround fluoropolymers and siloxane based polymers[75-87]. Several other non-fluoropolymers and non-siloxane based polymers have also been investigated[88-93].

OPs have also been reported to interact with fluoropolymers such as fluoropolyol, poly(vinylidene fluoride), and fluoro-modified polymers such as fluoroalcohol-containing organic polymers, silicon based fluoroalcohol, and fluorinated-phenol polymers [83,84,85,86,87,88,89,90]. In all of these studies, reversible physisorption involving hydrogen bonding between the OPs and the fluoroalcohol or fluorinated groups were reported. These interactions between the OPs and the surfaces were reportedly stronger than those that were observed for the non-fluoropolymer, polymethylmethacralate (PMMA)[88].

In the case of siloxane based polymers, literature exists for the interaction of DMMP with o-allyl phenol group functionalized polysiloxane, poly{methyl[3-(2-

hydroxy-3,4-difluoro)phenyl] propyl siloxane}, co-poly(hydroxy-terminated silicone divinylbenzene), and polydimethylsiloxanes[91,92,93,94,95]. Interactions of DMMP with siloxane based polymers were found to be reversible, and desorption upon heating was observed[94].

The interactions of OPs with non-fluoropolymers and non-siloxane based polymers such as allyl-substituted 3,5-bis(trifluoromethyl)phenol polymethylhydrosiloxane polypyrrole, polyamidoamine, hyperbranched polyurea functionalized with 1,5-dansyl (1,5-D), 2,5-dansyl (2,5-D), 2,6-dansyl (2,6-D) and nitrobenzofurazan (NBD) fluorophores, poly(o-phenylenediamine), polyaniline, MEH-PPV, PMMA, and polyethylenimine have been investigated [96,97,98,99,100,101]. All of these polymers indicated a respond to the OPs. The interactions of DMMP with polypyrrole, led to conformational changes in the polymer[97]. The interaction was concluded to be electronic in nature, and likely implied a strong chemisorption process[101]. The DMMP interaction with polyaniline was attributed to hydrogen bonding, and swelling of the polymer was observed[100].

1.2.2.2 Salts

The interactions of OPs with salts such as triflate (trifluoromethylsulfonate) and salts of copper, aluminum, zinc, and iron have been reported in the literature[94-98]. In the study with the ionic liquid salt 1,9-di(3-vinylimidazolium) nonane triflate (trifluoromethylsulfonate), selectivity of the surface towards DMMP amongst a mixture of organics was observed[94]. The ionic liquid salt was successfully utilized for gas chromatography, which implied that a reversible interaction

between the OP and the surface occured[102]. As for the salts of metals (e.g. copper perchlorate), although utilized with various liquid crystals (i.e. 4-cyano-4 -biphenylcarbonitrile, nematic liquid crystal E7, 4 -pentyl-4-cyanobiphenyl, smectic liquid crystal 8CB) as indicators of the interaction, the mechanisms of interaction have been attributed to the OP interaction with the metal ions[103,104,105,106]. The interactions were reportedly reversible and indicative of the physisorption of DMMP and the nerve agents GB, GD, GA, and VX onto the surfaces[103,104,105,106].

1.2.2.3 Biological Materials (Enzymes)

Biological materials (e.g. enzymes) are primarily of interest to applications in OP detection since their application in air pollution control scenarios usually requires stringent environmental controls (e.g. temperature). However, for completeness, the available literature on the interactions of enzymes with OP compounds are also briefly reviewed here. The interactions of various OP compounds such as paraoxon, methyl parathion, diisopropyl phosphorofluoridate, DMMP, and fenitrothion have been investigated with ascorbic acid oxidase (AAO), acetylcholinesterase (AChE)/choline oxidase (CHO) enzymes, and organophosphorous hydrolase (OPH). Interactions with these enzymes were indicated by inhibition of the enzyme, as indicated by changes to the enzyme catalyzed reaction, or decomposition of the OPs into detectable products[107,108,109,110,111,112,113,114]. Although the mechanisms of interaction were not explicitly studied in the available literature, the formation of decomposition

products suggested that a strong interaction must have existed between the OPs and the enzymes[107,108,109,110,111,112,113,114].

1.2.3 Summary

As summarized in Table 1.1, OP compounds have been shown to have an affinity to several different types of surfaces. However, an optimal surface for the control of gaseous OP compounds has yet to be obtained since extensive quantitative information is missing.

Table 1.1. Summary of OP Interactions with Organic and Inorganic Materials

Interacting Surface	OP Compounds	Interaction Type	References
Carbon			
Nanotubes	DMMP	Physisorption	22,26,27
Modified Nanotubes	DMMP	Physisorption	28,29
Activated Carbon	DMMP	Physisorption	23,32,33
Modified Activated Carbon	DMMP	Chemisorption	23,32,33
Metals and Metalloids			
Silicon	DMMP, DEEP, TEP	Unknown	34
Modified Gold	DMMP	Physisorption	35-37
Oxides			
Pure Oxides	DMMP, TEP, TMP	Both	24, 38-71
Mixed Oxides	DMMP	Both	72-75
Modified Pure Oxides	DMMP	Chemisorption	76-78
Zeolites	DMMP	Physisorption	79-81
Oxide-Inorganic Hybrids	DMMP	Physisorption	82
Polymers			
Fluoropolymers	DMMP	Physisorption	83-90
Siloxane-Based Polymers	DMMP	Physisorption	91-95
Other Polymers	DMMP	Unknown or Chemisorption	96-101
Salts			
Other salt	DMMP, TEP, DIMP	Physisorption	102
Metal salts	DMMP, GB, GD, GA, VX	Physisorption	103-106
Biological Materials			
AAO, AChE, CHO, OPH	Nitroaromatic OPs	Decomposition	107-114
Plant esterase complex	DMMP	Unknown	115

1.3 Objective

This work aims to determine an efficient material for the control of gaseous OP compounds by utilizing fundamental quantitative approaches. The approaches undertaken seek to investigate the mode of gaseous OP interactions with the selected surfaces as well as the thermodynamic strengths of interaction by employing closely coupled experimental and computational work. As previously summarized, selected OPs have been shown to interact with oxide materials. Oxides also offer attractive electronic and optical properties[116] that may potentially provide a facile means for the subsequent destruction of the sorbed OPs. Thus, these sorbent materials are used in this work as the starting materials for the control of the gaseous OP compounds. Specifically, the interactions of various OP compounds with three different oxides, i.e. amorphous and hydroxylated silica (a-SiO_2), γ-alumina, and monoclinic zirconia, are determined. The first two oxides were chosen as baseline materials since they were previously investigated from a qualitative perspective with some OP compounds[24,38-41,52-54]. The work outlined in this document using a-SiO_2 extends the previously published work to new OP compounds and provides a baseline example of the physisorption of OP compounds. The work described in this document using γ-alumina provides a baseline example of chemisorption due to the interactions of the OP compounds with the Lewis acid sites of the γ-alumina. It is hypothesized that zirconia has the potential to provide for the effective sorption of OP compounds in a manner that is superior to that of either the silica or the alumina surfaces due to the presence of Zr Lewis acid sites.

The OPs of interest in this work are illustrated in Figure 1.1. DMMP is of interest to this study as it is commonly utilized as a surrogate for sarin, a chemical warfare agent[117]. A comparison between sarin and DMMP appears in Figure 1.2. DMHP, DMEP, DEEP and TEP were chosen to determine the effects of changes in molecular size; an increase in the interaction energetics with an increase in molecular size is hypothesized. This work also aims to determine if this trend is accurately predicted by first principles computational chemistry calculations.

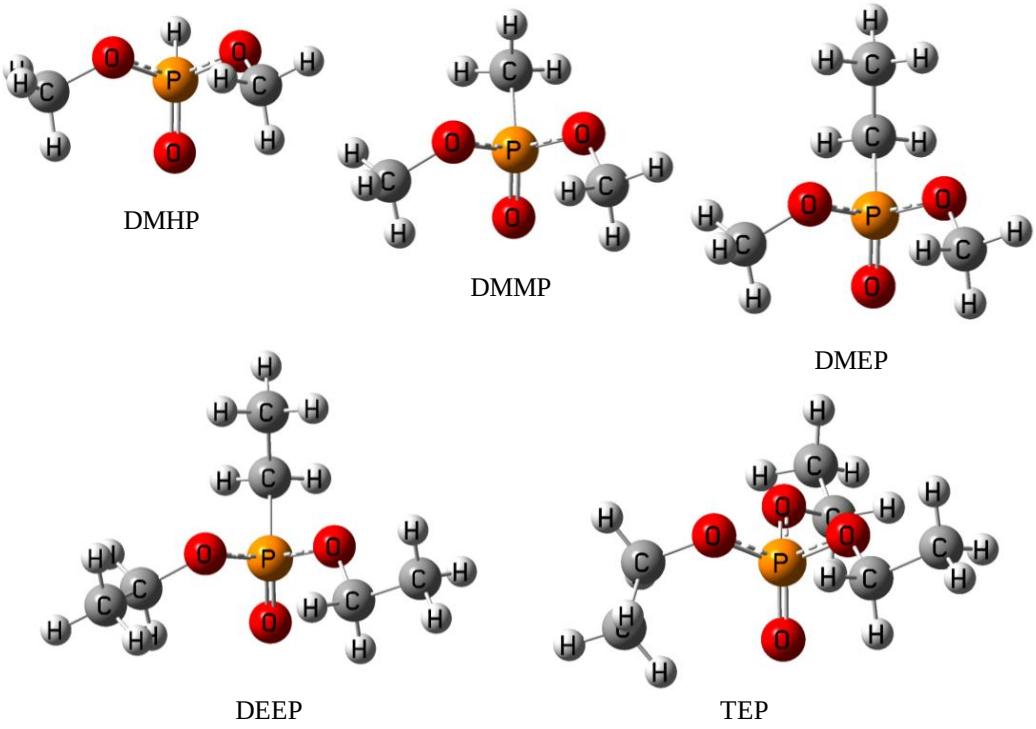

Figure 1.1. OPs of Interest: Dimethyl phosphite (DMHP), Dimethyl Methylphosphonate (DMMP), Dimethyl Ethylphosphonate (DMEP), Diethyl Ethylphosphonate (DEEP), and Triethyl Phosphate (TEP)

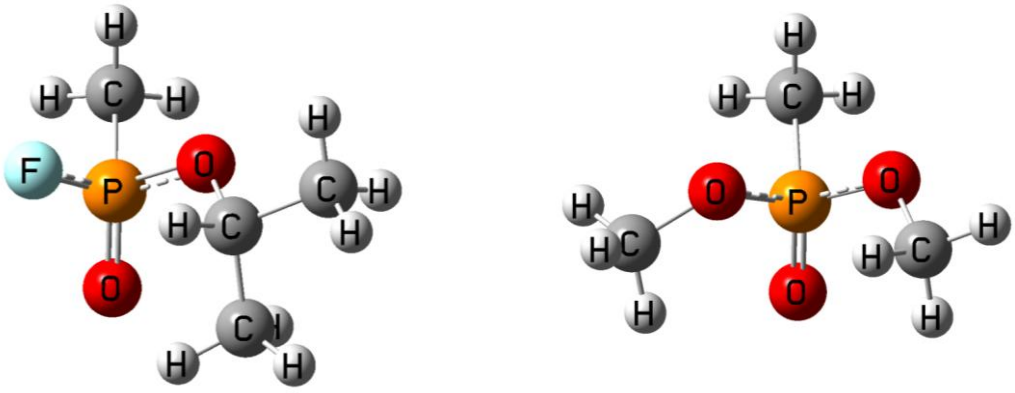

Figure 1.2. Structures of Sarin and DMMP

Empirical data are available for the interactions of DMMP with both silica and alumina, as well as for the interactions of nitroaromatic OPs with zirconia[24,38-41,52-54,118,119,120]. Computational chemistry investigations have been reported for the interactions of DMMP with silica and alumina[1,121,122,123]. However, neither experimental nor computational chemistry investigations of the energetics of DMHP, DMEP, DEEP, and TEP interactions with silica or alumina have been published. Furthermore, the interactions of the five OPs of interest with zirconia have also not been determined. The work herein serves to extend the available database of information for silica and alumina, thereby enhancing the ability to develop structure response predictions for other OPs, while simultaneously devising and characterizing new zirconia based materials for the effective control of gas-phase OP compounds.

1.3.1 Experimental determination of the thermodynamics of interaction

One of the thermodynamic parameter of interest that is associated with the gas / sorbent interaction is the heat of adsorption. The heat of adsorption, ΔH, can be represented by Equation (1.1),

$$\Delta H = R \left[\frac{\delta \ln P}{\delta \left(\frac{1}{T} \right)} \right]_N \qquad \text{(Equation 1.1)}$$

where R is the gas constant, P is the pressure, and T is the absolute temperature. The ΔH value is evaluated at a specific value of N that corresponds to the equilibrium amount of gas that is adsorbed onto the sorbent. A negative ΔH value corresponds to an exothermic process and a positive ΔH implies an endothermic process. Since adsorption is an exothermic process, for any spontaneous interaction between the gas and the sorbent, ΔH is negative. Comparative analyses can be performed by evaluating the magnitude of ΔH. A more negative ΔH is indicative of stronger interactions between the gas and the sorbent. As examples, a ΔH value that is more positive than -20 kcal/mol is associated with physisorption (i.e. weak binding through van der Waals forces or hydrogen bonding), while a ΔH value that is more negative than -20 kcal/mol is associated with chemisorption (i.e. strong binding by formation of ionic or covalent bonds)[30,31].

Based on Equation 1.1, the heat of adsorption can be calculated with knowledge of the equilibrium pressure of the sorbate (P) and the corresponding amount of

gas adsorbed onto the sorbent (N) at various temperatures (T). Adsorption isotherms provide this correlation between P, N, and T.

1.3.1.1 Adsorption isotherm

Adsorption isotherms describe the relationship between the equilibrium amount of gas (sorbate) adsorbed onto the sorbent (i.e. N) and the equilibrium pressure of the sorbate (P) at constant temperature (T). The equilibrium pressure of the sorbate, P, is often expressed in terms of a relative pressure, i.e. *x*, where $x = P/P^o$ and P^o is the saturation vapor pressure of the sorbate. Thus,

$$N = f(\text{relative pressure}, x)|_{\text{temperature,T}}$$

There are six types of adsorption isotherms, as illustrated in Figure 1.3[124,125].

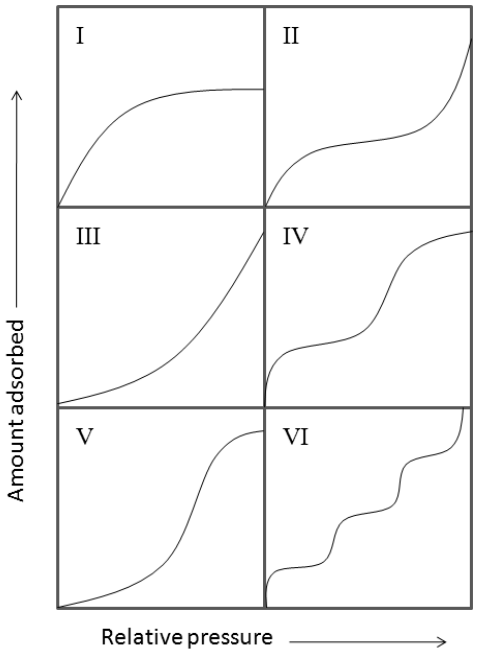

Figure 1.3. Types of Adsorption Isotherm

In brief, a Type I isotherm is representative of monolayer adsorption, where only one layer of sorbate interacts with the sorbent and the surface becomes saturated as the relative pressure, *x*, approaches unity (i.e. no sorbate-sorbate interaction). Type II-VI isotherms are representative of multilayer adsorption which may be observed when both sorbate-sorbent and sorbate-sorbate interactions exist. Specifically, a Type II isotherm represents the monolayer saturation of a surface (i.e. sorbate-sorbent interaction) followed by further adsorption through sorbate-sorbate interaction. A Type III isotherm represents simultaneous sorbate-sorbent and sorbate-sorbate interactions. Type IV and V isotherms represent, respectively, Type II and Type III adsorption behaviors which approach saturation limits as the relative pressure approaches unity. A type VI isotherm represents the type IV isotherm but with incremental steps associated with saturation limits. Comparing the shape of an experimental adsorption isotherm to one of these isotherm types can be useful for deducing the adsorption processes and aid in the selection of an appropriate mathematical expression for fitting experimental data.

Experimental adsorption isotherms are constructed from measurements of the adsorbed amount, N, and the relative pressure, *x*, at constant temperature, T. These measurements can be taken by two different methods. The first method involves the monitoring of the amount of sorbate that leaves the gas phase; a volumetric system is the most direct tool of measurement for this method. For a system of known volume, a direct measurement of the change in the system's pressure can be correlated to the amount of sorbate leaving the gas phase. This technique requires uniform temperature control of the system and an appropriate

equation of state to relate the PVT behavior of the sorbate. The second method involves the monitoring of the amount of sorbate that enters the sorbed phase; this can be done directly with a gravimetric system. For a sorbent with a known mass, the changes in the sample mass upon exposure to the sorbate can be related to the amount of sorbate entering the sorbed phase. Typical responses for these systems are illustrated in Figure 1.4.

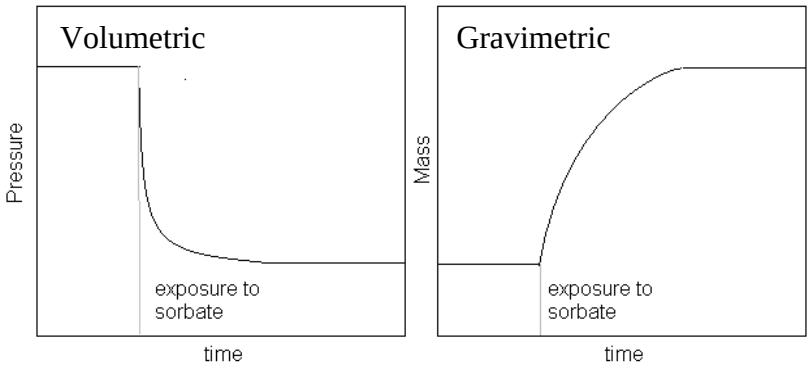

Figure 1.4. Typical Responses for Volumetric and Gravimetric Systems

Other quantities that can be related to the amount of sorbate leaving the gas phase or the amount of sorbate entering the sorbed phase (e.g. changes in the intensity of an infrared absorption band) can also be utilized. However, these alternative techniques require an extensive correction of data to correlate the adsorbed amount to the observed response, thus introducing unnecessary sources of error. Both the monitoring of the sorbate leaving the gas phase or the amount of sorbate entering the sorbed phase can be employed in static (i.e. batch) or dynamic (i.e. continuous) systems. Dynamic systems are often coupled to chromatographic equipment for the analysis of mixtures (e.g. the sorbent can be exposed to a pure

component sorbate, the sorbate can react with the sorbent and release product gases to form a mixture with the original sorbate).

With the availability of adsorption isotherm data at two or more temperatures, the heats of adsorption can be calculated. Note that heat of adsorption could also be measured by calorimetric methods. However, the operation of a calorimeter could be costly and this technique could be limited by the detector sensitivity.

1.3.2 Computational determination of the thermodynamics of interaction

The thermodynamics of interaction can be determined using computational chemistry calculations. Traditionally, computational chemistry generally involves the use of the Schrodinger equation[126], which is a wave equation deduced in an attempt to describe the wave-like behavior of particles[127]. Solutions to the Schrodinger equation provide information on the energy and the quantum mechanical or chemical behavior of a particle[127].

For many-body problems or systems involving multiple electrons, density functional theory has been developed and is increasingly popular for providing an alternative solution to the Schrodinger equation[128]. Density functional theory (DFT) utilizes electron densities (as opposed to wavefunctions) for the chemical and physical description of materials[126].

Many software packages exist to carry out DFT calculations[126]. One of these software packages is Gaussian[129]. Computational determinations of the thermodynamics of interaction (i.e. heats of adsorption) are calculated from partition functions[130]. In brief, contributions from translational, electronic,

vibrational, and rotational motions are accounted for in these partition functions[130]. These motions are used to ultimately calculate the heat of adsorption, assuming idealized behavior[130].

1.4 Overview of the Dissertation Document

In the following chapter, a laboratory-based, quantitative evaluation of the interactions of the five OPs of interest with amorphous silica is presented. A static volumetric technique is utilized. This technique was chosen for its ability to directly monitor the amount of sorbate leaving the gas phase. The experimental results are compared with computational predictions to determine the validity of computational chemistry tools for comparative analyses (i.e. the ability to predict trends accurately). Amorphous silica was chosen for this validation study for its ability to attract OPs without subsequent reaction of the OP, as reported in the literature[52,53]. The non-reactive attraction of the OPs allows the static volumetric technique to be effectively utilized for the adsorption isotherm measurements.

In chapter 3, the utility of zirconia for sorption of the five OPs of interest is investigated using computational chemistry tools. This work represents the first comprehensive study of the interactions of the five gas-phase OPs of interest with zirconia. It is hypothesized that zirconia has the potential to provide for the effective sorption of OP compounds in a manner that is superior to that of the silica surfaces due to the presence of Lewis acid sites and better bonding ability as compared with the Lewis acid sites of alumina due to the surface charge of the zirconium ion when coordinated in the oxidized form. A comparison between the

strengths of interactions between the OPs and zirconia versus the interactions of the OPs with alumina and silica are also presented. Based on the results from the validation study presented in chapter 2, the applicability of the computational results and the expectations for zirconia interactions in a "real" system are commented upon.

Chapter 4 presents the synthesis of a monoclinic zirconia material (the phase modeled by computational chemistry tools in Chapter 3) and its application in OP adsorption. A first attempt at optimizing the hydrothermal synthesis of monoclinic zirconia adsorbent with a high surface area is investigated by analyzing the effects of calcination at various conditions. A first experimental study of the mechanisms of interaction and the heats of adsorption between the OPs of interest and monoclinic zirconia are also presented. Conclusions are drawn on the applicability and challenges associated with the utility of monoclinic zirconia in a "real" environment.

Lastly, in chapter 5, a proposal for future work to enhance the applicability of monoclinic zirconia for the purpose of OP pollution control is presented. Strategies associated with the further optimization of the synthesis of m-zirconia as well as potential ideas which could be explored to overcome challenges associated with the application of the material are proposed.

CHAPTER 2

EXPERIMENTAL AND COMPUTATIONAL CHEMISTRY PREDICTIONS OF ORGANOPHOSPHORUS ADSORPTION ONTO AMORPHOUS SILICA

2.1 Introduction

The utility of amorphous silica for the experimental adsorption of several organophosphorus (OP) compounds, including one of the OPs of interest, dimethyl methylphosphonate (DMMP), has previously been reported[54,52,53]. Early work by Henderson et al.[54] investigated the adsorption of DMMP onto dehydrated and hydroxylated amorphous silica (a-SiO_2) surfaces, partially hydrated and hydroxylated a-SiO_2, and heavily hydrated (i.e. with surface bound H_2O) a-SiO_2 . The samples were dosed with DMMP at 170K and studied by Auger electron spectroscopy in combination with temperature programmed desorption up to 700K. The study concluded that multilayer adsorption of DMMP occurred by physisorption on the partially hydrated/ hydroxylated surface and the dehydrated / hydroxylated surface. In addition, small amounts of decomposition products from the chemisorption of DMMP were observed on the heavily hydrated surface of silica[54].

Kanan and Tripp[52,53] investigated the adsorption of dimethyl methylphosphate (DMMP), trimethyl phosphate (TMP), methyl dichlorophosphate (MDCP) and trichlorophosphate (TCP) at room temperature onto the hydroxylated surface of a-SiO_2 utilizing infrared spectroscopy. The authors concluded that physisorption of the OPs to the surface occurred via hydrogen bonding between the phosphonyl O

and/or the methoxy O atoms of the OPs and surface hydroxyl groups[52,53]. Pertaining to DMMP, one of the OPs of interest in this work, adsorption onto the amorphous silica occurred by hydrogen bonding between the two methoxy oxygen atoms of DMMP and surface hydroxyl groups. Subsequent to adsorption, the OPs were reversibly desorbed at room temperature, 150°C, 300°C, and 400°C for TCP, MDCP, DMMP, and TMP, respectively[52]. The OPs were also found to be selectively desorbed using amine displacers. Although these reports are pertinent for the evaluation of sorbent materials, the conclusions that can be drawn are limited to the qualitative aspects of adsorption. Thus, a quantitative gap in data exists.

Recent efforts to evaluate the utility of material surfaces for OP adsorption by quantitative means have focused on computational studies. Bermudez[1] performed computational chemistry calculations on the adsorption of TCP, DMMP, and Sarin on a-SiO_2. The a-SiO_2 model utilized in the study by Bermudez[1] was obtained by terminating Van Ginhoven's optimized bare amorphous silica with ~3.4 –OH groups per nm^2; the model is structurally representative of amorphous silica. Interaction between DMMP and the $Si_{21}O_{56}H_{28}$ cluster resulted in an isosteric heat of adsorption of -20.0 kcal/mol for the most stable adsorption geometry. The most stable adsorption geometry involved hydrogen bonding between the surface hydroxyl groups and the phosphonyl O atom, as illustrated in Figure 2.1.

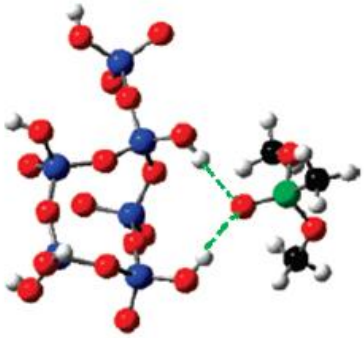

Figure 2.1. a-SiO_2 Adsorption of DMMP via the Phosphonyl O atom as obtained from Bermudez[1] (The Blue, Red, Green, Black, and White Atoms in the Figure represent Si, O, P, C, and H, respectively)

The less stable adsorption geometry between the surface hydroxyl groups and the methoxy O atoms, as illustrated in Figure 2.2, resulted in an isosteric heat of adsorption of -13.6 kcal/mol [1].

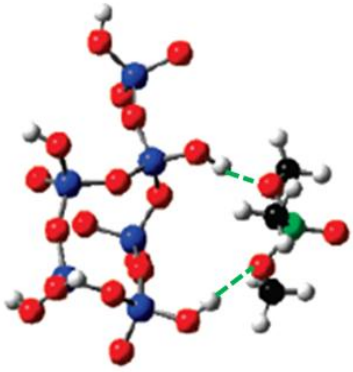

Figure 2.2. a-SiO_2 Adsorption of DMMP via the Methoxy O atom as obtained from Bermudez[1] (The Blue, Red, Green, Black, and White Atoms in the Figure represent Si, O, P, C, and H, respectively)

The validity of the adsorption energetics deduced from computational methods is uncertain since few experimental data exist for comparison. Moreover, the available calculations are based on an idealized one active site – one molecule interaction. A mismatch in energy may thus be expected when comparing the computational results to those obtained from experiment. Nevertheless, deducing adsorption energetics by experimental means is time intensive. In addition, safety concerns could arise when dealing with species of high reactivity or high toxicities. Hence, the use of computational chemistry as a pre-screening tool is beneficial, provided that the trends in the quantitative parameters can be accurately predicted.

This first work aims to systematically determine and compare experimental and computational chemistry data to determine the trends in adsorption energetics. Experimental heats of adsorptions are determined for four OP compounds of similar group contribution with the generic structure as illustrated in Figure 2.3.

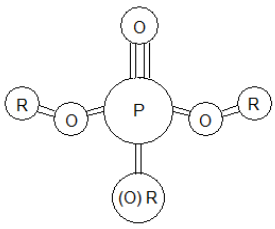

Figure 2.3. Generic Structure of the OPs of Interest

Specifically, the adsorption of dimethylphosphite (DMHP), dimethyl methyl phosphonate (DMMP), diethyl ethyl phosphonate (DEEP), and triethyl phosphonate (TEP) onto the hydroxylated surface of amorphous silica are

investigated. The OP compounds vary in their molecule size. Isosteric heats of adsorption are calculated based on Equation 2.1,

$$\Delta H = R\left[\frac{\delta \ln P}{\delta\left(\frac{1}{T}\right)}\right]_N \qquad \text{(Equation 2.1)}$$

where R is the gas constant, P is the pressure, and T is the absolute temperature. The ΔH value is evaluated at a specific value, N, that corresponds to the equilibrium amount of gas that is adsorbed onto the sorbent. Adsorptions isotherm are constructed at various pressures up to the saturation vapor pressure of the OPs to relate OP adsorption, N, to the pressure of the OP exposed to a-silica samples, P. The adsorption behavior (i.e. monolayer or multilayer) is also deduced from the experimental data. Prior to conducting the adsorption studies, vapor pressures as a function of temperature for the four OPs of interest are also measured since data for these OP compounds either exhibit great uncertainty or have not previously been published.

2.2 Experimental Details

Chemical and Reagents

Nanoparticles of hydrophilic fused silica with a BET surface area of 380 m^2/g were obtained from Evonik Degussa; these samples are amorphous in nature. Amorphous silica (a-SiO_2) samples were vacuum treated at 105°C for 45 minutes in an attempt to dislodge the surface adsorbed water molecules and subsequently sealed under vacuum prior to use. Liquid TEP, DMMP, DMHP, and DEEP of >98% stated purity were obtained from Spectrum Chemical (for DMMP) and Alfa

Aesar (for TEP, DMHP, and DEEP). To further enhance the purity of the OPs, the liquid samples were subjected to freeze-pump-thaw cycles using a custom manufactured vacuum system. Gaseous TEP, DMMP, DMHP, and DEEP were generated from the purified liquid samples.

Vapor pressure measurements

The vapor pressures of TEP, DMMP, DMHP, and DEEP were measured at six temperatures between 23.8°C and 34.6°C using the apparatus illustrated in Figure 2.4. Approximately 6 to 10 mL of liquid samples of TEP, DMMP, DMHP, or DEEP were loaded into the liquid sample holder. The liquid sample holder is constructed from a Pyrex round bottom flask modified with a ¼'' O.D. opening. The experimental apparatus was evacuated by opening valve V1 which connects the apparatus to the vacuum pump (U.S. Vacuum Model 100-3.5 Two Stage Rotary Vane Vacuum Pump). The liquid samples were frozen with liquid nitrogen, and valve V3 was opened to allow gases to be pumped from the apparatus as the liquid samples thawed. Freeze pump thaw cycles were repeated until bubbling was eliminated during the thaw cycle prior to the vapor pressure measurements.

Subsequent to the freeze pump thaw cycles, valve V3 was closed to allow the experimental apparatus to evacuate. The experimental apparatus was evacuated to a negligible pressure (i.e. less than the maximum resolution of the capacitance diaphragm gauges, e.g. 0.03 Torr). Meanwhile, the liquid sample holder was covered with heating ropes, insulated, and allowed to reach the desired

temperature set point. The experimental apparatus was also allowed to reach the desired temperature set point.

The temperature was controlled by an Omega CNi3243 temperature controller with a set point accuracy of ±0.1°C. Background studies were performed to measure the actual temperature variation in the experimental apparatus; temperature variations in the experimental apparatus were within 1°C of the temperature set point. Once the desired temperature set points were achieved, the experimental apparatus was closed to the vacuum pump and valve V3 was opened to the liquid sample holder to allow the liquid samples of TEP, DMMP, DMHP, or DEEP to reach their equilibrium saturation vapor pressures. The pressure of the apparatus was measured with two pressure gauges (CDG025 1000 Torr and CDG025 1 Torr) obtained from Inficon. For pressures between 0 to 1 Torr, the 0 to 1 Torr pressure gauge with a resolution of 0.00003 Torr was utilized. For pressures between 1 to 1000 Torr, the 0 to 1000 Torr pressure gauge with a resolution of 0.03 Torr was utilized. The measurements by the gauges were processed and indicated by the Inficon VGC402 pressure measurement unit and recorded by LabView software on an adjoining computer. Each pressure recording was logged in 30 seconds intervals until negligible changes in pressure, (specifically, the change in pressure, ΔP, per hour was less than the gauge resolution) was reached. For each OP compound, six temperatures were used, and five measurements of the vapor pressure were determined at each temperature.

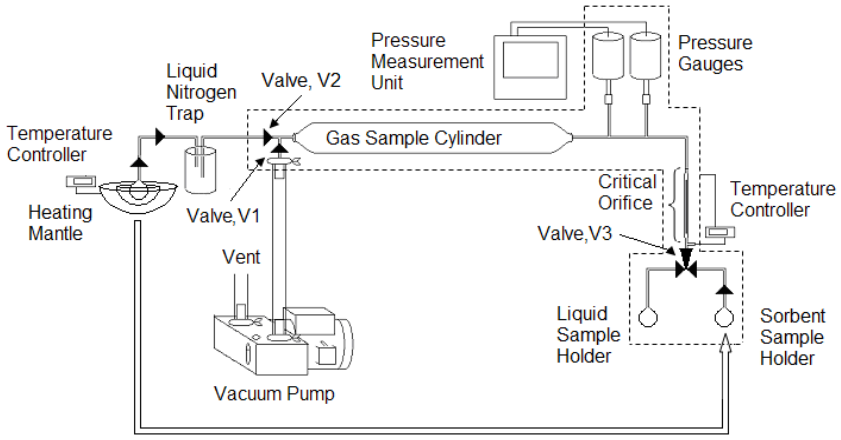

Figure 2.4. Experimental Apparatus

Adsorption isotherm measurements

Adsorption isotherm measurements were performed using a static volumetric method. Measurements were recorded at four temperatures between 23.8°C and 34.6°C. The experimental apparatus illustrated in Figure 2.4 for vapor pressure measurements was utilized for these measurements as well. For the adsorption studies, approximately 0.07 to 0.10 g of a-SiO_2 samples were loaded into the custom made Pyrex sorbent sample holder. The sorbent samples holder was slowly evacuated in a temperature controlled heating mantle at 105°C for 45 minutes prior to use. Evacuation was performed by opening valves V1 and V2 to create an open path to the vacuum pump and the valve directly connected to the sample holder was partially opened to create a small orifice for the air inside the sample holder to be evacuated while minimizing loss of the samples. Once

evacuation was completed, the sorbent sample holder was sealed under vacuum and transferred to the port on valve V3.

Subsequent to securing the sorbent sample holder onto the valve V3 connection, valve V2 was closed and valve V1 was kept open to allow the experimental apparatus to evacuate. The experimental apparatus was evacuated to a negligible pressure. Valve V3 was subsequently opened to the sorbent sample holder to determine the initial pressure of the experimental apparatus. Meanwhile, the experimental apparatus, including both the liquid sample holder and the sorbent sample holder, was covered with heating ropes, insulated, and allowed to reach the desired temperature set point as controlled by the Omega temperature controller. Once the desired temperature set points were achieved, the experimental apparatus was closed to the vacuum pump, valve V3 was closed to the sorbent sample holder, and opened to the liquid sample holder to allow the liquid OP samples to vaporize into the gas sample cylinder until the desired pressures were reached. The pressure of the gas sample cylinder was measured with the two pressure gauges and logged by LabView at 30 seconds interval.

Once the desired pressure was stabilized as indicated by the Inficon pressure measurement unit, the sorbent sample was then exposed to the gaseous OP sample by opening valve V3 to the sorbent sample holder. The change in pressure was then measured with the gauges and recorded by LabView, also at 30 seconds interval. The change in pressure was monitored and recorded until negligible changes in pressure (i.e. ΔP per hour < gauge resolution) was recorded. Once this state of "equilibrium" was reached, additional gaseous OP samples were

generated by allowing the liquid OP samples in the liquid sample holder to vaporize into the gas sample cylinder. The gas sample cylinder was opened to the liquid sample holder until the next desired pressure was attained. The procedure for exposure of the gaseous OP in the gas sample cylinder to the sorbent sample was repeated at additional pressures. Additive dosing of the gaseous OP onto the sorbent sample was performed until the saturation vapor pressure of the OP, at the corresponding temperature of the adsorption measurements, was reached. For each OP compound at each of the four temperatures, three sets of isotherm measurements were recorded.

2.3 Computational Details

Computational chemistry studies of the gas-solid interaction involve (1) optimization of the structure of the gaseous material, (2) optimization of the structure of the solid surfaces, and (3) the optimization of the coupled systems. DFT calculations on the gases of interest (i.e. organophosphorus) and the hydroxylated a-silica model were performed to determine the lowest energy conformation (most favorable geometry). All calculations were performed with the Gaussian 03 computational package[129]. The geometries of the OPs were individually optimized. The OP-silica pairs were subsequently optimized with the lowest energy conformer of the OPs as the starting structures. Upon completing the geometry optimization of the OPs and the OP-silica pairs, frequency calculations were performed to determine the thermodynamic parameters associated with the OP-silica interactions.

DMHP, DMMP, DMEP, DEEP, and TEP

DMHP, DMMP, DMEP, DEEP, and TEP can exist as one of multiple low energy conformers[131,132,133,134,135]. The lowest energy conformer is the focus of this work. The low energy conformers are thermodynamically favorable; computational investigations of the conformers for the five OPs of interest have been presented in published literature [131,132,133,134,135]. The ability to resolve the geometries of the low energy conformers of compounds by computational methods relies upon the capability of the functional and the basis set. These computational parameters describe the electronic behavior of the atoms that the compounds are composed of. The choice of which functional and basis sets to use is made by one of two methods: (1) comparison between the predictions of various properties (e.g. infrared absorption frequencies) determined by using the computational methods to the properties observed empirically and (2) comparison among the different computational methods used. Published computational results for the OPs of interests using different methods are summarized in Table 2.1.

This study investigates the interaction of silica with the most favorable conformer for each OP. The geometries of DMHP, DMMP, DMEP, DEEP, and TEP were optimized using density functional theory (DFT) with the B3LYP functional and the 6-31G (d) basis set. The B3LYP functional and 6-31G (d) basis set is the minimal method which has been utilized in published work by Yang et al.[135] with proven success for obtaining the lowest energy conformer for DMMP.

Table 2.1. Computational Chemistry Evaluation of the Organophosphates of Interest[124,125,126,127,128]

1. Comparison to empirical data

OP	Emprical data for comparison	Functional / basis set	Comment on Functional / basis set	Reference
DMMP TEP (TMP)	Fourier Transform Infrared Spectroscopy	MP2 / 6-311++(d,p) B3LYP / 6-311++ (3df,2p)	None	*Cuisset et al.*
DEMP DEEP (DIMP)	Fourier Transform Microwave Spectroscopy	Restricted Hartree-Fock B3LYP / 6-311G(d,p)	Higher level theory is needed to locate all conformers.	*DaBell et al.*
DMHP	Matrix Isolation Infrared Spectroscopy	HF/ 6-31++G(d,p) B3LYP / 6-31++G(d,p)	HF gave an imaginery frequency for one of the conformers.	*Sundararajan et al.*
DMMP	Fourier Transform Microwave Spectroscopy	HF / 6-31G(d) MP2 / 6-311G(d)	HF gave better approximation of rotational constants and inertial defects.	*Suenram et al.*

2. Comparison among functional and basis set

OP	Emprical data for comparison	Functional / basis set	Comment on Functional / basis set	Reference
DMMP	None	B3LYP / 6-31G(d), 6-31++G(d,p), aug-cc-pVDZ MPW1K / 6-31G(d), 6-31++G(d,p), aug-cc-pVDZ MP2 / 6-31G(d), 6-31++G(d,p), aug-cc-pVDZ CBS-QB3	Lowest energy conformer found with B3LYP/6-31G(d). Geometries determined by B3LYP is in good agreement with those predicted from higher level theories, and increasing the size of the basis set beyond 6-31G(d) had no significance differences.	*Yang et al.*

Silica and OP interaction

The structure for the various forms of silica (e.g. with defects [136,137,138], bare [139,140,141,142,143,144,145,146,147,148,149,150,151,152,153,154,155,156,157,158] vs. hydroxylated[159,160,161, 162,163,164], amorphous vs. crystalline[165,166,167,168]) have been investigated by computational chemistry methods. The defect-free hydroxylated surface of amorphous silica is the subject of interest in this study. Investigations on the structural features (i.e. bulk structure and surface properties of hydroxyl sites) of the defect-free hydroxylated surface of a-SiO_2 have been conducted by two different methods: dissociative adsorption of water onto the bare silica surface[161,162,163,164]and comparative evaluation of surfaces with artificial loading of –OH groups[159,160]. In the former method, the well established bare SiO_2 surface is often utilized. These bare models are amorphousized and optimized by the simulated annealing of large slabs of crystalline silica on the order of 10^3 atoms in size. The resulting structure of the bare silica consists of a fourfold coordinated Si atoms (i.e. Si connected to four other units by bonding interactions) and twofold coordinated oxygen atoms except in areas where under-coordinated defects are present. A large distribution of these Si and O atoms appear as 4 to 8-fold SiO_2 rings in the underlying layers, with a smaller distribution of even larger rings (also found in the underlying layers) and low concentrations of the smaller twofold and threefold rings near the surface[7,169,144]. Studies on the reaction between water and the bare amorphous cluster <100 atoms in size (which are structurally in agreement with the aforementioned description) concluded that the three-coordinated Si defect was the most favorable site for hydroxylation, especially when the defect

was positioned near a non-bridging oxygen; hydroxylation only occurred in the presence of other water molecules[161,162,164].

In the latter method (i.e. artificial loading of –OH groups), a silica model with similar ring distributions as those determined from bare a-SiO_2 calculations are artificially loaded with one or more –OH at different termination sites. These structures are optimized and their simulated properties such as NMR shifts, infrared absorption frequencies, and dehydrogenation energies are compared with experimental observation. Ugliengo[160] investigated five different surfaces of 60 Si-atom models with varying –OH densities (7.2, 5.4, 4.5, 2.4, 1.5 –OH groups per nm^2). These surfaces were representative of a-SiO_2 that was heated at different temperatures. The study concluded that high concentrations of terminal –OH (as opposed to –OH involved in hydrogen bonding contacts within the structure) were available for surface interactions. Tielens[159] investigated the top and bottom surfaces of a $Si_{26}O_{65}H_{27}$ slab model. The optimized structures consisted of 5.8 –OH groups per nm^2 with a larger density of terminal sites (-OH on a three coordinated Si) than germinal sites (-OH on a two coordinated Si) on the surface. These studies concluded good agreement with empirical data such as NMR shifts, infrared absorption frequencies, and dehydrogenation energies.

In summary, the hydroxylated defect-free a-SiO_2 model is described by a large distribution of 4 to 8-fold coordinately saturated SiO_2 rings in the bulk, some 2 and 3-fold coordinately saturated SiO_2 rings on the surface, and a large distribution of terminal –OH of an experimentally correlated density on three-coordinated surface Si atoms.

In this work, a new, reduced size model, as illustrated in Figure 2.5, was constructed based on a larger model that was obtained from Dr. V.M. Bermudez of the Naval Research Laboratories and utilized in his previously published work[1]. All of the models are based from the original work of Van Ginhoven[154]. The reduced cluster in the current work was terminated with –OH to achieve the desired functionality.

Interactions between the silica surface shown in Figure 2.5 and the five OPs of interest were optimized using density functional theory (DFT) with the B3LYP functional and a 6-31G (d) basis set. When geometry optimization was completed, frequency calculations were performed to determine the thermochemical data for each of the silica and OP (i.e. DMHP, DMMP, DMEP, DEEP, and TEP) pairs.

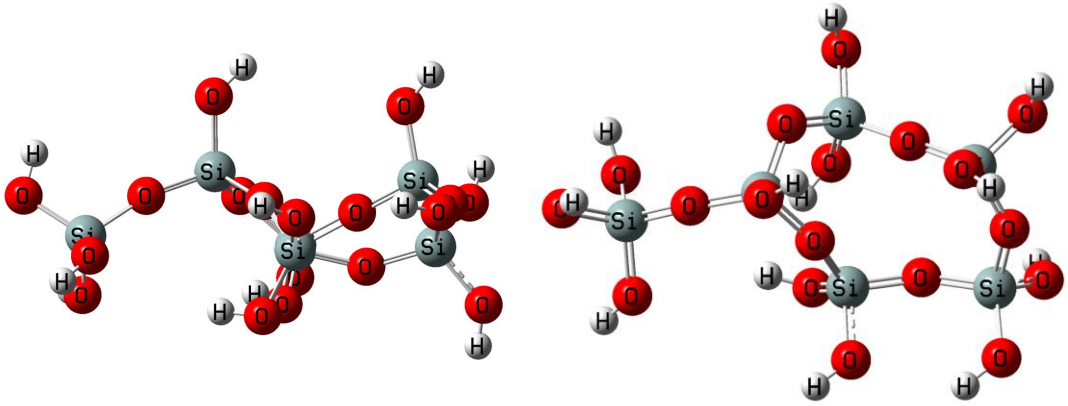

Side View Top View

Figure 2.5. Side View and Top View of Amorphous Silica Cluster for Adsorption of OPs

2.4 Results and Discussion

The validity of the adsorption isotherm is limited to relative pressures, *x*, between 0 and 1 (relative to the saturation vapor pressure, P^o). Saturation vapor pressures must be known at each temperature of interest prior to undertaking the adsorption isotherm measurements. The vapor pressures for DMHP and DMMP are available in the literature at limited temperatures[2,3], whereas the vapor pressures for DEEP and TEP have not been previously published in the open literature.

2.4.1 Vapor pressure of DMHP, DMMP, DEEP and TEP

The vapor pressures of DMHP, DMMP, DEEP, and TEP were measured at six temperatures of interest: 23.8, 26.4, 28.0, 30.6, 32.1, and 34.6°C. Figures 2.6 - 2.9 illustrate the results for DMHP, DMMP, DEEP, and TEP, respectively; comparisons to available literature values are also illustrated.

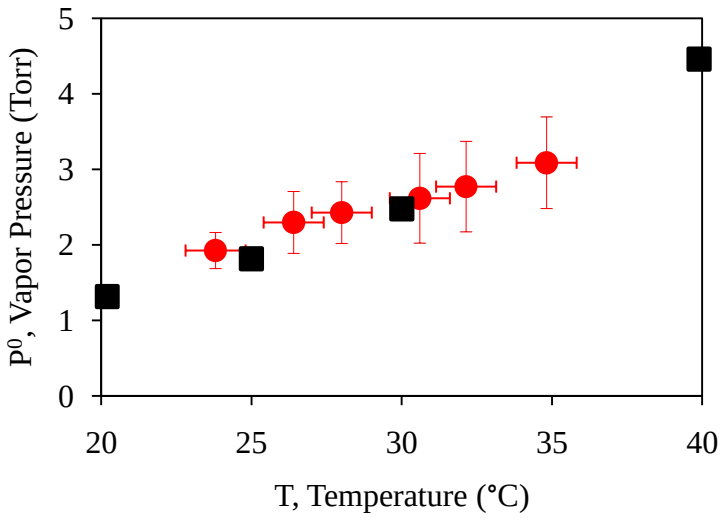

Figure 2.6. Vapor Pressure, P^o, of DMHP (●) ±1σ at 23.8, 26.4, 28.0, 30.6, 32.1, and 34.6°C and Literature Values (■)[2]

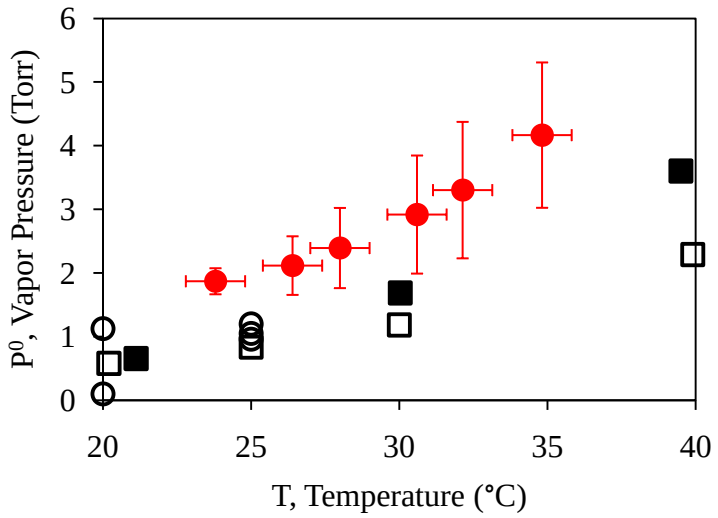

Figure 2.7. Vapor Pressure, P^o, of DMMP (●) ±1σ at 23.8, 26.4, 28.0, 30.6, 32.1, and 34.6°C determined in this work. Literature Values are represented by (■)[2], (□)[3], and (○)[4,5,6]

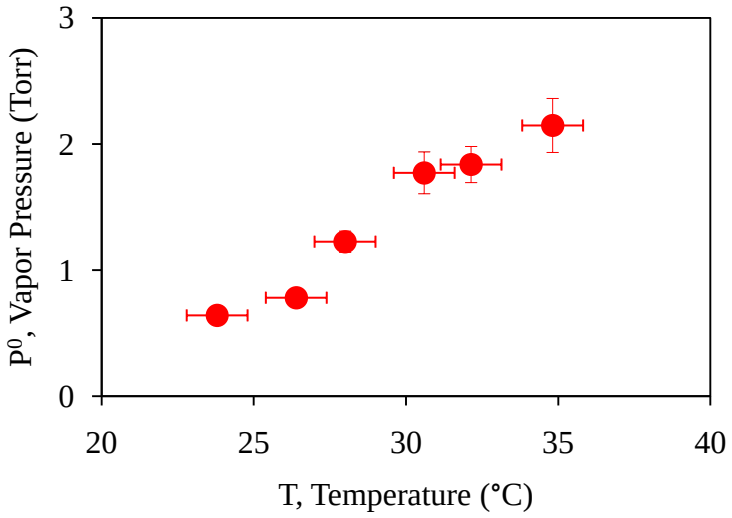

Figure 2.8. Vapor Pressure, P^o, of DEEP (●) ±1σ at 23.8, 26.4, 28.0, 30.6, 32.1, and 34.6°C

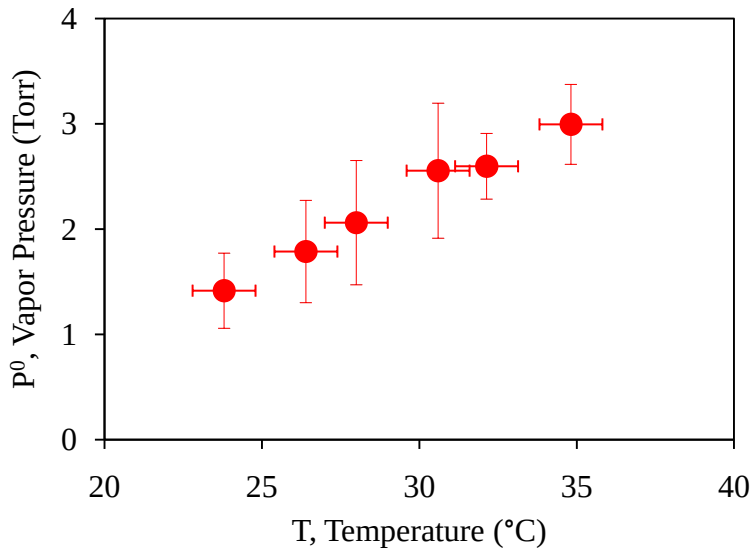

Figure 2.9. Vapor Pressure, P^o, of TEP (●) ±1σ at 23.8, 26.4, 28.0, 30.6, 32.1, and 34.6°C

The vapor pressures, P^o, for DMHP, DMMP, DEEP, and TEP measured at T = 23.8, 26.4, 28.0, 30.6, 32.1, and 34.6°C in this work increase with increasing temperature, as expected. The increase in vapor pressure can be attributed to the increase in the kinetic energy of the molecules at higher temperature.

In comparison to the available literature values, discrepancies in the vapor pressures of DMMP exist among the published work and with the values measured in this work[46-50]. Specifically, the vapor pressures of DMMP measured from this work are consistently higher than those reported by Tevault and coworkers[2,3]; vapor pressures higher and lower than the values obtained by Tevault and coworkers[2,3] have also been reported as illustrated in Figure 2.7. It should also be noted that the values reported by Tevault and coworkers in 2009[2] are in better agreement with the values measured in this work than the values reported by

Tevault and coworkers in 2006[3]. On the contrary, the vapor pressures of DMHP measured from this work are in excellent agreement with the values obtained and published by Tevault and coworkers[2].

Conclusive reasons for the discrepancy between the experimental values obtained in this work and the values reported in references[4-6] cannot be fully commented upon since some of the published data contain no information on the measurement methodology. Agreement in the DMHP values and discrepancies with the DMMP values reported by Tevault and coworkers in 2009[2] may be explained by the differences in sample purity and measurement methodology. In our work, DMMP samples, initially of 99.3% purity, were further purified by repeated freeze-pump-thaw cycles, a technique that is effective for the removal of any impurities with higher vapor pressures than our compound of interest. It is noted that Tevault and coworkers[2] used DMMP samples of 99% purity (as stated by their supplier) without further purification and DMHP samples of 99.87% purity (measured in their work). Moreover, Tevault and coworkers[2] determined the vapor pressure of DMMP by a gravimetric measurement (i.e. a measurement of the mass change of any liquid material present), while the DMHP vapor pressure measurements were determined using a chromatographic method that focused on specifically measuring the DMHP. The gravimetric and chromatography methodologies differ in the ability of chromatography to differentiate between a response induced by the DMHP (the OP compound studied) from a response induced by an impurity. The gravimetric method is unable to identify sources of error due to impurities in the DMMP sample (i.e. an impurity with a lower vapor P would lead to a lower mass

loss of the liquid phase and correlate to a lower vapor P for DMMP). With these differences in mind, the discrepancies between the values published by Tevault and coworker in 2009[2] and the values measured in this work may be easily explained. Note that the larger magnitude of discrepancies between the values in this work and the values published by Tevault and coworker in 2006[3] cannot be explained by differences in purity (i.e. this would require a significant difference in purity). Dr. Tevault was contacted, and electronic mail communication indicated that the 2009 data were more reliable.

Based on the explanation given, the values obtained in this work are in reasonable agreement with recently published data and are reliable. Thus, the vapor pressures measured in the current work were utilized for the adsorption isotherm measurements.

2.4.2 a-SiO_2 adsorption of DMHP, DMMP, DEEP, and TEP

Adsorption isotherm

Amorphous silica was exposed to single-component gas samples of DMHP, DMMP, DEEP, and TEP at 23.8, 28.0, 30.6, and 34.6 °C. Adsorption measurements were made for gas sample pressures, P, between 0 Torr and the average vapor pressure of the OPs, P^o (i.e. between relative pressure, x =P/ P^o, from 0 to 1). Adsorption of the OP onto amorphous silica, N, was correlated from the pressure measurement using the ideal gas law. The validity of the ideal gas law was confirmed by insignificant differences between the pressure, volume,

temperature behavior predicted by the ideal gas law and that predicted by the virial equation of state.

The experimental results for DMHP, DMMP, TEP, and comparisons of the experimental results to the four adsorption isotherm models listed in Table 2.2 are illustrated in Figures 2.10 – 2.12. Note that attempts were made to determine the adsorption of DEEP onto amorphous silica at 23.8, 28.0, 30.6, and 34.6 °C. The measurements, however, were statistically insignificant (see Appendix). This indicates the limitations of the measurement technique for exceptionally low volatility compounds. Thus, the adsorption isotherms of DEEP were not utilized and will not be discussed.

Table 2.2. Multilayer Adsorption Isotherm Models

Isotherm model	**Model equation**[170,171,172]
BET	$N = \frac{a_m}{(1-x)} * \frac{\frac{Kx}{(1-x)}}{1+\frac{Kx}{(1-x)}}$
nBET	$N = \frac{a_m}{(1-x)} * \frac{Kx(1-(n+1)x^n + nx^{(n+1)})}{1+(K-1)x - Kx^{(n+1)}}$
BDDT	$N = \frac{a_m}{(1-x)} * \frac{Kx(1+n((q-1)x^{n-1} + qx^{n+1} - (2q-1)x^n) - x^n)}{1+(K-1)x + K((q-1)x^n - qx^{n+1})}$
Hüttig	$N = \frac{a_m(1+x)Kx}{(1+Kx)}$

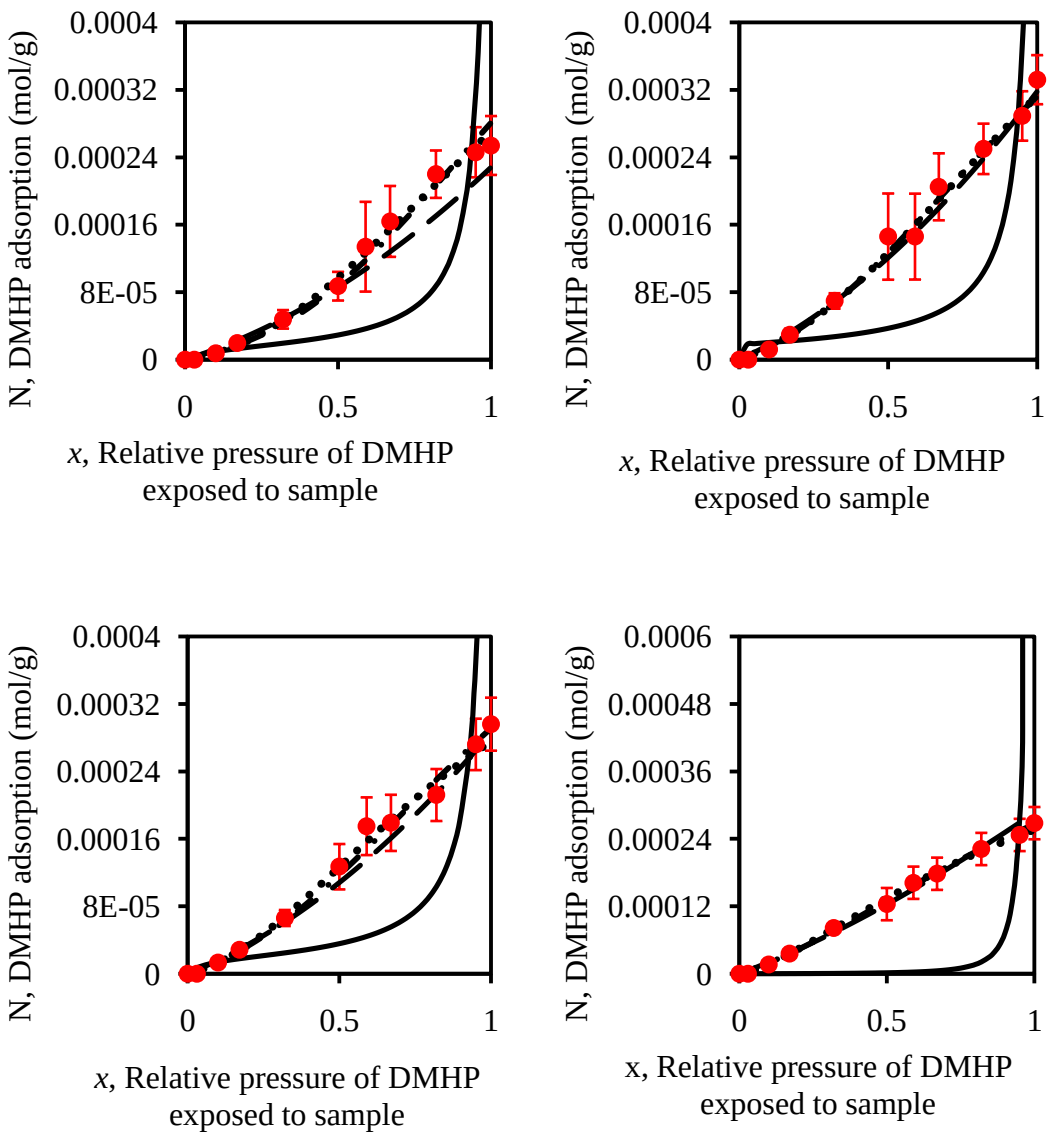

Figure 2.10. Adsorption of DMHP (●) by a-SiO_2 at 23.8°C (top left), 28.0°C (top right), 30.6°C (bottom left), and 34.6°C (bottom right) as compared to the BET (—), the nBET (– . –), the BDDT (....), and the Hüttig (— –) Models

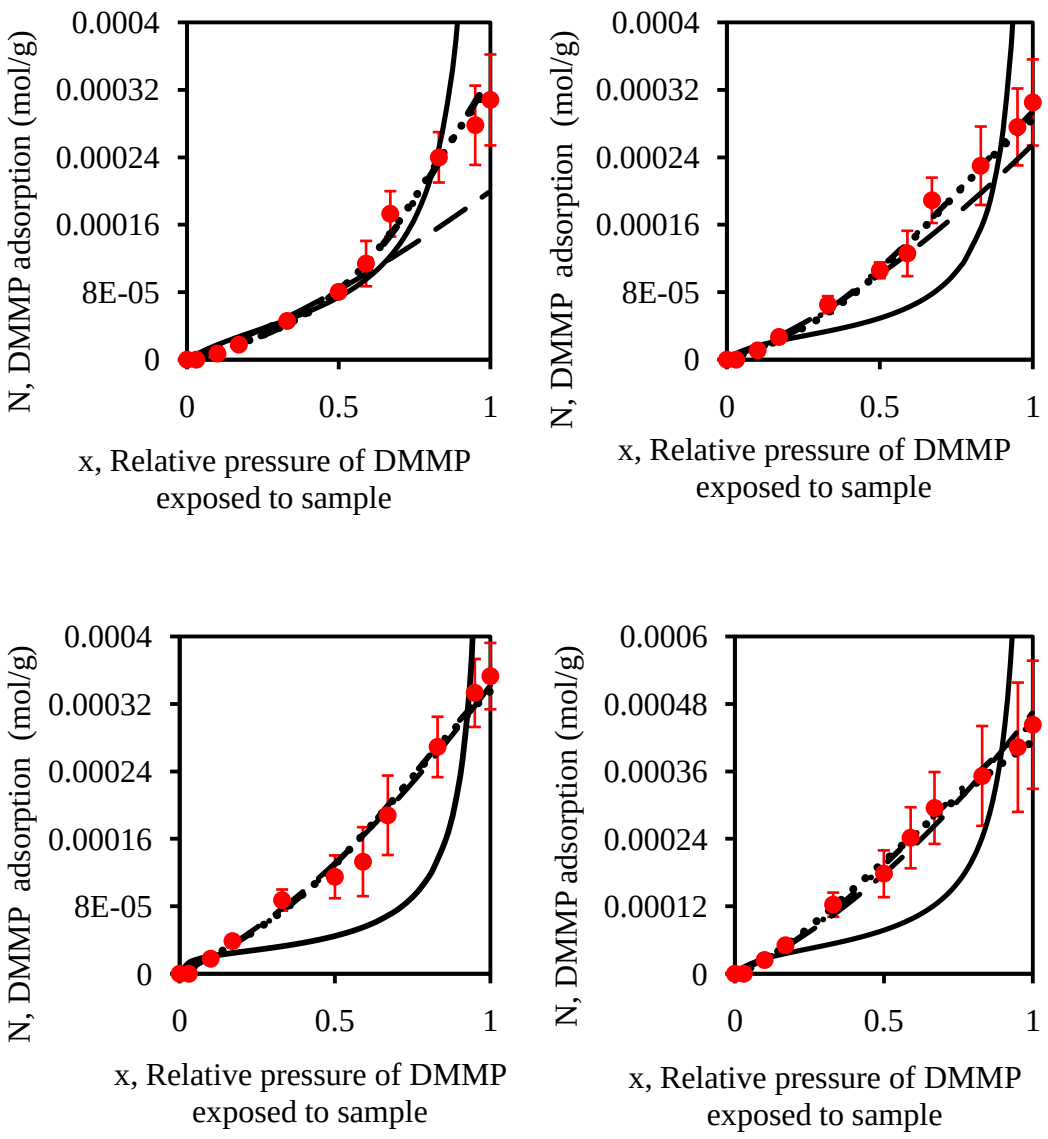

Figure 2.11. Adsorption of DMMP (●) by a-SiO_2 at 23.8°C (top left), 28.0°C (top right), 30.6°C (bottom left), and 34.6°C (bottom right) as compared to the BET (——), the nBET (– . –), the BDDT (····), and the Hüttig (— –) Models

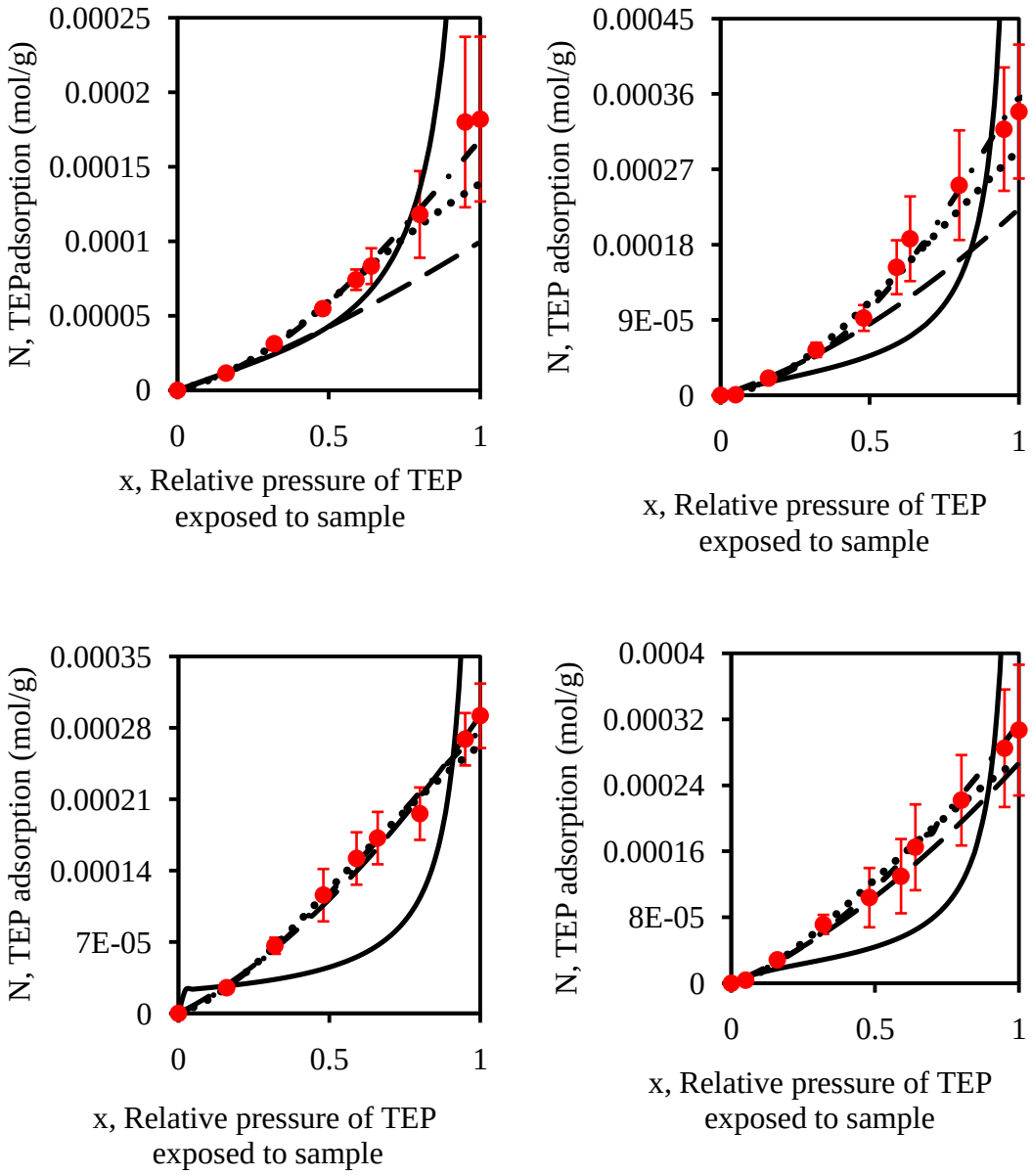

Figure 2.12. Adsorption of TEP (●) by a-SiO_2 at 23.8°C (top left), 28.0°C (top right), 30.6°C (bottom left), and 34.6°C (bottom right) as compared to the BET (——), the nBET (– . –), the BDDT (····), and the Hüttig (— —) Models

TEP, DMMP, and DMHP adsorption onto amorphous silica demonstrates multilayer adsorption behavior (i.e. monotonic increase in adsorption, N, as relative pressure, *x*, approaches unity[124,125]). To obtain a continuous representation

of the experimental data for any value of *x*, the results were compared with the isotherm models listed in Table 2.2. These isotherm models are representative of multilayer adsorption such as the Type II-VI isotherms shown in Chapter 1. In Table 2.2, the adsorbed amount, N, is related to the monolayer capacity, a_m, the adsorption constant, *K*, the number of layers of sorbate, *n*, and the compensation for energetic diversity, *q*, as well as the relative pressure, *x*, in these multilayer adsorption isotherm models. The nBET, BDDT, and the Hüttig models are extensions to the BET model, which is one of the first attempts to represent multilayer adsorption[173,174,175]. The BET model assumes that (1) adsorption occurs on an energetically homogenous surface[176], (2) the adsorption and desorption behavior of an infinite number of adsorbed layers beyond the second layer are identical, (3) the adsorption energy is assumed to be equivalent to that of the liquid state, and (4) the molecules adsorbed on the surface do not interact with one another[171]. The nBET model relies upon the same assumptions as the BET model, although it limits adsorption to only a finite number of adsorbable layers[171]. An additional parameter, *q*, in the BDDT model accounts for the effects of energetic diversity due to the compensation for effects such as capillary condensation[171]. All three of these models have the inherent implication that adsorbed molecules cannot desorb from the surface if additional layers are present on top of them. In the case of the Hüttig model, desorption of any molecule is assumed to be unimpeded[172].

As illustrated in Figures 2.10 – 2.12, the BET model underpredicts adsorption at low relative pressures and overestimates adsorption at high relative pressures. The Hüttig model represents the adsorption data at low relative pressure but

underestimates adsorption at high relative pressures. Conversely, both the nBET and the BDDT models represent the experimental results within the uncertainty of the measurements. The sources of discrepancy lie within the inherent assumptions of the isotherm models. Specifically, BET adsorption approaches infinity as relative pressure, *x*, approaches unity. The nBET and BDDT adsorption models are defined with a finite number of absorbable layers. The Hüttig model also converges to a constant as the relative pressure, *x*, approaches 1. In summary, the 2 parameter BET and Hüttig models fail to describe all of the experimental results. Although the BDDT model provided better fit (e.g. lower values of χ^2) for some of the experimental data, the 3 parameter nBET model and the 4 parameter BDDT model were equivalent in efficacy within the uncertainty of the measurements. (Adsorption isotherm model parameters, the standard deviation of the model parameters, χ^2, from regression analyses, and P values from F tests were obtained using Igor Pro 6.03 and are listed in the Appendix. The values of χ^2 were minimized to obtain the best-fit model parameters). Further discussions for DMHP, DMMP, and TEP utilize the nBET model predictions since the nBET model predictions provide continuous representations of the experimentally determined relationships between OP adsorption, N, and relative pressure of the OP, *x*, using a minimal number of parameters.

Temperature dependence of the adsorption isotherm

The temperature dependence of the adsorbed number of moles, N, for DMHP, DMMP, and TEP, are represented by the nBET predictions as shown in Figures 2.13 – 2.15, respectively. Again, it is important to emphasize that the nBET model

provided an excellent fit to the experimentally derived data, and the model was simply used to provide a continuous representation that is easier to visualize in Figures 2.13 – 2.15.

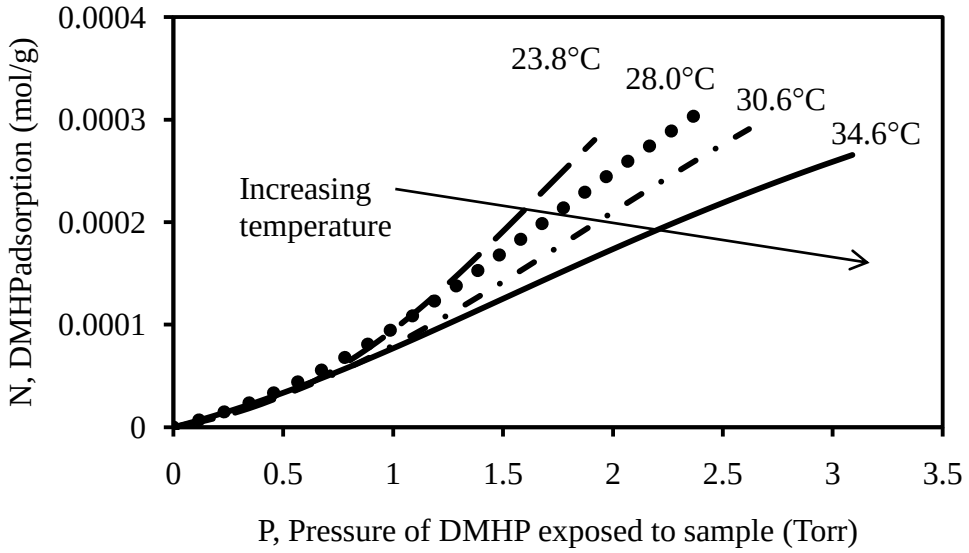

Figure 2.13. Temperature Dependency of DMHP Adsorption, N, as represented by nBET Predictions for Adsorption by a-SiO_2 at 23.8, 28.0, 30.6, and 34.6 °C

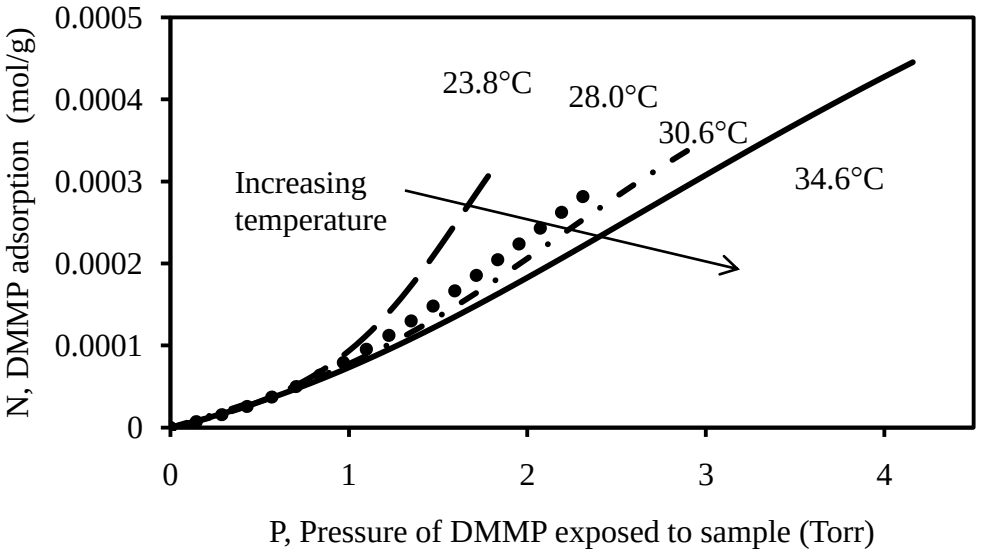

Figure 2.14. Temperature Dependency of DMMP Adsorption, N, as represented by nBET Predictions for Adsorption by a-SiO_2 at 23.8, 28.0, 30.6, and 34.6 °C

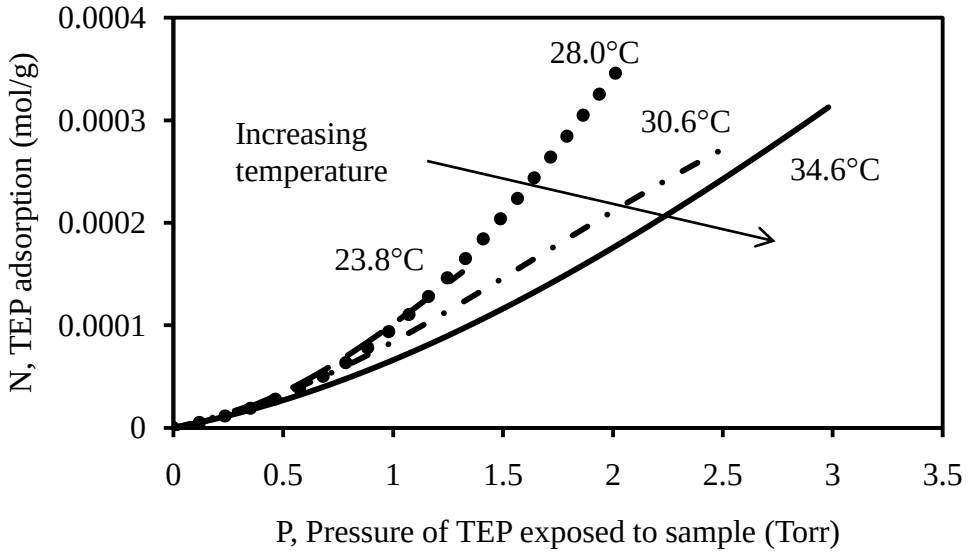

Figure 2.15. Temperature Dependency of TEP Adsorption, N, as represented by nBET Predictions for Adsorption by a-SiO_2 at 23.8, 28.0, 30.6, and 34.6 °C

The adsorptions of DMHP, DMMP, and TEP decrease with increasing temperature. These results are representative of exothermic processes such as adsorption (i.e. interactions are less favorable with increases in temperature[177,178]). Figures 2.13 – 2.15 also illustrate variations in the magnitude of decrease in DMHP, DMMP, and TEP adsorption with increases in temperature. These variations are evidence of surface heterogeneity[179] (e.g. adsorption on energetically diverse adsorption sites and potential interaction with trace amounts of water on the surface). Effects of surface heterogeneity are subsequently discussed.

Isosteric heat of adsorption

The isosteric heat of adsorption was defined in Equation 2.1, and is based upon the temperature dependence of the adsorption isotherms. To determine the isosteric heat of adsorption, ln P versus T^{-1} plots were constructed at N = 0.0001 g/mol. This adsorption amount, N, allows all collected data (i.e. adsorption at 23.8, 28.0,

30.6, and 34.6 °C) to be included in the calculation. The ln P versus T^{-1} plots for DMHP, DMMP, and TEP adsorption onto a-SiO_2 are illustrated in Figures 2.16 – 2.18, respectively. The isosteric heats of adsorption for TEP, DMMP, and DMHP as calculated from Figures 2.16 – 2.18 and Equation 2.1 are listed in Table 2.3.

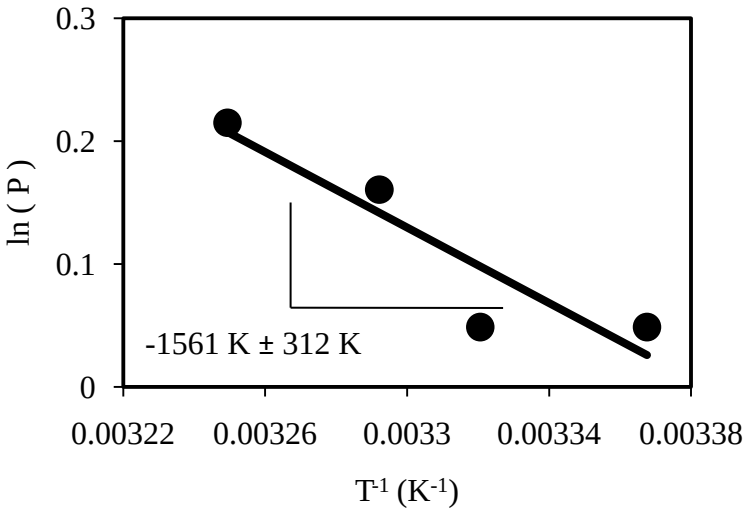

Figure 2.16. Ln P (from nBET Prediction) versus T^{-1} Plot for DMHP Adsorption onto a-SiO_2

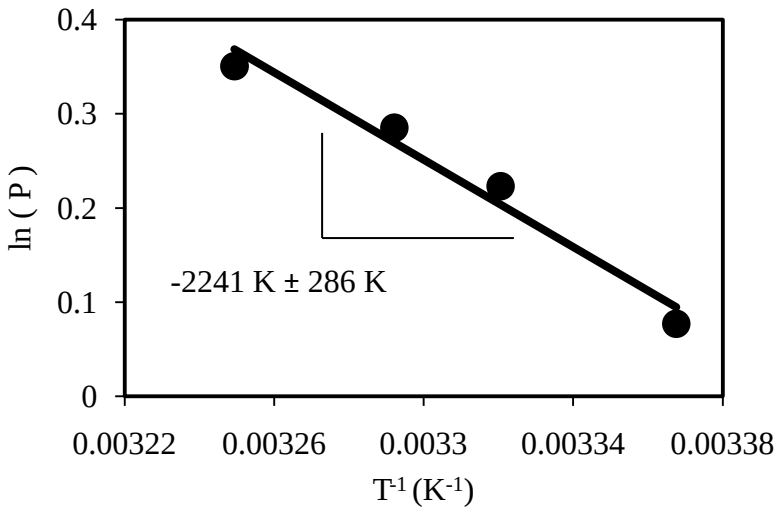

Figure 2.17. Ln P (from nBET Prediction) versus T^{-1} Plot for DMMP Adsorption onto a-SiO_2

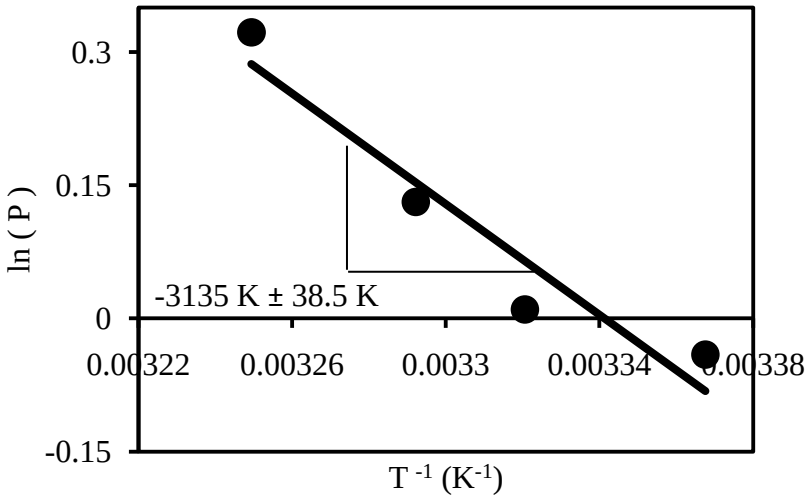

Figure 2.18. Ln P (from nBET Prediction) versus T^{-1} Plot for TEP Adsorption onto a-SiO_2

Table 2.3. Isosteric Heat of Adsorption for a-SiO_2 Adsorption of OPs

OP compound	**Isosteric heat of adsorption ± 1σ (kcal/mol)**
DMHP	-2.97 ± 0.593
DMMP	-4.28 ± 0.543
TEP	-5.96 ± 0.073

Considering the adsorption onto a-SiO_2, the isosteric heat of adsorption is more negative for TEP as compared to DMMP, and more negative for DMMP as compared to DMHP. These data indicate that TEP has a more favorable interaction with a-SiO_2 as compared to either DMMP or DMHP. For a particular class of compound with similar group contributions, the size of the molecule generally dictates its volatility. The volatility, in turn, affects its desire to condense onto surfaces. Larger gas molecules are less volatile and favor the sorbed phase in the absence of strong specific interactions (i.e. chemical reactions).

The relationship between the isosteric heat of adsorption and the sizes of the OP molecules are illustrated in Figure 2.19.

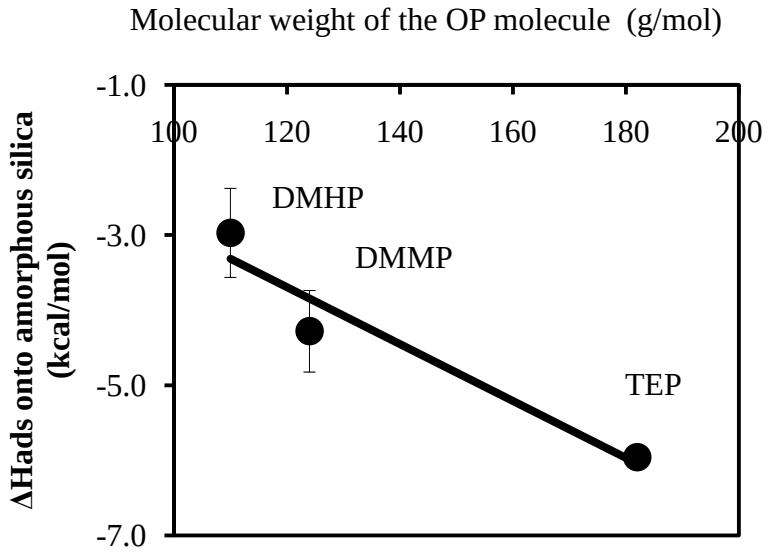

Figure 2.19. Variation in the Heat of Adsorption with Variation in Molecular Size (The errors represent ± 1σ)

The size of the molecules increased from that of DMHP to DMMP to TEP, and the isosteric heat of adsorption became more negative as the molecular size increased. TEP, the largest among TEP, DMMP, and DMHP, resulted in the most negative isosteric heat of adsorption, as expected.

2.4.3 Comparison to DFT study of OP adsorption onto a-SiO_2

The adsorption of DMHP, DMMP, DMEP, DEEP, and TEP onto a-SiO_2 were investigated using computational chemistry calculations using a modification of a cluster model obtained from Dr. V.M. Bermudez of the Naval Research Laboratories. To simplify the calculations in this work, the cluster size was

reduced from that which was previously used by Bermudez[1]. The optimized geometries for the interactions are illustrated in Figure 2.20.

The interactions between the OPs and the surface hydroxyl groups of silica occurred through the phosphonyl O atom, as indicated by the dashed lines in Figure 2.20. The interaction involved two –OH groups on the surface of the a-SiO_2 cluster. In a previously published computational investigation of the adsorption of DMMP onto a larger a-SiO_2 cluster ($Si_{21}O_{56}H_{28}$), adsorption via two hydrogen bonds with the phosphonyl O atom was also observed; a heat of adsorption of -20.0 kcal/mol was reported for this interaction with DMMP[1].

To verify the validity of our reduced size a-SiO_2 cluster and to compare these results to those obtained experimentally, the computational predictions for the heat of adsorption were calculated using Equation 2.2.

$$H_{ads} = H(cluster + OP\ compound) - H(cluster) - H(OP\ compound) \quad \text{(Equation 2.2)}$$

The heats of adsorption associated with the interactions are shown in Table 2.4.

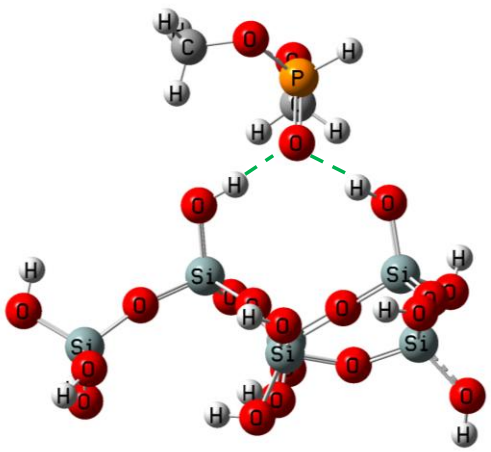

DMHP

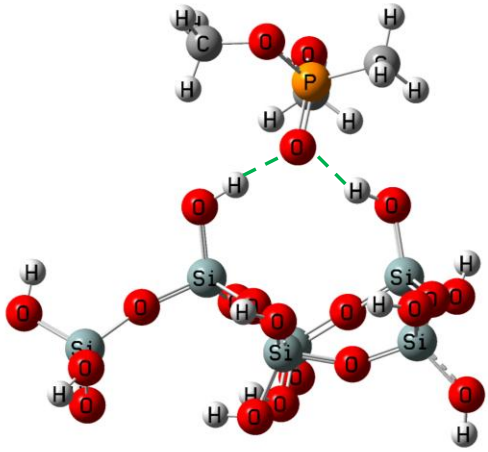

DMMP

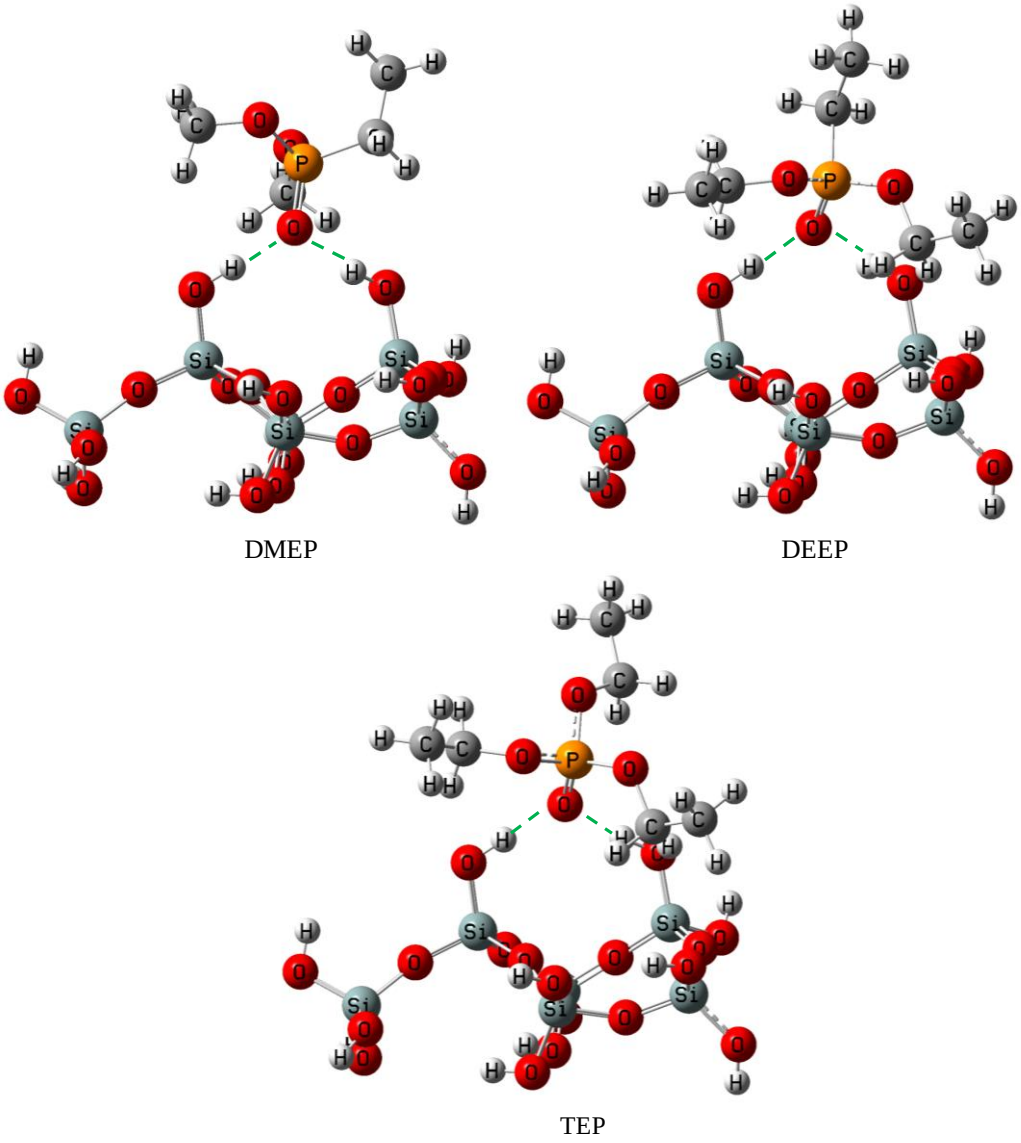

Figure 2.20. Optimized Geometries for the Interaction of DMHP, DMMP, DMEP, DEEP, and TEP with Amorphous Silica as represented by the Dashed Lines

Table 2.4. Calculated ΔH_{ads} for OP Adsorption on a-SiO_2

OP compound	**ΔH_{ads} (kcal/mol)**
DMHP	-16.8
DMMP	-19.7
DMEP	-19.4
DEEP	-21.4
TEP	-21.7

First, it should be noted that the heat of adsorption for DMMP is in excellent agreement with literature data[1]. It should then be noted that the OP compounds in Table 2.4 were arranged according to increasing size (i.e. DMHP < DMMP < DMEP < DEEP < TEP). As seen in Table 2.4, the heats of adsorption generally became more negative as molecular size increased.

In comparison with the experimental results, the computational calculations accurately predicted the trend observed between the changes in the heat of adsorption with changes in molecular size. However, the DFT calculation results were consistently more negative than the experimentally determined heats of adsorption determined at the OP adsorption value of 0.0001 g/mol. The differences in energy values between the experimental and computational data may be attributed to surface heterogeneity.

Surface heterogeneity results in energetic diversity. In the case of a-SiO_2, the interactions of OP compounds with less favorable geometries, including interaction via the methoxy O atom, as well as interactions with different types of

–OH sites, the number of –OH sites involved in hydrogen-bonding, and interaction with adsorbed or pre-adsorbed molecules on the surface could contribute to energetic diversity. For instance, the presence of pre-adsorbed water or adsorbed OP on the surface results in OP interaction with the surface bound water molecule or the surface bound OP. These interactions would extend the distance between the OP molecule and the surface. A less negative adsorption heat of adsorption associated with the interaction between the OP and the a-SiO_2 surface would therefore be expected[180].

In the absence of two adjacent surface hydroxyl groups or in the event that the OP molecule is locally stabilized through interaction with one surface –OH, thus leading alkyl group to hinder the interaction with the second –OH, a different adsorption energy would also be expected. The effects from the reduction of –OH sites involved in hydrogen bonding on the heats of adsorption were determined by DFT methods for the interaction of two example OPs, i.e. DMHP and DMEP. The optimized geometries for interaction with one –OH site are illustrated in Figure 2.21.

The interaction of DMHP and DMEP with a single –OH site resulted in heats of adsorption of -12.7 kcal/mol and -13.9 kcal/mol, respectively. Comparatively, these values are more positive (less negative) than the heats of adsorption of -16.8 kcal/mol and -19.4 kcal/mol obtained for the same OP molecules when two surface –OH sites are involved in hydrogen bonding.

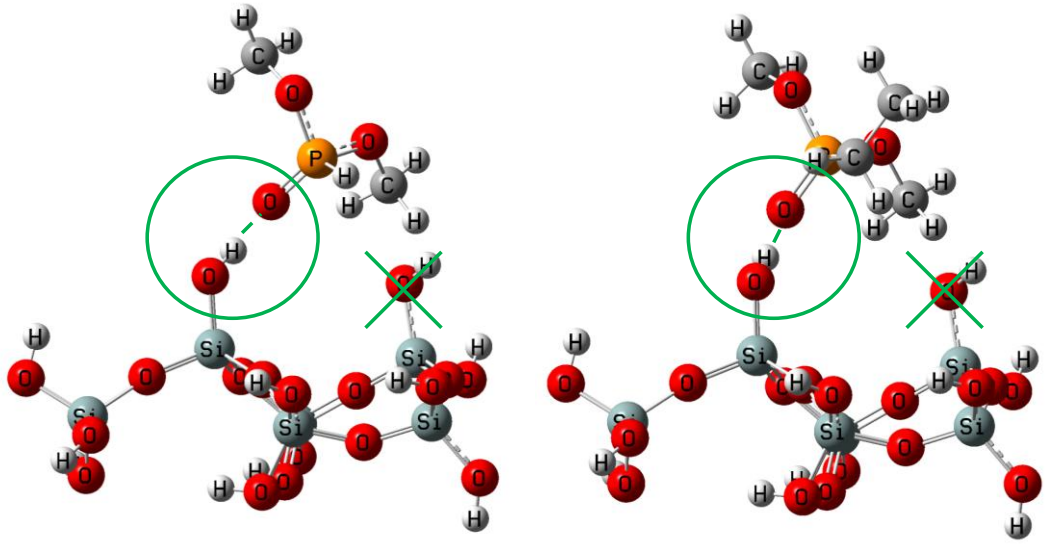

DMHP DMEP

Figure 2.21. Optimized Geometries for the Interaction of DMHP and DMEP for Interaction with a Single –OH Site (circled) as opposed to Interaction with a Second –OH sites (crossed) as well, as shown in Figure 2.20

Interactions with different types of surface –OH sites also leads to less favorable interaction geometries, thus influencing the calculated thermochemical data. As seen in the DFT study of DMMP adsorption by hydroxylated alumina, the heat of adsorption could range from -4.5 to -23.2 kcal/mol for interaction of DMMP with an OH bonded to a single surface Al to an OH bonded to three Al atoms, respectively[123].

Lastly, interaction with the methoxy O atom introduces a source of energetic diversity. Bermudez[1] investigated the less favorable adsorption between the surface hydroxyl groups and the methoxy O atoms, illustrated in Figure 2.2. This interaction resulted in a less negative isosteric heat of adsorption of -13.6 kcal/mol (compared with -20 kcal/mol for interaction of the same cluster model with the phosphonyl O atom).

The temperature dependence of the adsorption isotherms (presented in the previous section) provided supporting evidence for the energetic diversities. This hypothesis was further investigated using Raman spectroscopy.

2.4.4 Energetic heterogeneity examined by Raman spectroscopy

Raman spectra were obtained from a sample of amorphous silica subsequent to its exposure to DMMP in the experimental apparatus utilized for the adsorption isotherm measurements. The Raman spectra of the sample before and after exposure to DMMP are illustrated in Figure 2.22.

The exposure of amorphous silica to DMMP resulted in the formation of spectroscopic features associated with DMMP. The results are compared with the Raman spectrum of DMMP from literature and the peaks are assigned in Table 2.5[181].

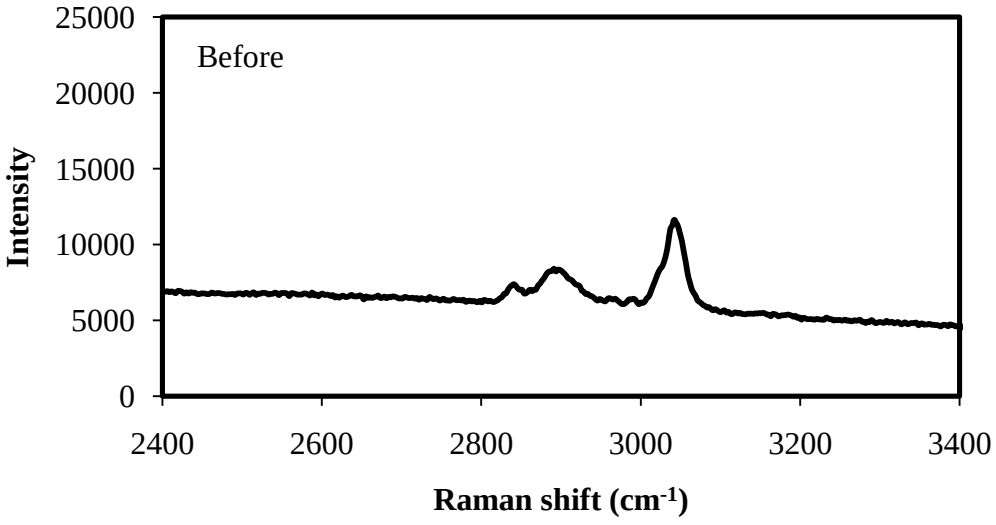

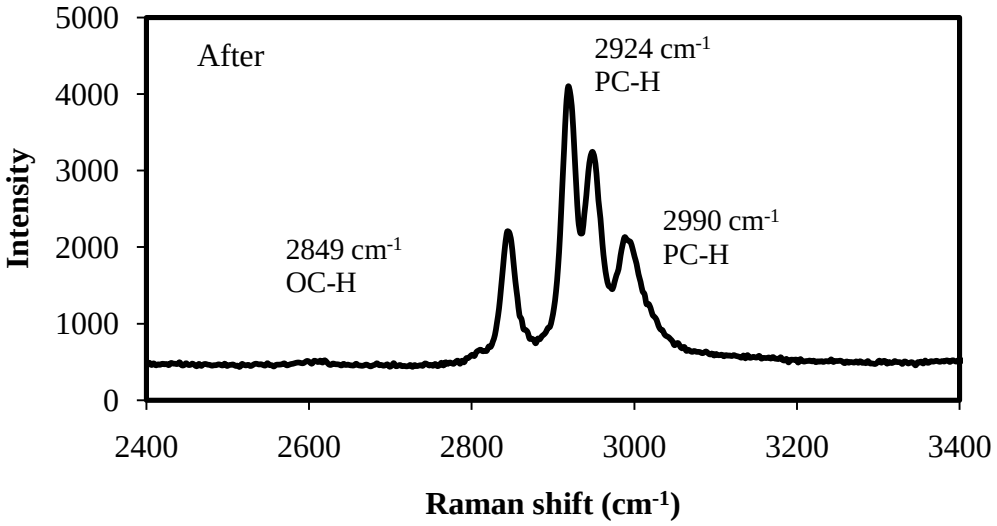

Figure 2.22. Raman Spectra of Amorphous Silica before and after Exposure to DMMP

Table 2.5. Peak Formation from Exposure of Amorphous Silica to DMMP and Comparison to the Raman Spectrum of Pure DMMP[181]

Pure DMMP Feature	**Wavenumber (cm^{-1})**	**Wavenumber in Adsorbed Phase (cm^{-1})**	**Shift from Pure DMMP Feature (cm^{-1})**
PC-H	2983	2990	7
PC-H	2916	2924	8
OC-H	2843	2849	6

The shift observed for the OC-H feature suggests that the DMMP interaction with amorphous silica could also occur with the methoxy O atom. This was observed for the other OPs investigated in this study as well. This result confirms that the less favorable interaction between the methoxy O atom of DMMP and a-SiO_2 does

occur. This interaction will lead to differences in the adsorption energies as compared to that which was predicted using the computational methods.

2.5 Conclusions

Quantitative evaluations of the experimental adsorption of DMHP, DMMP, and TEP by hydroxylated surfaces of amorphous silica were performed in this work. In summary, the experimental heats of adsorption for TEP (the largest OP), DMMP, and DMHP (the smallest OP) became more negative as the molecular size increased. A more negative heat of adsorption is suggestive of a stronger interaction between the OP and the surface.

Experimental results were compared with computational chemistry data obtained for the adsorption of OP compounds onto a-SiO_2 to determine if the trends in adsorption energetics could be accurately predicted. In general, DFT predictions of the heat of adsorption were the more negative for the larger of the five OPs investigated and the less negative for the smaller OPs. The DFT results accurately predicted the trends observed in the changes in energetics deduced from the empirical data. The magnitudes of the computationally determined heats of adsorption were offset from those obtained experimentally due to the surface heterogeneity which was not fully accounted for in the DFT studies. Nevertheless, computational tools were shown to be valid for the purpose of comparative analysis when systems of similar chemistries are investigated. It should also be noted that both the experimental and computationally determined heat of adsorptions fall into the range expected for physisorption, which is the observed

mechanism of adsorption in the experiments. Based on these results, one could expect computational tools to reasonably allow for a comparative evaluation of the interactions of other OPs-oxide systems.

CHATPER 3

THEORETICAL DETERMINATION OF THE ADSORPTION OF DMHP, DMMP, DMEP, DEEP, AND TEP ON m-ZrO_2: A COMPARATIVIE ANALYSIS TO γ-Al_2O_3 and a-SiO_2

3.1 Introduction

Oxide materials have been well-known for their ability to interact with OPs and demonstrated promising characteristics for the control of OPs[1-35]. Pure oxides that were reported to interact with OPs include Al_2O_3, TiO_2, SiO_2, WO_3, Y_2O_3, CeO_2, FeO, CuO, In_2O_3, SnO_2, and MgO. Recall that both physisorption and chemisorptions were reported for these oxides[38-71].

In the present work, the interactions between ZrO_2 and OPs are investigated. Five OPs of interest, including DMHP, DMMP, DMEP, DEEP, and TEP are studied. The interactions of the five OPs of interest with zirconia have not been reported in the available literature. For this evaluation of zirconia, the thermodynamic heats of adsorption for OP interactions with zirconia are compared with adsorption by alumina and silica. Alumina was chosen as an example of chemisorption whereas silica, investigated in the previous chapter, was chosen as example of physisorption. It is hypothesized that zirconia has the potential to provide for the effective sorption of OP compounds in a manner that is superior to that of the silica surfaces due to the presence of Lewis acid sites and better bonding ability compared with the Lewis acid sites of alumina due to the surface charge of the zirconium ion when coordinated in the oxidized form.

Empirical data are available for the interactions of DMMP with both silica and alumina, as well as for the interactions of nitroaromatic OPs with zirconia[24,38-41,52-54,118,119,120]. However, qualitative and quantitative evaluations of the interaction not have been reported for any OPs studied in this work with zirconia. Therefore, the mechanism of interaction, the strength of the interaction, as well as how zirconia's performance compares to other oxides is unknown. Computational chemistry investigations have been reported for the interactions of DMMP with silica and alumina[1,121,122,123]. However, neither experimental nor computational chemistry investigations of the energetics of DMHP, DMEP, DEEP, and TEP interactions with silica or alumina have been published. Hence, this work also extends the available database of information for silica and alumina, thereby enhancing the ability to develop structure response predictions for new OPs.

In the previous chapter, the validity of computational chemistry methods for the purpose of comparative analysis was demonstrated since the DFT methods were able to accurately predict the experimental trends. Therefore, computational chemistry methods are utilized for this evaluation of zirconia and theoretical models of alumina and zirconia clusters with identical sizes (i.e. same number of Lewis acid sites) are utilized for comparative analyses. Zirconia can exist in three different phases (e.g. monoclinic, tetragonal, and cubic). The monoclinic phase of zirconia (m-ZrO_2) is investigated for its room temperature stability. Alumina can also exist in different phases. The transitional γ-alumina is investigated for its utility in catalysis. Computational chemistry investigations have been reported for

the theoretical modeling of m-zirconia and γ-alumina. The available literature studies are briefly reviewed in the following sections.

Theoretical modeling of zirconia

Numerous computational studies have been published on the lattice dynamics of zirconia models[44-51]. These models include hydroxylated and bare surfaces of various sizes (e.g. slabs and clusters) and phases (e.g. monoclinic, tetragonal, and cubic). The availability of these well-studied models provides crucial information to the stability and the structure of zirconia.

Among the literature on m-zirconia, predictions of phase stability and phase dynamics of zirconia have been examined using density functional theory (DFT). Kuwabara et al. performed lattice dynamic calculations for the phase stability of zirconia using DFT; bulk models of cubic, tetragonal, and monoclinic zirconia were examined[182]. The bulk models, represented by supercells, were optimized and their respective lattice parameters were reported. The lattice parameters for m-zirconia, the phase of interest in this work, are shown in Table 3.1. The authors also examined the phase transformation dynamics of zirconia and concluded that their results agreed with the experimental data and other calculations[183,184,185,186,187,188,189].

Christensen and Carter[7] also investigated the phase stability for bulk zirconia, and in addition, the surface models of ZrO_2 in the monoclinic, tetragonal, and the cubic phases. The optimized bulk structures were "cut" into 10 Å slabs for the 17 unique surfaces (i.e. 3 for cubic, 5 for tetragonal, 9 for monoclinic)[7]. Energies were

calculated using DFT for each of these surfaces. The ($\bar{1}$11) surfaces of m-zirconia, illustrated in Figure 3.1, was determined to be the most stable surface. The authors concluded that the computational surface energies were in good agreement with empirical data.

Table 3.1. Unit Cell Lattice Parameters for Monoclinic ZrO_2 Model

Property / parameter	**Kuwabara et al.** [182]
Space Group Symmetry	$P2_1/c$
a (Å)	5.211
b (Å)	5.286
c (Å)	5.388
α	90.0°
β	99.590°
γ	90.0°
Zr (x, y, z)	(0.277, 0.043, 0.210)
O1 (x, y, z)	(0.070, 0.336, 0.343)
O2 (x, y, z)	(0.450, 0.758, 0.478)

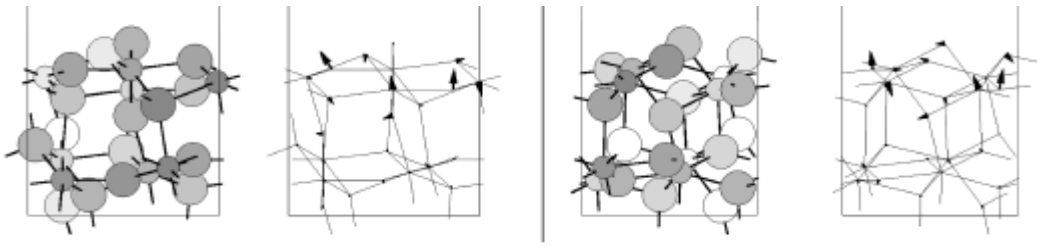

Figure 3.1. ($\bar{1}$11) Surface of Monoclinic ZrO_2 obtained from Christensen and Carter[7] viewed from two Different Angles

Theoretical modeling of alumina

γ-Alumina is one of the intermediate phases in reaching the energetically favorable α-alumina. γ-Alumina is thermodynamically less stable than the α form, but it has proven its prominence and utility in catalysis[190]. Since γ-alumina is a transition alumina and does not exist in a single pure-crystal form, difficulties exist in resolving its structure by experimental methods[190]. First principle methods have been utilized to propose possible structures for γ-alumina. In general, a defective cubic spinel model[191] and a non-spinel model[190] have been proposed.

The defective cubic spinel model is based on a spinel lattice, AB_2O_4, where A denotes a tetrahedral cation site, B denotes octahedral cation sites, oxygen atoms are fourfold coordinated, and vacancies are present to arrive at the stoichiometric Al_2O_3. Mo et al.[192] and Gutierrez et al.[193] investigated different vacancy configurations which could exist in a bulk spinel model and concluded that Al vacancies at the octahedral sites yielded the most favorable structure. Pinto et al.[191] investigated the stability of bulk and surface models of the spinel γ-alumina; comparative evaluations of the (111), (001), (110), and (150) surfaces were presented. Geometry optimization of the bulk model resulted in a unit cell described by the lattice parameters listed in Table 3.2. In the model proposed by Pinto et al[191], the Al vacancies were also located at the octahedral sites. The surface slabs cut from the optimized bulk structure and first principle calculation indicated that the (111) and (001) surfaces were energetically favorable in the spinel model[191].

The non-spinel model suggests several alternative crystal structures for γ-alumina. The Al are also located in octahedral or tetrahedral cation sites for the non-spinel model. The oxygen atoms, however, are not limited to four-fold coordination. Several studies investigated bulk non-spinel γ-alumina models and arrived at a monoclinic or a tetragonal structure of the $I4_1/amd$ space group symmetry with lattice parameters similar to those reported by Ching[190], also listed in Table 3.2[190,194,195,196]. Bulk non-spinel models have also been investigated by computationally simulated dehydration of boehmite[197,198,199]. Digne et al.[198] simulated the dehydration process and obtained a monoclinic non-spinel model described by the lattice parameters in Table 3.2.

Sun et al.[200] evaluated both spinel and non-spinel models and compared the models to XRD data. Based on this comparison, the non-spinel model was found to be an inaccurate representation. These remarks were rebutted by Digne et al.[199] on the grounds that the commercial γ-alumina model referenced by Sun et al.[200] was not well characterized as being strictly present as the γ-alumina form. Paglia et al.[201] also rebutted the results of Sun et al.[200] with similar remarks. With these unresolved discrepancies, both models are still being utilized and referenced in currently published computational studies on the adsorption of molecules such as water and carbon monoxide onto γ-alumina.

Table 3.2. Unit Cell Lattice Parameters for γ-Al_2O_3 Model

Property / parameter	**Spinel model** Pinto et al. [191]	**Non-spinel model** Ching et al. [190]	Digne et al. [198]
Space Group Symmetry	C2/m	$I4_1$/amd P1	P21/m
a (Å)	5.663	5.606	5.587
b (Å)	5.663	5.570	8.413
c (Å)	13.710	13.482	8.068
α	90.6	89.4	90.0
β	90.6	90.0	90.6
γ	60.4	120.0	90.0

3.2 Computational Details

All calculations were performed with the Gaussian 03 computational package[129]. The geometries of each of the OPs and the surfaces were individually optimized. The OP-surface pairs were subsequently optimized with the optimized surface and the lowest energy conformer of the OPs as the starting structures. Upon completing the geometry optimizations of the OPs, the surfaces, and the OP-surface pairs, frequency calculations were performed to determine the thermodynamic parameters associated with their interactions.

DMHP, DMMP, DMEP, DEEP, and TEP

DMHP, DMMP, DMEP, DEEP, and TEP can exist as one of multiple low energy conformers[131,132,133,134,135]. The lowest energy conformer was the focus of this work. This study investigated the interaction of the alumina and zirconia surfaces with the most favorable conformer for each OP. The geometries of DMHP, DMMP, DMEP, DEEP, and TEP were optimized using density functional theory (DFT) with the B3LYP functional and a 6-31G (d) basis set. This functional and basis set have previously been utilized by Yang et al. to model DMMP[135].

Zirconia

The Zr Lewis acid site was the active site of interest in this study. The most energetically favorable ($\bar{1}11$) surface[7] of monoclinic zirconia was modeled. A 2 x 2 x 2 cell with unit cell lattice parameters that were listed in Table 3.2, as determined by Kuwabara et al[182], were utilized to construct the cluster model of zirconia.

The 2 x 2 x 2 cell was "cut" along the plane corresponding to the ($\bar{1}11$) Miller indices and excess atoms were removed to form a cluster model consisting of 8 Zr atoms and 16 oxygen atoms. One of these Zr atoms was selected as the active site for adsorption. The model was optimized using DFT with the B3LYP functional coupled with the LanL2DZ effective core pseudopotential (ECP) basis set. Previous work on Zr also utilized the LanL2DZ basis set[126,202,203,204,205,206,207,208].

Alumina

Although there are controversies on the validity of the cubic spinel representation for γ-alumina, this model was chosen for the investigation of OP adsorption on alumina. The cubic spinel model was utilized in computational studies of sarin and DMMP adsorption, and the results obtained in those studies were in agreement with experiments[121].

The Al Lewis acid site of γ-Al_2O_3 was the active site of interest in this study. Specifically, the active site located on the (111) surface of the model was investigated since the (111) surface is the most stable surface of γ-Al_2O_3[191]. A 2 x

2 x 2 cell with the unit cell parameters obtained from Pinto et al.[191] as listed in Table 3.2 was constructed. The 2 x 2 x 2 cell was "cut" along the (111) plane and excess atoms were removed to obtain a cluster model consisting of 8 Al atoms and 12 oxygen atoms. Two of the 8 Al atoms are in the tetrahedral coordination, and one of these two Al atoms was used as the active site for OP interaction. The geometry of the cluster model was optimized using DFT with B3LYP / 6-31G (d). Previous work by Bermudez et al. determined the validity of the computational method that was utilized [121,122,123].

Energies

Subsequent to the geometry optimization, the energies of the different surfaces (i.e. alumina, zirconia), OPs (i.e. DMHP, DMMP, DMEP, DEEP, and TEP), and surface-OP pairs were determined. The functional and basis sets that were utilized for the geometry optimizations of the surfaces were utilized for the single point energy calculations.

3.3 Results and Discussion

Geometries of DMHP, DMMP, DMEP, DEEP, and TEP

The optimized structures for DMHP, DMMP, DMEP, DEEP, and TEP are illustrated in Figure 3.2.

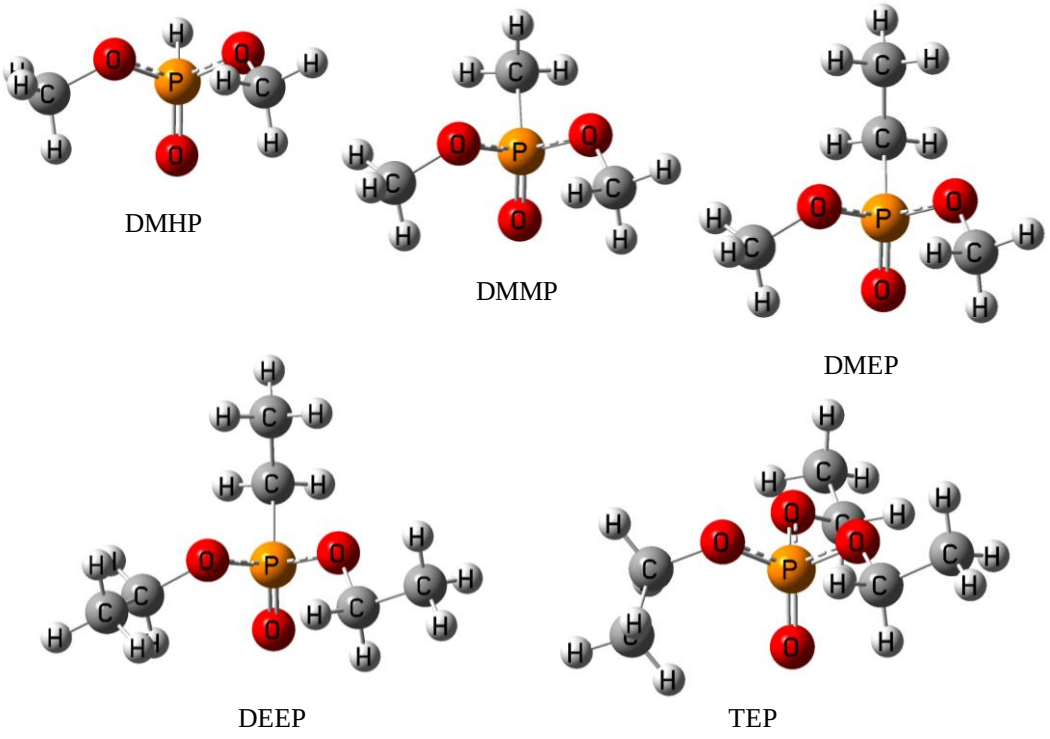

Figure 3.2. Optimized Structures for DMHP, DMMP, DMEP, DEEP, and TEP

DMMP was known to be a strong hydrogen-bonding base due to the oxygen atom of the phosphonyl group[84,26]. The charges for the O atom of the phosphonyl groups were determined to provide insights on the basicity of the OPs; these charges are shown in Table 3.3. The basicity of the OPs increased as the oxygen atom's charge became more negative. As seen in Table 3.3, DMHP was the least basic of the five OPs of interest and TEP was the most basic. The trend in basicity was likely a result of the contribution of the alkyl (i.e. –R) and the alkoxy (i.e. –OR) group; the larger –R and –OR altered the charge of the central P atom which in turn affected the charge of the phosphonyl O atom.

Table 3.3. Calculated Charge for the O Atom of the Phosphonyl Group (P=O) within the OP Molecule Studied

OP molecule	Charge of O atom of P=O
DMHP	-0.559
DMMP	-0.568
DMEP	-0.567
DEEP	-0.570
TEP	-0.591

Geometries of m-Zr_8O_{16} and γ-Al_8O_{12} clusters

Optimization of the zirconia and alumina surface resulted in numerous bond rotations and extensions. The optimized zirconia and alumina cluster models are illustrated in Figures 3.3 and 3.4, respectively.

The Al / O and the Zr / O arrangements in these cluster models were in agreement with existing literature[7, 121,191].

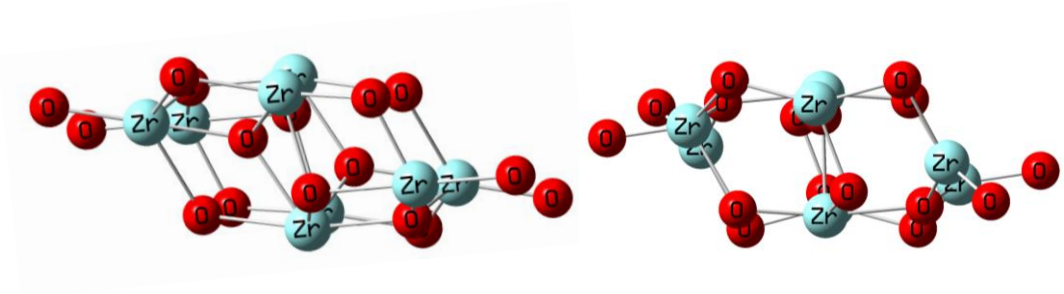

Figure 3.3. Side Views of the Cluster Models for Monoclinic Zr_8O_{16} before and after Optimization. The Energetically Favorable Plane (i.e. the $(\bar{1}11)$ plane) is Facing Upward. The Lewis Acid Site is located on the Surface of Plane

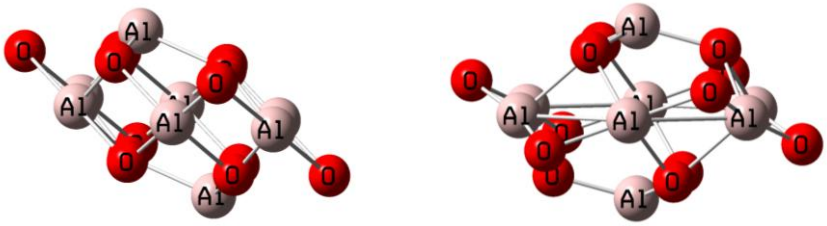

Before After

Figure 3.4. Side Views of the Cluster Models for γ-Al_8O_{12} before and after Optimization. The Energetically Favorable Plane (i.e. the (111) plane) is Facing Upward. The Lewis Acid Site is located on the Surface of Plane

Adsorption of OPs onto the monoclinic Zr_8O_{16} cluster

Interactions between the most stable ($\bar{1}11$) surface of monoclinic zirconia and DMHP, DMMP, DMEP, DEEP, and TEP were investigated with DFT methods. The optimized Zr_8O_{16} cluster, as illustrated in Figure 3.3, was utilized for the geometry optimization for the OP-zirconia pairs. The optimized geometries for the interactions are illustrated in Figure 3.5 (the bond lengths and bond angles can be found in Tables A.4 – A.8 in the Appendix).

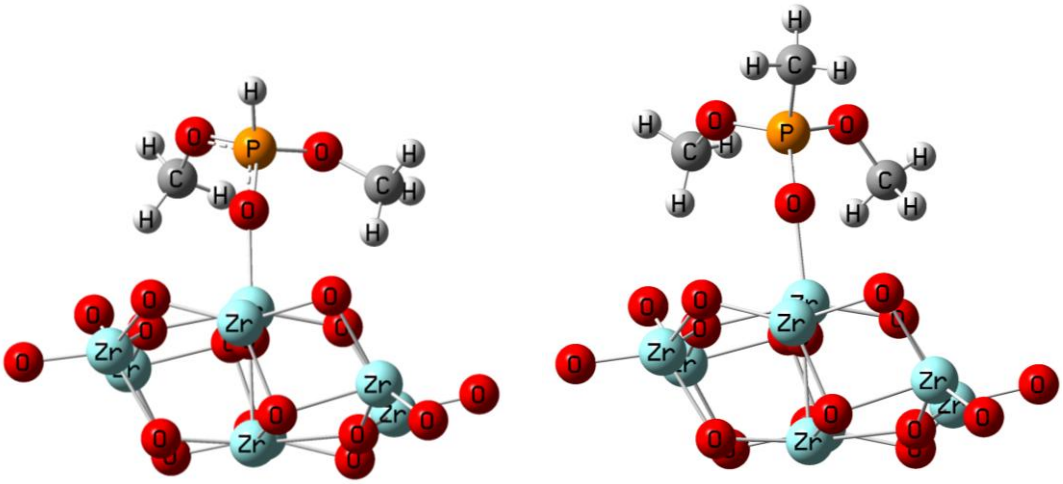

DMHP DMMP

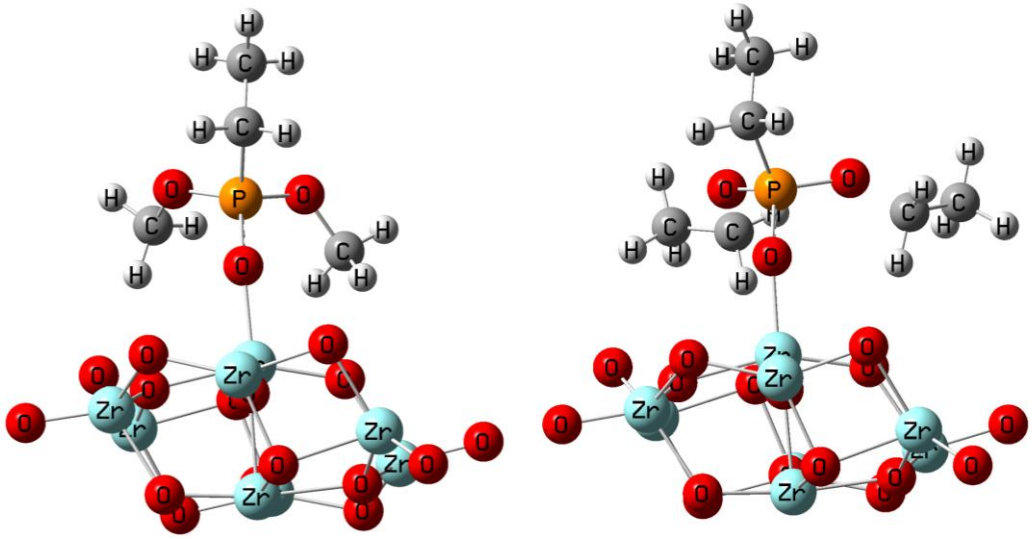

DMEP DEEP

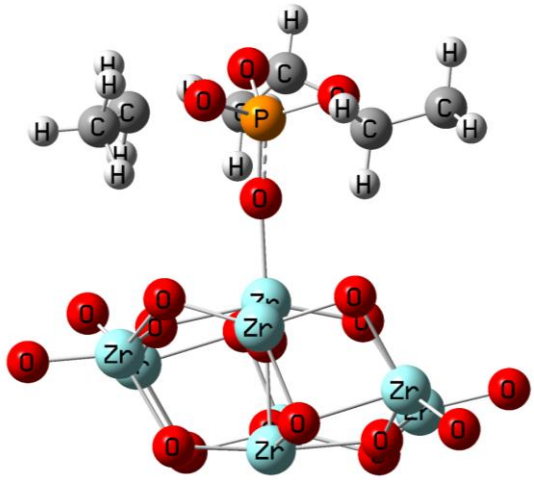

TEP

Figure 3.5. Optimized Geometries for the Adsorption of DMHP, DMMP, DMEP, DEEP, and TEP on a Zr Lewis Acid Site located on the ($\bar{1}$11) Surface of m-Zr_8O_{16}

As seen in Figure 3.5, bond formation occurred when the computational surface of m-Zr_8O_{16} was exposed to the OPs. This bonding interaction occurred between the Zr Lewis acid site and the phosphonyl O atom of the OPs. These results were indicative of strong chemisorption. In the case of DEEP and TEP, it is notable that

the ethyl group (i.e. $–C_2H_5$) of the ethoxy groups (i.e. $-OC_2O_5$) detached from the central phosphorous atom. This suggested that dissociation could potentially occur on an equivalent experimental surface.

To determine how interactions compared between the different OPs and how the m-Zr_8O_{16} surface compared with other oxides (i.e. alumina and silica), quantitative indications of the strengths of the interactions (i.e. heats of adsorption) were determined. The heat of adsorption was determined by Equation 3.1, and calculated values for the OP interactions with m-Zr_8O_{16} are provided in Table 3.4.

$$H_{ads} = H(cluster + OP\ compound) - H(cluster) - H(OP\ compound) \quad \text{(Equation 3.1)}$$

Table 3.4. Calculated ΔH_{ads} for OP Adsorption on m-Zr_8O_{16}

OP compound	**ΔH_{ads} (kcal/mol)**
DMHP	-77.6
DMMP	-80.7
DMEP	-81.3
DEEP*	-83.4
TEP*	-80.6

* all ethyl groups of the ethoxy groups detached after optimization

The OP compounds were arranged in Table 3.4 in order of increasing size (i.e. DMHP < DMMP < DMEP < DEEP < TEP). In general, the heat of adsorption became more negative as size increased, with the exception of TEP. More negative heats of adsorption are associated with stronger interactions. It is notable

that with the increase in molecular size, the OPs also became more basic, as evidenced by the charges of the O atoms that were shown in Table 3.3. Variation in the strength of the interaction for TEP could have resulted from a reduction of the basicity of the phosphonyl O atom with the loss of the ethyl groups. This reduction in basicity would lead to a weakening of the bond between the phosphonyl O atom and the surface Zr Lewis acid site.

Comparison to adsorption of OPs onto γ-Al_2O_3 and a-SiO_2

The ability of zirconia to form strong interactions with the OPs (DMHP, DMMP, DMEP, DEEP, and TEP), has been demonstrated using computational chemistry methods. To determine how the calculated strengths of interaction compare with those of other oxides (i.e. alumina and silica), an alumina cluster of equivalent size (i.e. same number of Lewis acid sites) was investigated. A comparison to the previously determined computational work on silica was also performed.

Interactions between the most stable (111) surface of γ-Al_2O_3 and DMHP, DMMP, DMEP, DEEP, and TEP were investigated using DFT methods. The optimized Al_8O_{12} cluster, as illustrated in Figure 3.4, was utilized for this study. The optimized structures are illustrated in Figure 3.6 (bond lengths and bond angles are available in Tables A.4 – A.8 in the Appendix).

Bonds were formed when the Al Lewis acid sites were exposed to DMHP, DMMP, DMEP, DEEP, and TEP. This was in agreement with existing experimental and computational work on DMMP[121,122,123,38,41,40,24,39]. Bond formation indicated that adsorption of the OP occured by a strong chemisorption route. The interaction

strengths were quantitatively represented by the calculated heats of adsorption (using Equation 3.1), and the results are listed in Table 3.5. The data were subsequently compared to the data obtained using the zirconia surface.

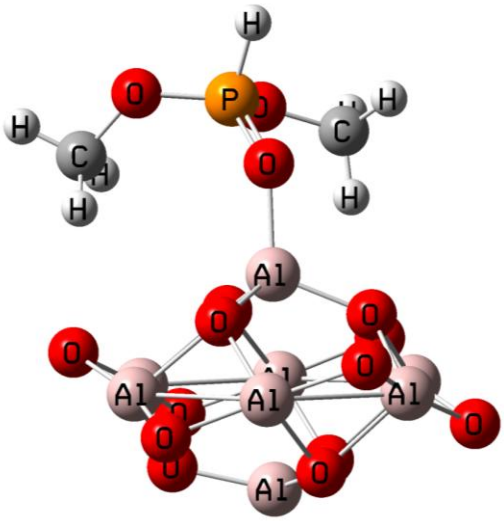

DMHP

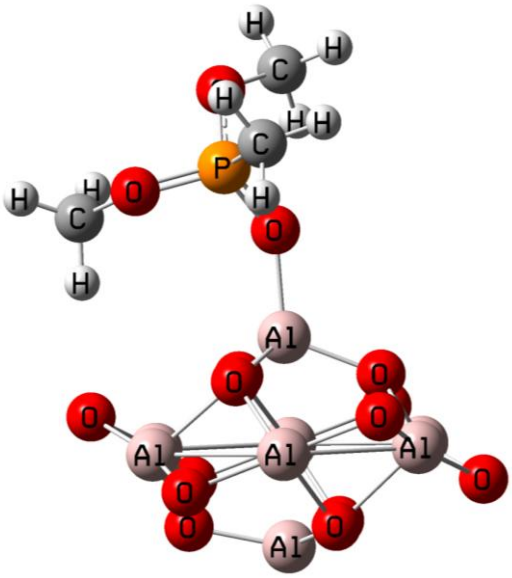

DMMP

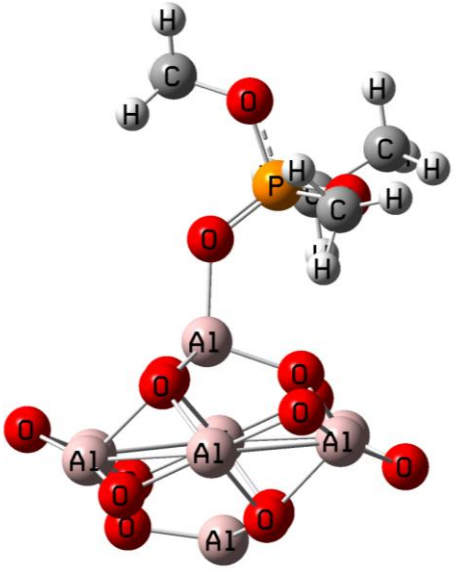

DMEP

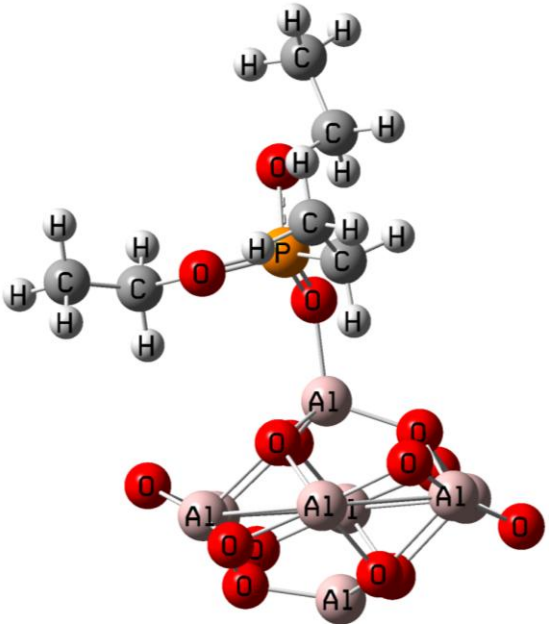

DEEP

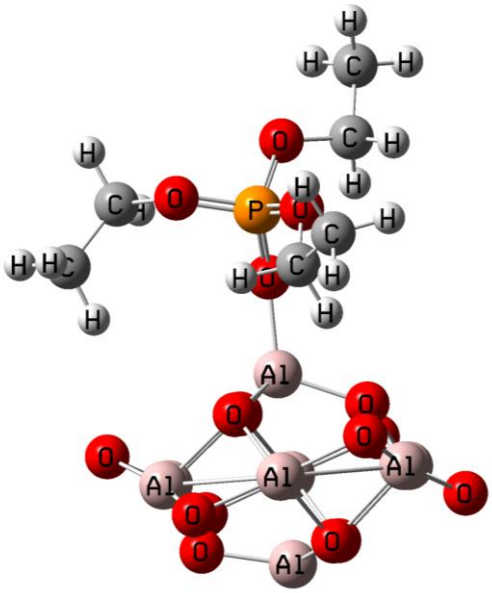

TEP

Figure 3.6. Optimized geometries for the adsorption of DMHP, DMMP, DMEP, DEEP, and TEP on an Al Lewis acid site located on the (111) surface of γ-Al_2O_3

Bermudez[121,122] investigated the adsorption of trichlorophosphine oxide (TCPO), trimethylphosphine oxide (TMPO), dimethyl methylphosphate (DMMP), and sarin onto the (111) surface of γ-Al_2O_3 . Isosteric heats of adsorption of -56.1 kcal/mol and -57.5 kcal/mol were reported for the chemisorption of DMMP onto an Al_8O_{12} cluster (represented by the 6-31G(d) basis set) and an $Al_{20}O_{30}$ cluster (represented by the 6-31G(d) and 3-21G basis sets), respectively. The result obtained in this study for DMMP interaction with the alumina surface was in good agreement. A general trend of a more negative heat of adsorption with an increase in molecular size was also observed for alumina. In comparison to the results obtained for OP interaction with zirconia, the heats of adsorption for interaction with the five OPs

of interest were consistently less negative for alumina. This result suggested that zirconia formed stronger interactions with the OPs investigated in this work.

Table 3.5. Calculated ΔH_{ads} for OP Adsorption onto an Al_8O_{12} cluster

OP compound	**ΔH_{ads} (kcal/mol)**
DMHP	-61.0
DMMP	-62.8
DMEP	-63.0
DEEP	-64.2
TEP	-64.1

DFT predictions of the heats of adsorption for OP interactions with silica were investigated and reported in the previous chapter; the heats of adsorption obtained from our previous work are listed in Table 3.6. In comparison to the results obtained for zirconia and alumina, the heats of adsorption for interactions with silica were the most positive. The heats of adsorption for interactions with alumina were less positive as compared to silica, and the heats of adsorption for interactions with zirconia were the most negative among the three oxides. In comparing the interactions of the OP compounds of interest in this work, i.e. DMHP, DMMP, DMEP, DEEP, and TEP, with zirconia, alumina, and silica, computational chemistry suggested that zirconia formed the strongest interactions.

Table 3.6. Calculated ΔH_{ads} for OP Interactions with Silica

OP compound	**ΔH_{ads} (kcal/mol)**
DMHP	-16.8
DMMP	-19.7
DMEP	-19.4
DEEP	-21.4
TEP	-21.7

In an attempt to explain the differences in interaction strengths, the charges for the active sites for the silica, alumina, and the zirconia cluster models were investigated. The cluster models are shown with their charges in Figure 3.7. The Zr and Al active sites had charges of 1.686 e and 1.102 e, respectively. The two interacting –OH sites on silica had charges of 0.44 e and 0.43 e.

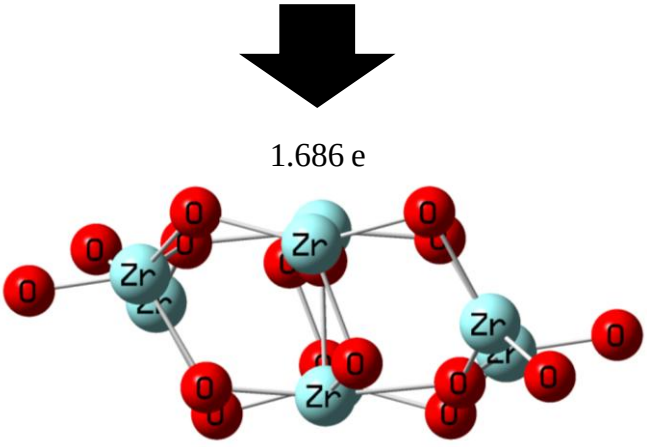

m-Zr_8O_{16}

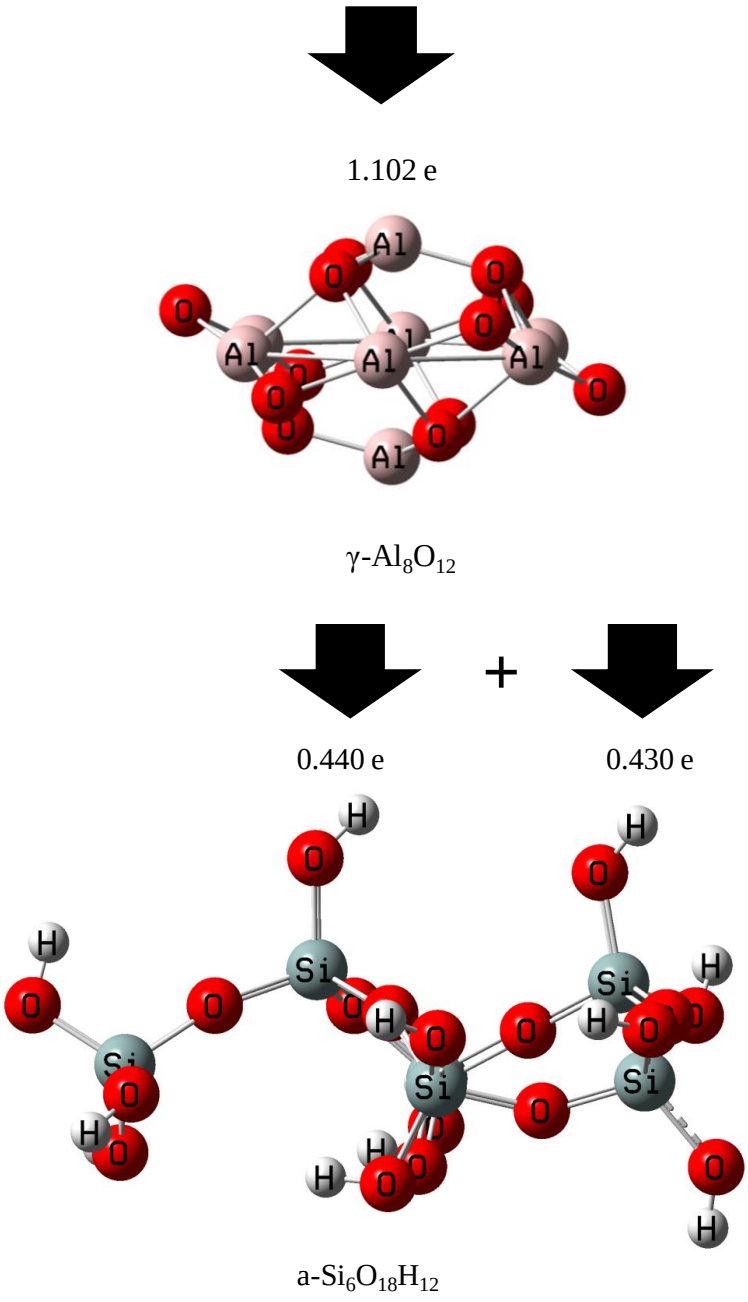

Figure 3.7. Illustration of the Charge Distribution on m-Zr_8O_{16}, γ-Al_8O_{12}, and a-$Si_6O_{18}H_{12}$

The magnitude of the positive charge on the sites of interaction (marked with arrows in Figure 3.7) provided a measure of the site acidities of the surface interacting sites. The computational modeling suggested that the Zr Lewis acid

site was more acidic than the Al Lewis acid site or even the two bonding hydrogens of the a-SiO_2 clusters (recall that OPs interact with a-SiO_2 via hydrogen bonding through the surface -OH). As previously mentioned, DMMP was known to be a strong hydrogen-bonding base, and the other OPs investigated in this study were similarly basic as shown by the charges listed in Table 3.3. Since a strong hydrogen-bonding base favors interaction with a strong hydrogen-bonding acid, the interactions of OPs is suggested to be stronger (i.e. a more negative heat of adsorption exists) for the more acidic Zr Lewis acid site as compared to the Al sites or available acidic bonding sites on the a-SiO_2 (quantification of the effects of the active sites' acidities on the charge transfers between the sites and the OPs are in the Appendix).

3.4 Conclusions

The mechanisms of interaction of DMMP, DMEP, DEEP, and TEP adsorption onto zirconia were investigated. A monoclinic zirconia cluster was constructed in this DFT study, and its interactions of the selected OPs with the m-ZrO_2 surface were determined to occur between the phosphonyl O atom of the OPs and the Zr Lewis acid site of the surface.

The heats of adsorption for the adsorption of OP by m-ZrO_2 were also predicted by computational means in this study, and the result ranged from -77.6 to -83.4 kcal/mol. The heats of adsorption generally increased with an increase in the OP molecular size and suggested that a strong chemisorption process occurred upon interaction with the Zr Lewis acid site. As with the SiO_2 experimental system, the

absolute thermochemical data are expected to vary with surface hydroxylation. Nevertheless, computational tools were shown to be valid for the purpose of comparative analysis when systems of similar chemistries were investigated.

Zirconia results were compared with the results obtained from OP interactions with both γ-alumina and a-silica. Interactions of the OPs with zirconia consistently led to more negative heats of adsorption in comparison to the heats of adsorption for OP interaction with γ-alumina (also determined in this study) and for OP interaction with a-silica (determined in the previous chapter). A more negative heat of adsorption is indicative of stronger interaction strengths, a desirable characteristic for the development of air pollution control technologies. Moreover, some of the calculations suggested dissociative adsorption, thus indicating not only control but destruction of the OP compounds. Based on these computational results, zirconia is suggested to be an effective sorbent material (among silica, alumina, and zirconia) for the control of OP compounds.

CHATPER 4

SYNTHESIS AND APPLICATION OF m-ZrO_2 FOR THE ADSORPTION OF OPs

4.1 Introduction

Monoclinic zirconia (m-zirconia or m-ZrO_2) surfaces were pre-screened using computational tools in the previous chapter. The OPs studied appeared to have a more favorable interaction with the m-ZrO_2 surface as compared to γ-alumina and a-SiO_2 surfaces. In this work, the goal was to synthesize monoclinic zirconia while maximizing the surface area of the material. A high surface area is advantageous in adsorption applications.

Sol-gel methods, co-precipitation, and hydrothermal / solvothermal methods[209,210,211,212,213,8,214] have been successfully used to synthesize monoclinic zirconia. Sol-gel synthesis involves the hydrolysis and condensation reaction of zirconium alkoxide[209], and resulted in the small particle size reported in the literature[209]. For samples of the same mass, smaller particle sizes were associated with higher surface areas[209]. This is an advantage to the use of a sol-gel synthesis method. Pure phase monoclinic zirconia nanoparticles were obtained via sol-gel synthesis[209]; calcination at 1000°C following the synthesis induced the desired phase transformation from the tetragonal phase to the monoclinic phase. Partciles of ~7nm with relatively high surface areas were reported[209]. Drawbacks to this technique included the extreme sensitivity of zirconia to moisture during synthesis, and the cost and toxicity associated with some alkoxides[209,210].

A co-precipitation technique was also explored as a suitable technique for the low cost, mass production of zirconia[211]. An inexpensive zirconium salt such as zirconyl chloride is utilized for the synthesis of zirconia through co-precipitation methods. Co-precipitation by the addition of sodium hydroxide or ammonium hydroxide to the dissolved zirconium salt was reported in the literature[211]. An exchange reaction led to the formation of precipitates in the tetragonal phase[211]. A calcination temperature of 1000°C was required to obtain pure monoclinic zirconia. Large particles (~40 nm) of relatively low surface area were obtained from this technique[211, 212].

Hydrothermal synthesis of monoclinic zirconia[210,213] was reported with the use of zirconyl chloride and zirconyl nitrate salt precursors. The use of these salt precursors is favored since they are inexpensive and nontoxic[210]. This technique involves the hydrolysis of the salt precursors at an elevated temperature, and could be coupled with the addition of solvents in the case of solvothermal syntheses. Li et al.[210] reported the synthesis of pure phase monoclinic zirconia by this technique in the presence of urea (resulting in neutral pH conditions). The synthesis products were calcined at 400°C and m-zirconia particles of ~6 nm with BET surface areas of 130 m^2/g were obtained in their study. Synthesis of pure phase monoclinic zirconia nanoparticles were also reported for hydrolysis of zirconyl chloride in water (resulting in acidic pH conditions) in the absence of other reactants[213]. An advantage to this technique is that calcination is not required to obtain the pure phase monoclinic zirconia materials. As synthesized, particles of 4 nm in size with a BET surface area of 110 m^2/g were reported[213]. Numerous attempts to

synthesize zirconia by hydrolyzing zirconium salts under basic conditions through the addition of ammonia were also reported[210]. Although the tetragonal phase of zirconia is favored at these conditions, pure phase monoclinic zirconia could be obtained by calcining the material at temperatures between 700°C – 1000°C[213,8,214]. However, similar to the other techniques that resulted in the initial formation of tetragonal zirconia, a high calcination temperature was required to generate the m-zirconia. This enhanced calcinations temperature resulted in an increased particle size and reduced surface area (e.g. to reported values of 40 – 60 m^2/g)[213, 214].

Based on these advantages and disadvantages discussed in the existing literature, a hydrothermal method was chosen to produce monoclinic zirconia. Syntheses under both acidic and neutral conditions were achieved in this work. Synthesis under basic conditions (by the addition of ammonia) was not investigated in this work since the formation of the desired monoclinic phase was previously shown to be unfavorable [213-214]. The acidic and neutral conditions were achieved through exclusion and inclusion of urea, respectively. This investigation provides a preliminary investigation on the optimization of the hydrothermal synthesis of m-ZrO_2 nanoparticles by characterizing the effects of various calcination conditions. This work also presents a first investigation on the experimental adsorption of the OPs of interest, including dimethyl phosphite (DMHP), dimethyl methylphosphonate (DMMP), diethyl ethylphosphonate (DEEP), and triethyl phosphate (TEP), by m-ZrO_2.

4.2 Experimental Details

Synthesis and Characterization of Monoclinic Zirconia

Monoclinic zirconia precipitates were synthesized by hydrothermal methods using zirconyl chloride both in the presence and absence of urea. Zirconyl chloride octahydrate of 98% purity and urea of 99.5% purity were obtained from Sigma-Aldrich. Zirconyl chloride (0.4 M), and urea (4 M) for samples synthesized in the presence of urea, were dissolved in nanopure water and heated in a pressure vessel at 160°C for 24 hours. The starting concentration and reaction time were determined from published literature[210]. The resulting precipitates were centrifuged and dried at 80°C overnight. The dried precipitates were analyzed with dynamic thermal analysis to determine the calcination temperature necessary to induce phase transition. The samples were calcined at various conditions and characterized.

Characteristics of interest included the surface area of the samples, the crystallinity of the samples, and the bulk properties of the sample. The surface areas of the samples were determined by BET analysis of N_2 isotherm measurements at 77 K (Micromeritics Tristar II 3020 surface area and porosity system). The measurements were taken immediately after calcination of the samples. The samples were also probed with X-ray diffraction and Raman spectroscopy for the crystallinity and the bulk properties, respectively. X-ray diffraction measurements were taken for 2θ values from 15° to 80° at a resolution of 0.2° on a diffractometer equipped with a CuKα source (Siemens D5000 powder x-ray diffractometer).

Raman spectra were recorded for frequencies between 50 cm^{-1} to 1150 cm^{-1} at a resolution of 1 cm^{-1} on a spectrometer equipped with a 100 mW Compass 532 nm laser.

The morphology of the sample prepared with the chosen calcination condition was also of interest and scanning electron microscopy (SEM) was utilized. The sample was gold-coated and analyzed with a beam acceleration voltage of 7.5 kV.

Characterization of Sample Interactions with the Pure Component Gaseous OPs

Qualitative and quantitative characterizations were performed to determine the mechanism of interaction and the strength of the interaction between the samples and the pure component gaseous OPs (in the absence of other atmospheric constituents). The mechanism of interaction between the OP compounds, dimethyl phosphite (DMHP), dimethyl methylphosphonate (DMMP), diethyl ethylphosphonate (DEEP), and triethylphosphonate (TEP), and the zirconia samples were investigated by Raman spectroscopy (resolution of 1 cm^{-1} on Raman spectrometer equipped with a 100 mW Compass 532 nm laser). The zirconia samples were exposed to the gaseous OPs utilizing the adsorption apparatus detailed in Chapter 2, and analyzed subsequent to the exposures. The samples were exposed to the atmosphere after the OP exposure and while the measurements were made. Raman spectra were obtained for frequencies between 50 cm^{-1} to 4000 cm^{-1} before and after the zirconia was exposed to the OPs. Five accumulative (i.e. co-added) scans were taken for an exposure time of 10 seconds per scan to differentiate between adsorbed OPs and artifacts from the measurement

(i.e. intensities of the peaks associated with the adsorbed OP increases during the five accumulative scans whereas signal intensities does not accumulate for artifacts in the measurements).

The strengths of the interaction between the zirconia samples and DMHP, DMMP, and TEP were also determined using the apparatus and the method described in Chapter 2. In brief, adsorption isotherm measurements were taken using a static volumetric method and measurements were recorded at four temperatures between 23.8°C and 34.6°C. Samples of approximately 0.10 g were loaded into a custom made Pyrex cell, evacuated at 105°C for 45 minutes, and exposed to doses of gaseous OPs, generated from purified liquid OPs, up to the saturation vapor pressures. The adsorption isotherms were compared with isotherm models to obtain a continuous representation of the experimental data, and adsorption isosteres were constructed based on the model representations. The heats of adsorption associated with the interaction between the samples and the OPs were determined from the adsorption isosteres using Equation 4.1,

$$\Delta H = R \left[\frac{\delta \ln P}{\delta \left(\frac{1}{T} \right)} \right]_N \qquad \text{(Equation 4.1)}$$

where R is the gas constant, P is the pressure of the OP exposed to the sample, T is the absolute temperature at which the measurements were taken, and N corresponds to the amount of gas that is adsorbed onto the sorbent at equilibrium (i.e. negligible changes in pressure, specifically, the change in pressure, ΔP, per hour was less than the gauge resolution).

Characterization of Sample Interactions with Gaseous DMMP and Air Mixtures

The performance of the sample for the application of OP pollution control was determined by testing the ability of the sample to adsorb a low concentration of DMMP from a DMMP and air mixture (i.e. in the presence of atmospheric constituents) in a flow system. Gas samples of air and DMMP (~45 parts per million, ppm) were generated by flowing air over 10 μL of liquid DMMP into a Tedlar bag. Mild heat was applied, with a heat gun, to warm an injection port where liquid DMMP was introduced to assist in the volatilization of the liquid DMMP. The gas mixture was then pumped from the Tedlar bag through an enclosed flow tube containing the sample at approximately 2.5 L/min for 5 minutes. Subsequent to exposure to the gaseous DMMP and air mixture in the flow tube, a portion of the sample was analyzed with thermal gravimetric analysis (Setaram TG92 TGA at LeRoy Eyring Center for Solid State Science) up to 700°C at 10°C / minute and the mass loss was compared with that from a sample which was not exposed to the mixture. The resolution of the TGA system is 1 μg. Another portion of the sample was placed in a programmable furnace in a vacuum system, after the exposure to the gaseous DMMP and air mixture, and residual gas analysis (Stanford Research System SRS 200 RGA at LeRoy Eyring Center for Solid State Science) was employed to obtain mass spectra up to 130 m/z which were utilized to identify the desorbents from the sample. The sensitivity of the RGA instrument is on the order of 10^{-10} Torr.

4.3 Results and Discussions

Characterization of Monoclinic Zirconia

Zirconia precipitates were prepared hydrothermally at 160°C with starting concentrations of 0.4 M zirconyl chloride, and 4 M urea for samples synthesized in the presence of urea. For samples synthesized in the absence of urea, the precipitates were soluble in the resulting liquid and were not centrifuged before drying. The precipitates obtained in the presence of urea were insoluble in the resulting liquid and allowed for centrifugation and removal of the resulting liquid prior to drying. Both of the dried precipitates were calcined under the same conditions (i.e. 400°C for 4h in an O_2 environment) and their BET surface areas were analyzed by N_2 adsorption analysis before and after calcination for comparison. For samples obtained subsequent to drying (i.e. before calcination), a higher BET surface area (i.e. 163.44 ± 0.53 m^2/g) was obtained for the precipitates prepared in the presence of urea as compared with the precipitates obtained in the absence of urea (i.e. BET surface area of 104.09 ± 0.52 m^2/g). Subsequent to calcination, decreases in the surface areas were observed for both samples, with a higher surface area (i.e. 115.62 ± 0.36 m^2/g) for the zirconia sample prepared in the presence of urea as compared with the sample prepared in the absence of urea (i.e. BET surface area of 86.85 ± 0.36 m^2/g). A higher surface area is desirable for the adsorption of gases and hence, further evaluations were performed only with the precipitates obtained in the presence of urea.

Additional calcination conditions were evaluated for the precipitates synthesized in the presence of urea. Four samples of precipitates were calcined under flowing O_2 at 400°C for 90h, at 400°C for 4h, and at 300°C for 4h, and in 2000 psi of O_2 at 100°C for 24h, respectively. The flowing O_2 environment was chosen to assist with the removal of impurities that might be present in the samples and to provide an oxygen rich environment which is favorable for the formation of the monoclinic phase [215]. The calcination temperature of 400°C was utilized as a comparison to the reference literature [210]. The calcination temperature of 300°C was chosen to enhance the surface area of the sample. Lower temperatures were not utilized under flowing O_2 because of the result obtained from the dynamic thermal analysis. In brief, a dynamic thermal analysis was performed on the dried precipitates up to 400°C, and the heat flow in and out of the sample was monitored. At ~250°C, a thermal signal was observed, which suggested this as the minimum temperature for phase transition to occur. However, 100°C was utilized in combination with 2000 psi of O_2 as the high pressure could potentially be an alternative driving force for phase transition. The calcined samples and two uncalcined samples were characterized with BET N_2 analysis. The BET surface areas and their standard errors are listed in Table 4.1.

Table 4.1. BET Surface Areas of Calcined and Uncalcined Samples

Calcination Condition	**BET Surface Area (m^2/g)**
Uncalcined sample 1	163.44 ± 0.53
Uncalcined sample 2	170.35 ± 0.68
400°C for 90h in flowing O_2	54.32 ± 0.07
400°C for 4h in flowing O_2	115.62 ± 0.36
300°C for 4h in flowing O_2	136.61 ± 0.36
100°C for 24h in 2000 psi O_2	119.16 ± 0.30

The surface areas of two uncalcined samples prepared under identical conditions were measured to obtain the error of imprecision from the BET N_2 adsorption isotherm measurements. The difference between the two surface area measurements was 6.91 m^2/g and will be denoted as the random experimental error for this discussion. For all of the samples, calcination resulted in a loss of available surface area (SA), as expected. For the samples calcined in flowing O_2, surface area decreased with increase in calcinations time and temperature, also as expected. The sample calcined at 300°C for 4h in flowing O_2 resulted in an enhancement of surface area, as desired, compared with the samples calcined at 400°C. The samples calcined at 400°C for 4h in flowing O_2 and at 100°C for 24h in 2000 psi O_2 were comparable in surface area when accounting for the random experimental error. The combination of reduced temperature and elevated pressure did not lead to an enhancement of surface area as desired. Based on these results, the sample calcined at 300°C for 4h in flowing O_2 is superior when considering surface area. However, the crystallinities of the samples should also be taken into account.

The crystallinities of the samples were probed with X-ray diffraction (XRD). The results were compared with a reference spectrum[8] of monoclinic zirconia shown in Figure 4.1. XRD spectra from this work are shown in Figure 4.2. In summary, all of the samples including the uncalcined samples diffracted x-ray at the same 2θ values as the reference spectrum for monoclinic zirconia (verification of the purities of the samples is subsequently discussed). The samples, however, did vary in their degrees of crystallinity. In general, crystallinity increased with the

increase in calcination time and temperature for the samples calcined under flowing O_2. For the sample calcined in 2000 psi of O_2 at 100°C for 24h, the crystallinity of the sample was comparable to the sample calcined at 300°C for 4h.

The synthesis of a high surface area monoclinic zirconia, which is characterized by an abundance of the $(\bar{1}11)$ surface, was the goal of this work. Hence, the XRD spectra were further evaluated at the 2θ value of 28.2° which corresponds to the $(\bar{1}11)$ crystal plane. In Figure 4.2, the peaks for the $(\bar{1}11)$ crystal plane are indicated by an arrow. Taking both surface area and crystallinity into account, the sample calcined at 400°C for 4h was determined to be superior to the other samples prepared under other calcinations conditions due to its prominence of the $(\bar{1}11)$ crystal plane and its reasonable surface area.

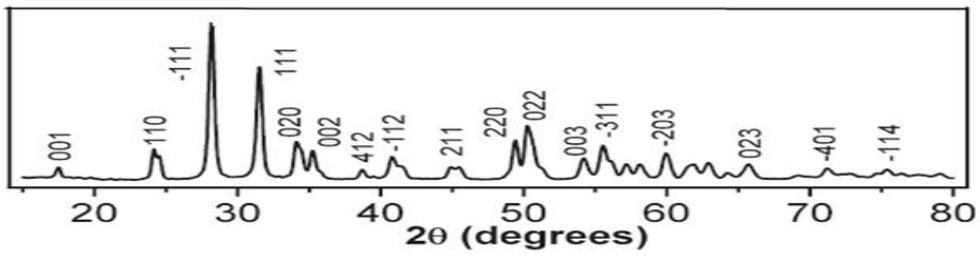

Figure 4.1. Reference Spectrum of Monoclinic Zirconia[8]

Raman spectroscopy was also performed to confirm that impurities were not present in the synthesized samples. Raman spectra of the samples are shown in Figure 4.3. The peaks observed in Figure 4.3 were identified as listed in Table 4.2. It is noted that all peaks observed in the Raman spectra shown in Figure 4.3 corresponded to Raman active modes of monoclinic zirconia (refer to Table 4.2). Hence, it can be concluded that the samples did not contain impurities.

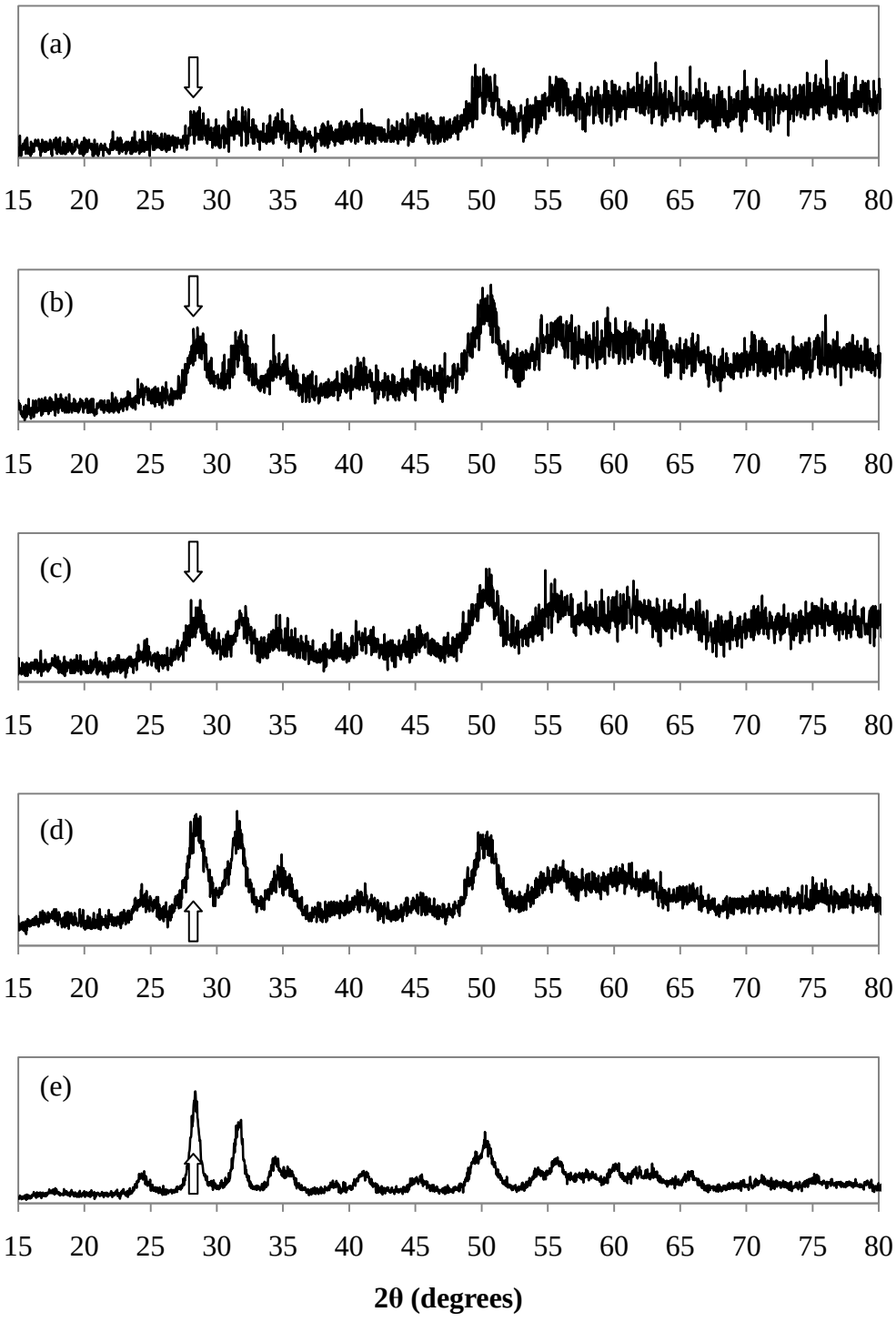

Figure 4.2. XRD Spectra of Zirconia Precipitates (a) before Calcination, and after Calcinations at (b) 300°C for 4h, (c) 100°C for 24h in 2000 psi of O_2, (d) 400°C for 4h, and (e) 400°C for 90h

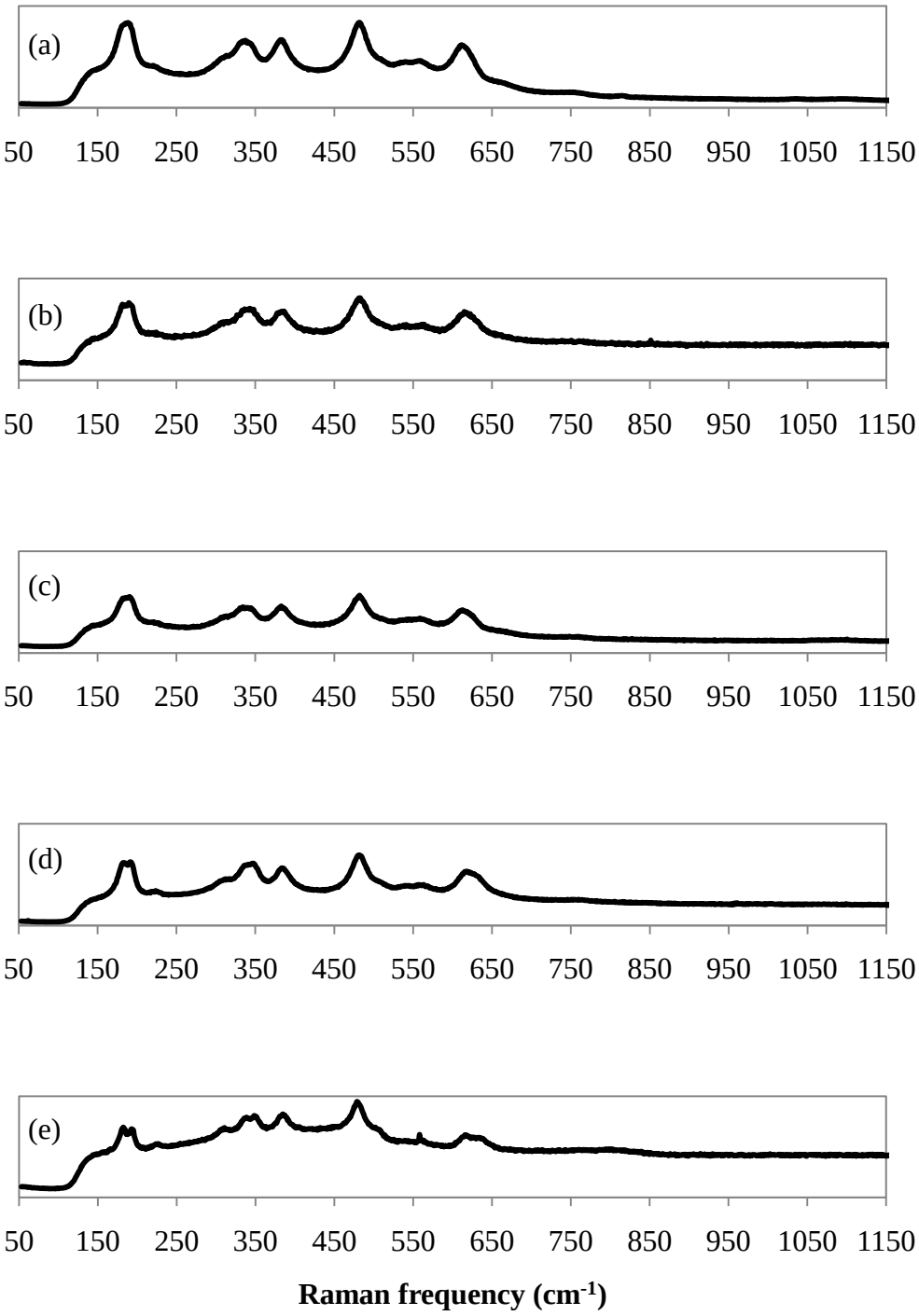

Figure 4.3. Raman Spectra of Zirconia Precipitates (a) before Calcinations and after Calcinations at (b) 300°C for 4h, (c) 100°C for 24h in 2000 psi of O_2, (d) 400°C for 4h, and (e) 400°C for 90h

Table 4.2. Peak Assignment for the Raman Spectra of Samples Calcined at Various Conditions

Reference – Peak Frequency Values (cm^{-1})				**Peak Assignment**	**Our Work – Peak Frequency Values (cm^{-1})**				
Ref 216	*Ref 215*	*Ref 209*	*Ref 217*		*400 C 90 h*	*400 C 4 h*	*300 C 4 h*	*100 C 24 h High P*	*uncalcined*
105	110		100	m-zirconia					
148		149		t-zirconia					
178	181	178		m-zirconia	181	182	181		
189		189	191	m-zirconia	191	191	190	190	185
		220	222	m-zirconia	223	224			
270		269		t-zirconia					
		307	304	m-zirconia	308	309			
309		312		t-zirconia					
333	333	337	335	m-zirconia	336		337	334	334
345			345	m-zirconia	348	345			
382	380	379	380	m-zirconia	383	384	383	383	381
477	475	472	475	m-zirconia	479	480	481	482	480
504			502	m-zirconia	505				
535			536	m-zirconia	537	539	538		533
560	558	558	559	m-zirconia	558	556	560	558	553
614	615		616	m-zirconia	615	616	615	611	611
633		634	636	m-zirconia	631				
	690			m-zirconia					
	760			m-zirconia	751	756			

Based on the surface area measurements, the X-ray diffraction results, and the Raman spectra, the samples calcined at 400°C for 4h in flowing O_2 were deemed to be superior in surface area and in crystallinity. The morphology of a sample prepared under these optimal conditions was characterized. An SEM image of the sample is shown in Figure 4.4.

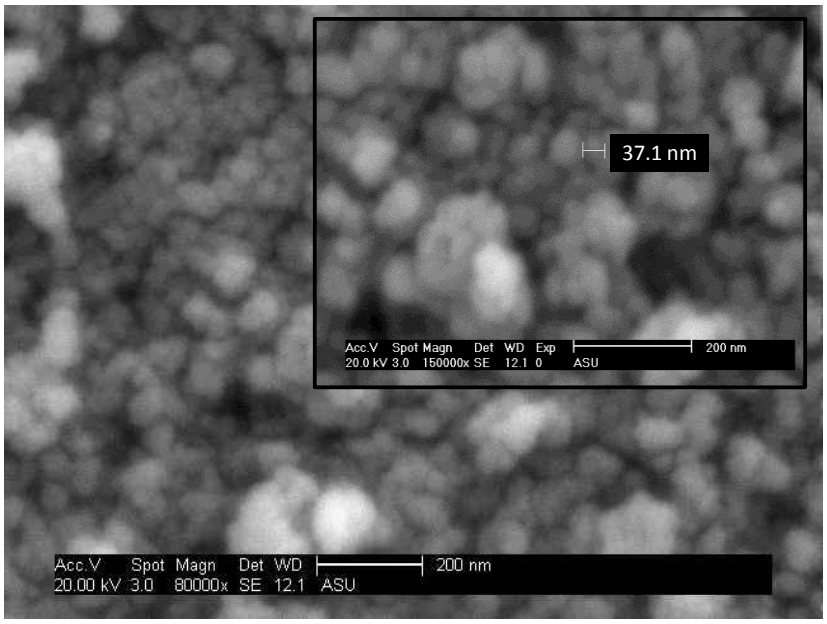

Figure 4.4. SEM Image of Zirconia Nanoparticles synthesized in the Presence of Urea and calcined at 400°C for 4h in Flowing O_2

As seen in Figure 4.4, nanoparticles (NPs) with primary particle diameters of ~37 nm resulted from the hydrothermal synthesis of zirconia in the presence of urea when calcined at the optimal condition (i.e. 400°C for 4h in flowing O_2). Dynamic light scattering (DLS) was also utilized to verify the particle size and the results indicated primary particles of 34 ± 6 nm and larger agglomerates of 175 ± 39 nm and 796 ± 145 nm where the error represented 1σ. In comparison to the

reference literature[210], the nanoparticles obtained in this work were ~30 nm larger in diameter. The surface areas of the nanoparticles, however, were comparable. This suggested that internal pore structures were present and could be accountable for the available surface area. A porosity measurement (determined by BET N_2 adsorption analysis on the Micromeritics Tristar II 3020 surface area and porosity system) was performed on the same sample and the result indicated the presence of mesopores of ~10 nm in diameter.

Mechanism of Interactions between m-ZrO_2 NPs and the OPs

Based on the material characterization results, samples calcined at 400°C for 4h in flowing O_2 were utilized for the organophosphorus (OPs) interaction studies. The interactions between four OP compounds, dimethyl phosphite (DMHP), dimethyl methylphosphonate (DMMP), diethyl ethylphosphonate (DEEP), triethyl phosphate (TEP), and the monoclinic zirconia nanoparticles were probed using Raman spectroscopy. Raman spectra of the monoclinic zirconia samples before and after exposure to the OPs are shown in Figures 4.5-4.8.

Exposure of the zirconia samples to the four OPs resulted in multiple peak formations. The spectra were compared with spectra obtained from liquid DMHP, DMMP, DEEP, and TEP and the identifiable peaks were assigned to their respective bonds as listed in Table 4.3-4.6. For comparison, peak formations observed for silica and alumina are also listed. The Raman spectra of the OPs and spectra of silica and alumina before and after OP exposures are in the Appendix.

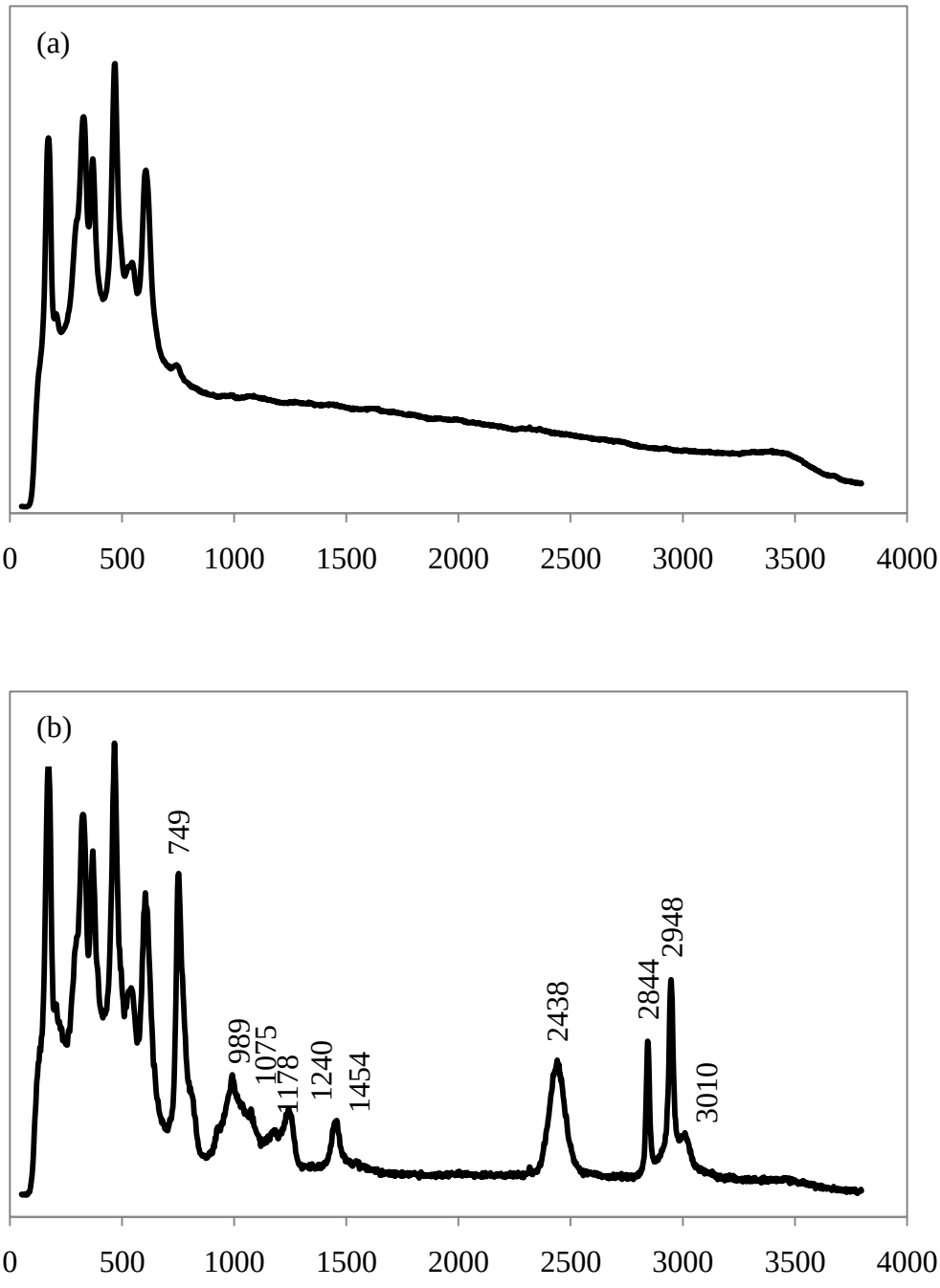

Figure 4.5. Raman Spectra of ZrO_2 (a) before and (b) after Exposure to DMHP

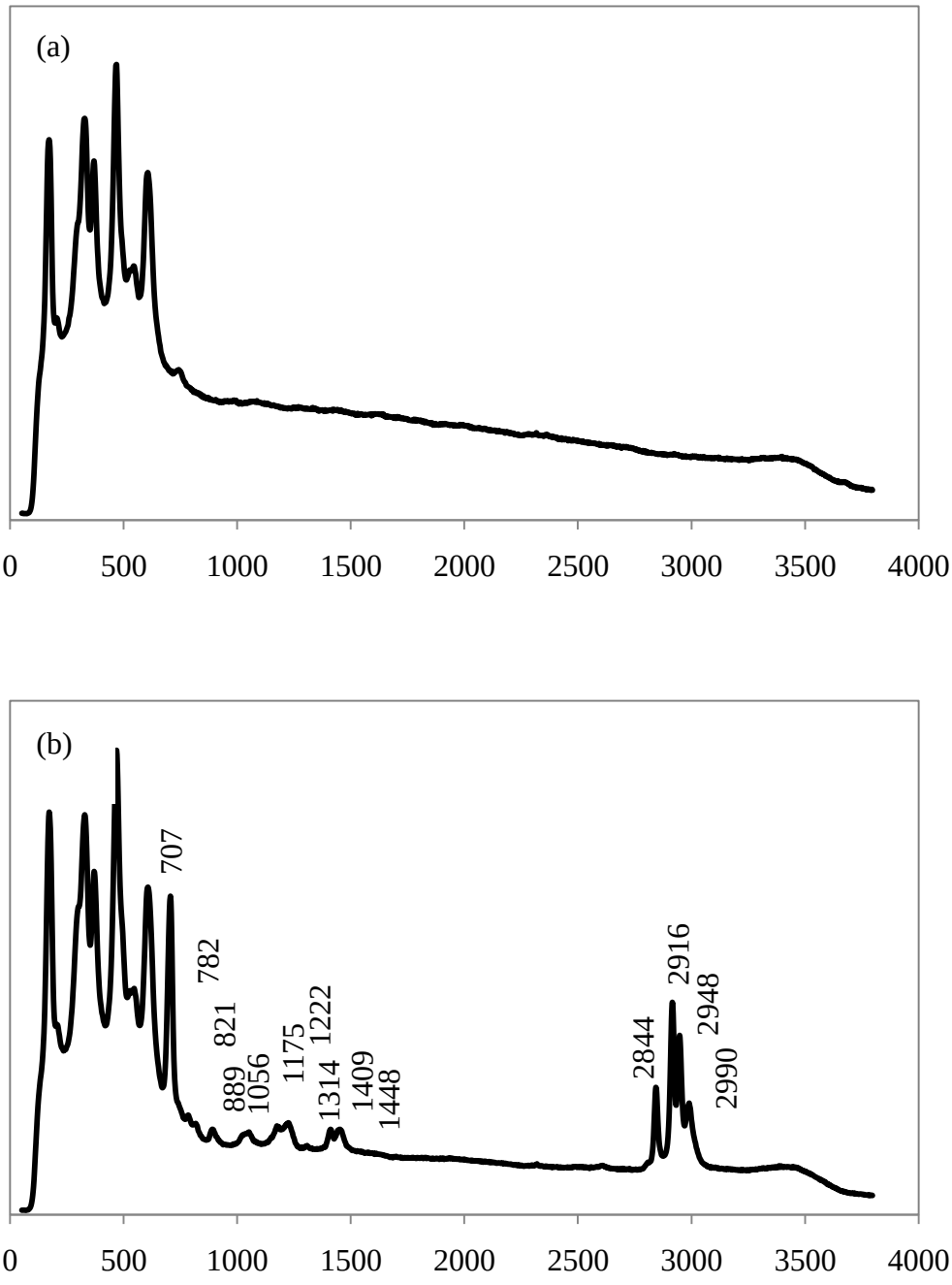

Figure 4.6. Raman Spectra of ZrO_2 (a) before and (b) after Exposure to DMMP

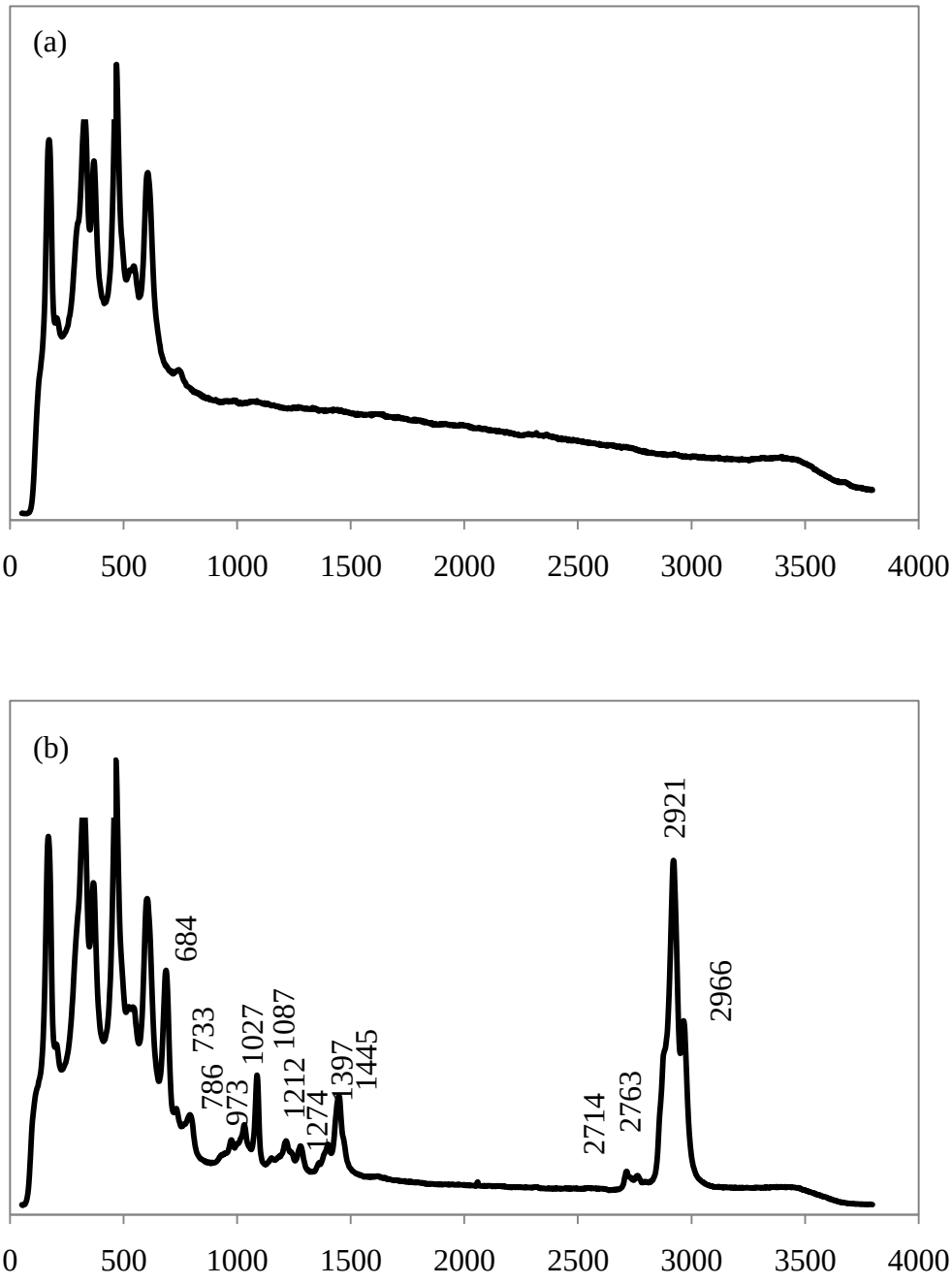

Figure 4.7. Raman Spectra of ZrO_2 (a) before and (b) after Exposure to DEEP

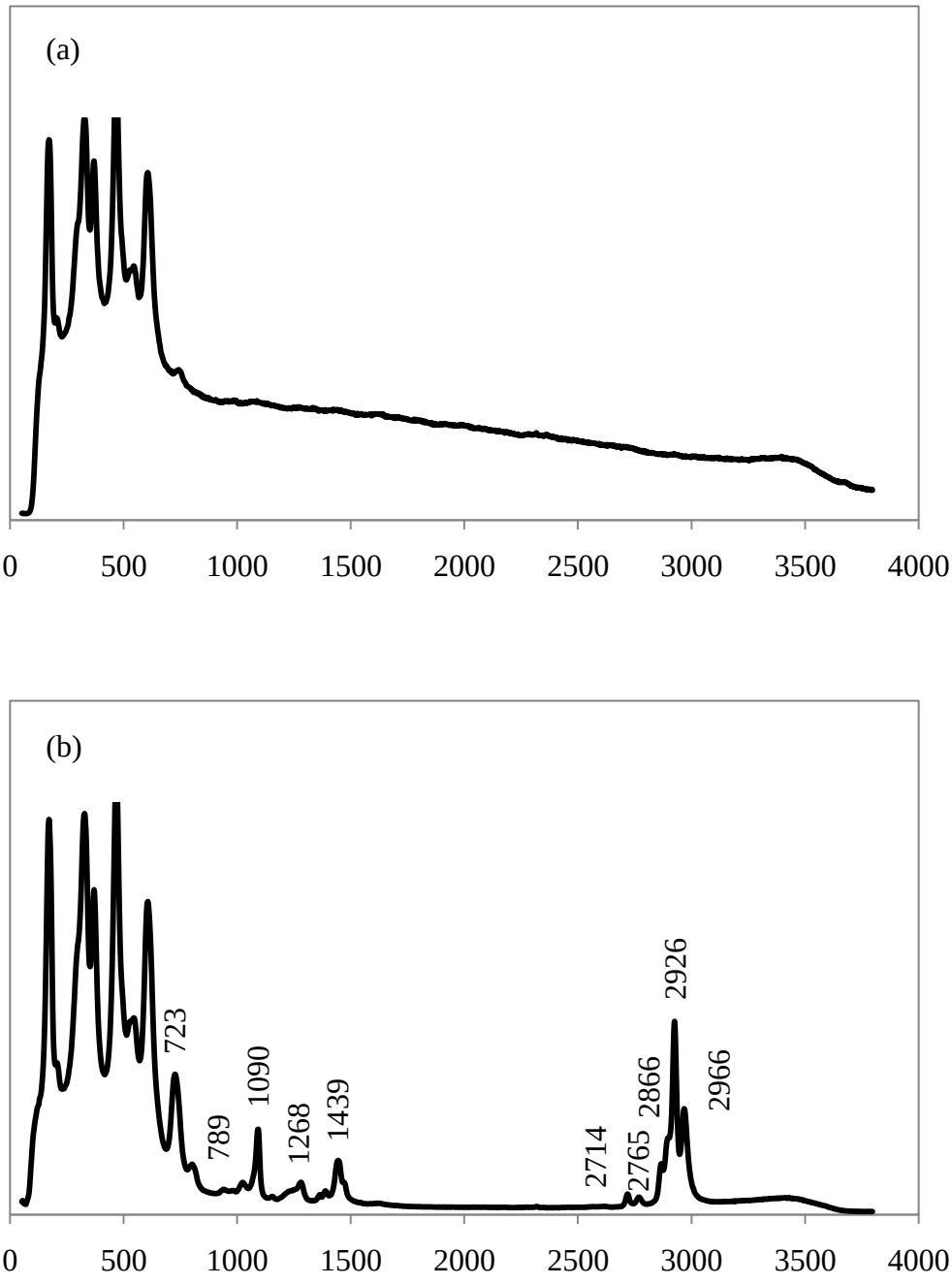

Figure 4.8. Raman Spectra of ZrO_2 (a) before and (b) after Exposure to TEP

Table 4.3. Peak Assignment for the Raman Spectra of Silica, Alumina, and Zirconia Samples subsequent to DMHP Exposure

DMHP		**SiO_2**	**Al_2O_3**	**ZrO_2**
peak	***assignment***	***peak***	***peak***	***peak***
746	P-O-C			749
979	P(V)	973		
1033	P-H			989
1062	C-O			1075
1166	C-H			1178
1249	P=O			1240
1445	C-H			1454
2422	P-H			2438
2844	OC-H		2851	2844
2919	C-H	2921	2926	
2946	C-H	2941	2953	2948
2990	C-H			3010

Table 4.4. Peak Assignment for the Raman Spectra of Silica, Alumina, and Zirconia Samples subsequent to DMMP Exposure

DMMP		**SiO_2**	**Al_2O_3**	**ZrO_2**
peak	***assignment***	***peak***	***peak***	***peak***
700	P-C			707
779	P-O-C			782
808	O-P-O			821
883	P-O-C			889
	P(V)	970		
1043	C-O			1056
1169	C-H			1175
1231	P=O			1222
	C-H			1314
1412	C-H			1409
1460	C-H			1448
2844	OC-H	2849	2851	2844
2916	C-H	2924	2926	2916
2946	C-H	2953	2956	2948
2983	C-H	2990		2990

Table 4.5. Peak Assignment for the Raman Spectra of Silica, Alumina, and Zirconia Samples subsequent to DEEP Exposure

DEEP		SiO_2	Al_2O_3	ZrO_2
peak	***assignment***	***peak***	***peak***	***peak***
687	P-C			684
730	P-C			733
789	P-O-C			786
973	P(V)			973
1030	P-O-C			1027
1090	C-O			1087
1215	C-H			1212
1277	P=O			1274
1403	C-H	1406		1397
1448	C-H			1445
2714	OC-H			2714
2760	OC-H			2763
2879	OC-H	2849	2849	
2921	C-H	2926	2921	2921
2966	C-H	2953	2951	2966
	C-H	2998	2998	

Table 4.6. Peak Assignment for the Raman Spectra of Silica, Alumina, and Zirconia Samples subsequent to TEP Exposure

TEP		SiO_2	Al_2O_3	ZrO_2
peak	***assignment***	***peak***	***peak***	***peak***
726	P-O-C			723
1037	C-O			1090
1277	P=O			1268
1445	C-H			1439
2714	OC-H			2714
2765	OC-H			2765
2869	OC-H	2851	2849	2866
2926	C-H	2924	2924	2926
2973	C-H	2951	2956	2966

Based on the peak assignment listed in Tables 4.3-4.6, it was notable that the peaks associated with the P-O-C and the P=O bonds were present in the spectra.

This suggested that dissociation of the OPs did not occur on the monoclinic zirconia samples, which could be indicative of a weaker interaction. The peaks associated with the P-O-C bond and the P=O bonds are further examined to determine the potential mechanisms of interaction (i.e. bonding with phosphonyl O atom, O of P=O, and/or bonding with the alkoxy O atom, O of P-OR) with the zirconia nanoparticles. Shifts in the frequencies of the peaks corresponding to the P-O-C, O-P-O, OC-H, and the P=O bonds are indicative of interaction.

For DMHP, DMMP, and DEEP, 3 cm^{-1} shifts (greater than the detector resolution of 1 cm^{-1}) were observed for the peaks associated with the P-O-C bond and 3 to 9 cm^{-1} shifts were observed for the peaks associated with the P=O bond. For DEEP, a 3 cm^{-1} shift was also observed for the OC-H bond. These results were indicative of interactions with the OPs through both the phosphonyl O atom (O of P=O) and the alkoxy O atom (O of P-OR). For TEP, shifts of 3, 2, and 2 cm^{-1} were observed, respectively, for three peaks associated with OC-H bonds, hence suggesting that the alkoxy O atom was involved in the interaction with the zirconia sample. Conclusions cannot be drawn for interaction through the P=O bond for TEP with the lack of a reference frequency (the peak for P=O bond of TEP was obscured in TEP's Raman spectrum, see Appendix).

In summary, the interactions of DMHP, DMMP, DEEP, and TEP occurred through non-dissociative interactions with the monoclinic zirconia samples synthesized in this work. Therefore, a static volumetric pressure based isotherm apparatus could be utilized for isotherm measurements. However, note that DEEP was previously identified, in Chapter 2, as a challenging (i.e. exceptionally

low vapor pressure) compound to measure adsorption isotherm data for with the apparatus used in this work. Hence, only the three OPs, DMHP, DMMP, and TEP were evaluated for their heat of adsorption. Based on the Raman spectroscopy results, varying magnitudes for the experimental heats of adsorption could be expected from these measurements due to the two different interaction mechanisms (i.e. interactions with O of P=O and O of P-OR).

Heat of Adsorption for OP uptake onto m-ZrO_2 particles

As previously discussed in Chapter 2, the temperature dependence of the adsorption isotherm provides a measure of the heat of adsorption. Thus, adsorption isotherm data were first collected. Monoclinic zirconia samples were exposed to single-component gas samples of DMHP, DMMP, and TEP at 23.8, 28.0, 30.6, and 34.6 °C. Adsorption measurements were made for gas sample pressures, P, between 0 Torr and the average vapor pressure of the OPs, P^o (i.e. between relative pressure, x =P/ P^o, from 0 to 1). Adsorption of the OP onto monoclinic zirconia, N, was correlated from the pressure measurement using the ideal gas law. The experimental results for DMHP, DMMP, TEP, and comparisons of the experimental results to four adsorption isotherm models (i.e. Langmuir (L), Freundlich (F), Generalized Langmuir (GL), and Langmuir-Freundlich (LF)) are illustrated in Figures 4.9 - 4.11. The errors in Figures 4.9 – 4.11 represent both the systematic errors associated with the resolution of the instrument and the imprecision of the measurements (±1σ). Note that some of the error bars are smaller than the symbols in the Figures 4.9 – 4.11; however, errors were characterized for all collected data.

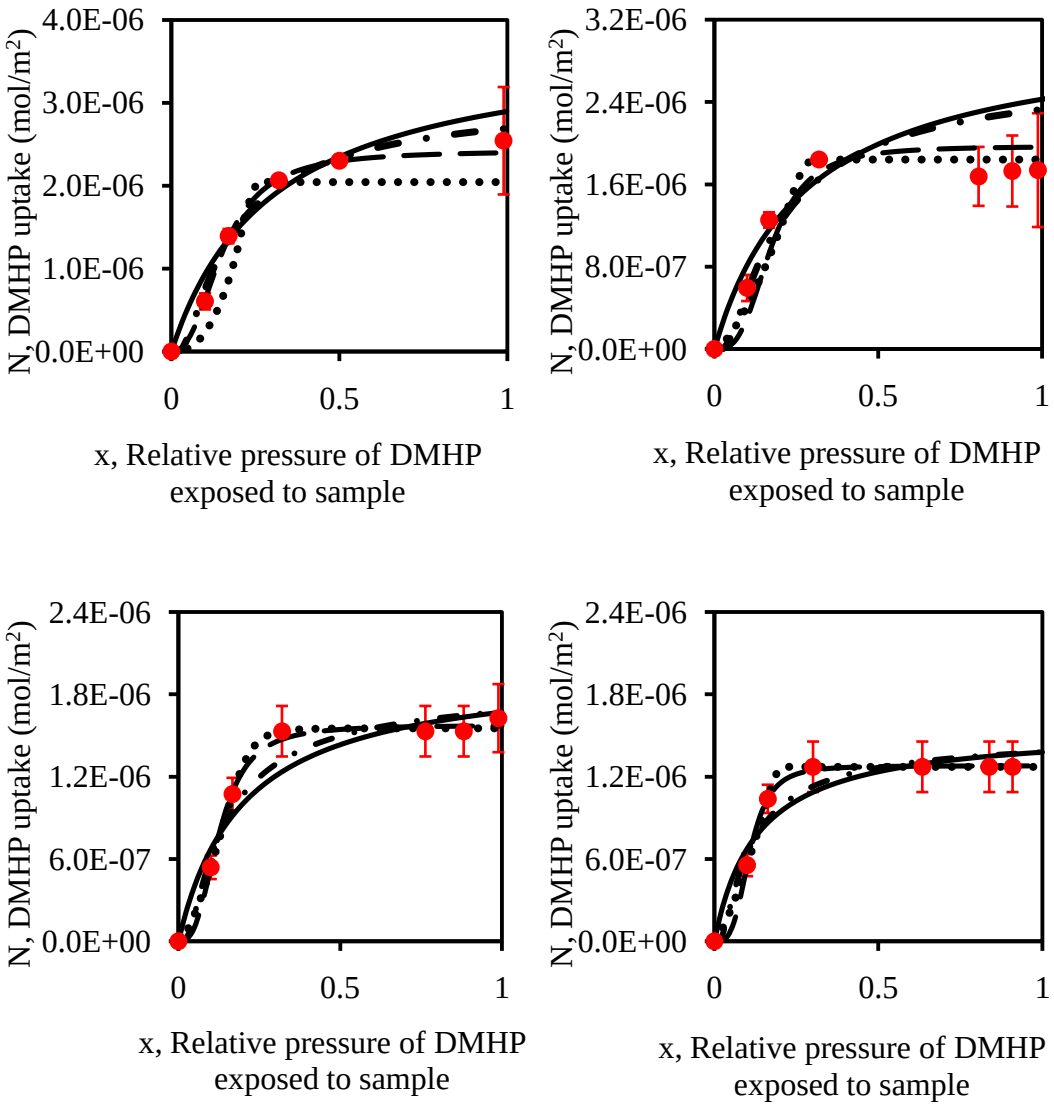

Figure 4.9. Adsorption of DMHP (●) by m-ZrO_2 at 23.8°C (top left), 28.0°C (top right), 30.6°C (bottom left), and 34.6°C (bottom right) as compared with the L (——), the F (– . –), the GL (····), and the LF (— —) Models

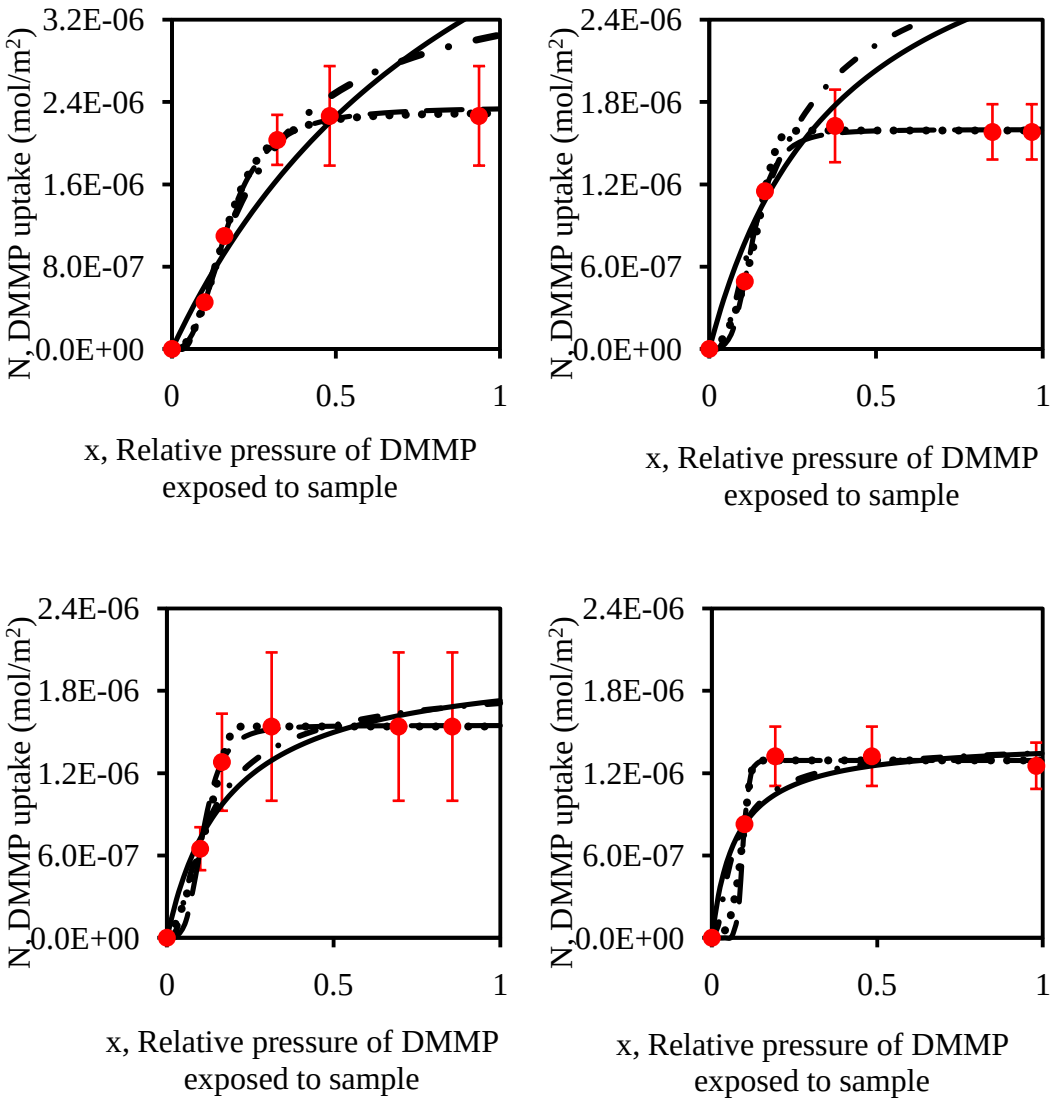

Figure 4.10. Adsorption of DMMP (●) by m-ZrO_2 at 23.8°C (top left), 28.0°C (top right), 30.6°C (bottom left), and 34.6°C (bottom right) as compared with the L (——), the F (– . –), the GL (····), and the LF (— —) Models

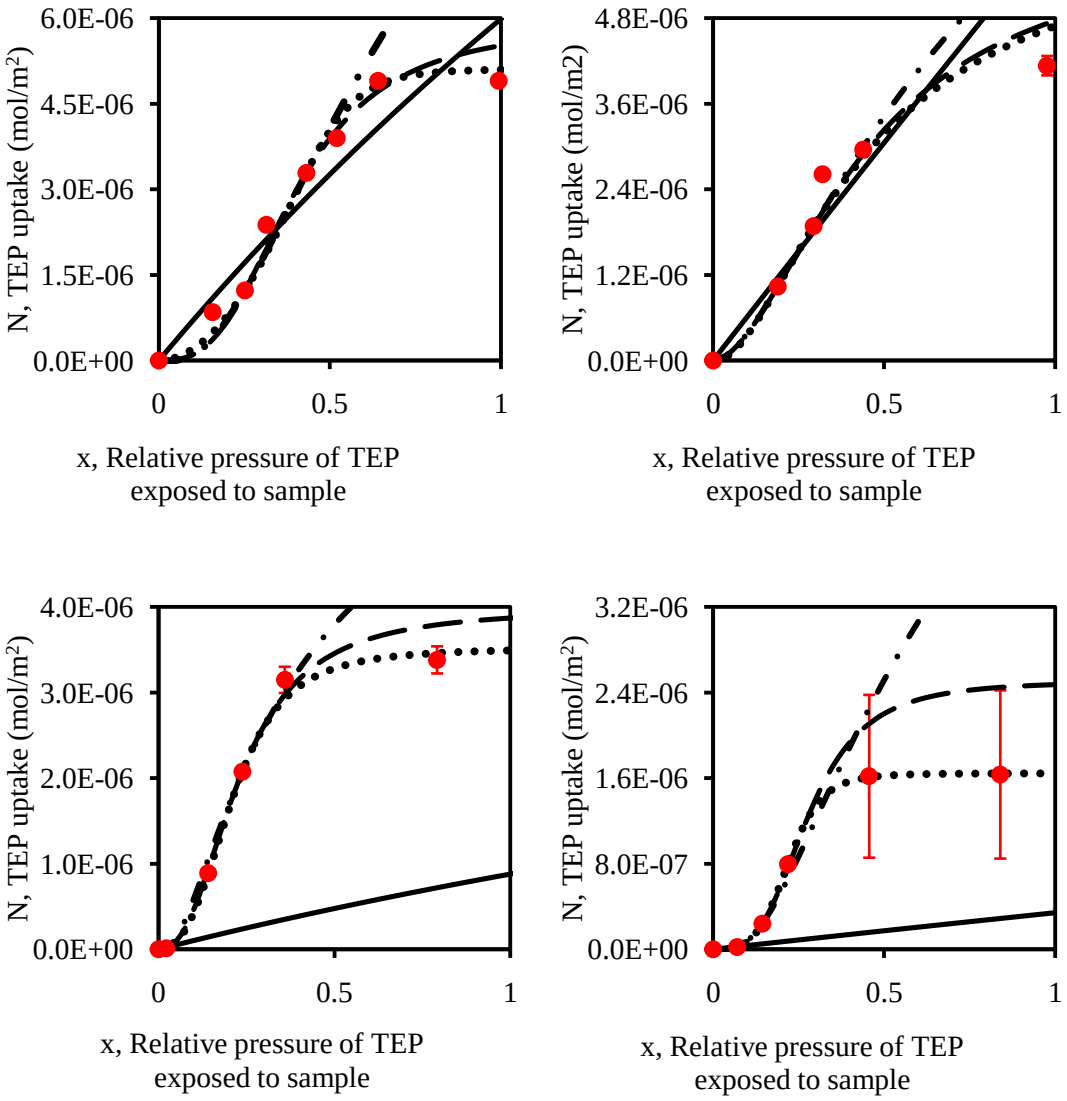

Figure 4.11. Adsorption of TEP (●) by m-ZrO_2 at 23.8°C (top left), 28.0°C (top right), 30.6°C (bottom left), and 34.6°C (bottom right) as compared with the L (——), the F (– . –), the GL (····), and the LF (— —) Models

TEP, DMMP, and DMHP adsorption onto monoclinic zirconia demonstrated monolayer adsorption behavior (i.e. adsorption, N, approaches saturation as relative pressure, *x*, approaches unity[124,125]). The monolayer adsorption behavior

could be attributed to the presence of pores in the sample. First, the limited volume in the pores could limit multiple layers of adsorbents from interacting with the pore surface. Additionally, one can also expect limited adsorption in the pores due to a diffusion limitation. Recall that the equilibrium point was defined as the point where the change in pressure, ΔP, per hour was less than the gauge resolution. Hence, the measurements taken could correspond to a meta-stable state of adsorption. Nevertheless, the measurements reflected an environmentally representative scenario where the interaction time between the adsorbates and the adsorbent can be expected to be less than one hour if natural convection mechanism (e.g. wind) was present. For the purpose of this discussion, achievement of equilibrium, though possibly meta-stable, was assumed.

To obtain a continuous representation of the experimental data for any value of the relative pressure, *x*, the results were compared with the isotherm models listed in Table 4.7.

Table 4.7. Monolayer Adsorption Isotherm Models

Isotherm model	**Model equation**[170,171,172]
Langmuir	$N = a_m * \frac{KP}{1+KP}$
Freundlich	$N = a_m * \left(\frac{KP}{1+KP}\right)^m$
Generalized Langmuir	$N = a_m * \left[\frac{(KP)^n}{1+(KP)^n}\right]^{\frac{m}{n}}$
Langmuir Freundlich	$N = a_m * \frac{(KP)^n}{1+(KP)^n}$

These isotherm models are representative of monolayer adsorption. In Table 4.7, the adsorbed amount, N, is related to the monolayer capacity, a_m, the adsorption

constant, *K*, the adsorption behavior as P approaches infinity, *n*, the adsorption behavior as P approaches zero, *m*, and the equilibrium sorbate pressure, *P*, in these monolayer adsorption isotherm models. The 2-parameter Langmuir (L) model assumes energetic homogeneity, whereas the 3-parameter Freundlich (F) model, the 3-parameter Langmuir-Freundlich (LF) model, and the 4-parameter Generalized Langmuir (GL) model account for varying distributions of energetic heterogeneity.

As illustrated in Figure 4.9 – 4.11, the 2-parameter Langmuir (L) model and the 3-parameter Freundlich (F) model failed to describe all of the experimental results; whereas the 3-parameter Langmuir Freundlich (LF) model and the 4-parameter Generalized Langmuir (GL) models were comparable in efficacy within the uncertainty of the measurements. Further discussions for DMHP, DMMP, and TEP utilize the Langmuir Freundlich (LF) model predictions since these model predictions provide continuous representations of the experimentally determined relationships between OP adsorption, N, and relative pressure of the OP, *x*, using a minimal number of parameters.

The temperature dependencies of adsorption, N, for DMHP, DMMP, and TEP, are represented by the Langmuir Freundlich predictions as shown in Figures 4.12 – 4.14, respectively.

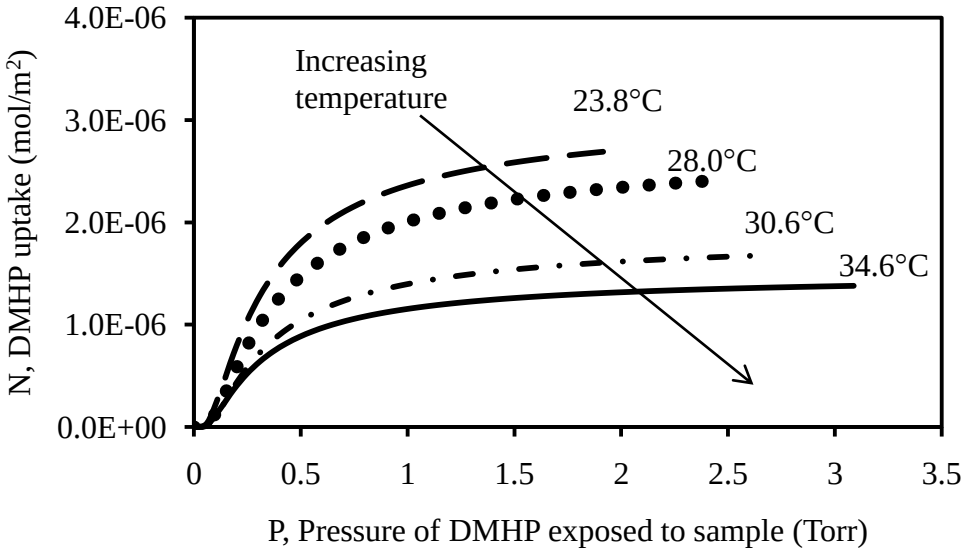

Figure 4.12. Temperature Dependency of DMHP Adsorption, N, as represented by Langmuir Freundlich Predictions for Adsorption by m-ZrO_2 at 23.8, 28.0, 30.6, and 34.6 °C

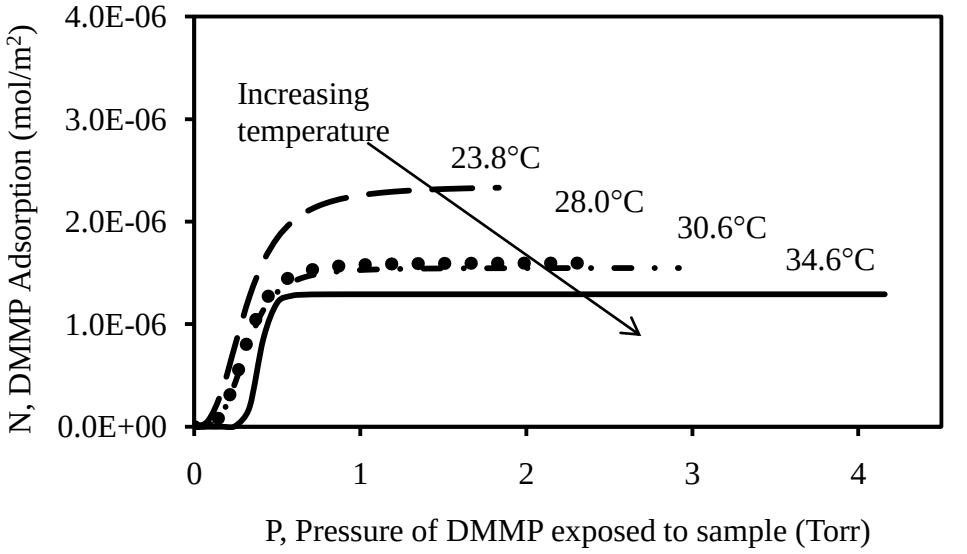

Figure 4.13. Temperature Dependency of DMMP Adsorption, N, as represented by Langmuir Freundlich Predictions for Adsorption by m-ZrO_2 at 23.8, 28.0, 30.6, and 34.6 °C

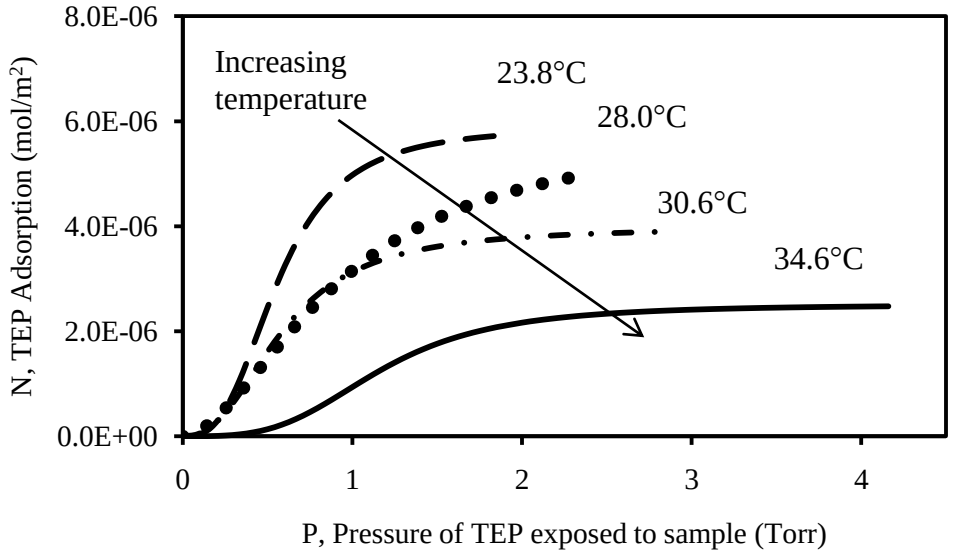

Figure 4.14. Temperature Dependency of TEP Adsorption, N, as represented by Langmuir Freundlich Predictions for Adsorption by m-ZrO_2 at 23.8, 28.0, 30.6, and 34.6 °C

The adsorptions of DMHP, DMMP, and TEP decreased with increasing temperature. These results were representative of exothermic processes such as adsorption (i.e. interactions were less favorable with increases in temperature[177,178]). Similar to a-SiO_2 adsorption of DMHP, DMMP, and TEP, adsorption onto m-ZrO_2 also illustrated variations in the magnitude of decrease in DMHP, DMMP, and TEP adsorption with increases in temperature. As previously discussed, these variations are evidence of surface heterogeneity[179].

As mentioned in Chapter 2, the isosteric heat of adsorption is defined by the Clausius-Clapeyron equation, and is based upon the temperature dependence of the adsorption isotherms. To determine the isosteric heats of adsorption, adsorption isosteres, or ln P versus T^{-1} plots, were constructed at a constant value

for N. A value of 5 x 10^{-7} moles of OPs adsorbed / m^2 was chosen for N to incorporate all of the adsorption isotherm data in the calculation. The ln P versus T^{-1} plots for DMHP, DMMP, and TEP adsorption onto m-ZrO_2 are illustrated in Figures 4.15 – 4.17, respectively.

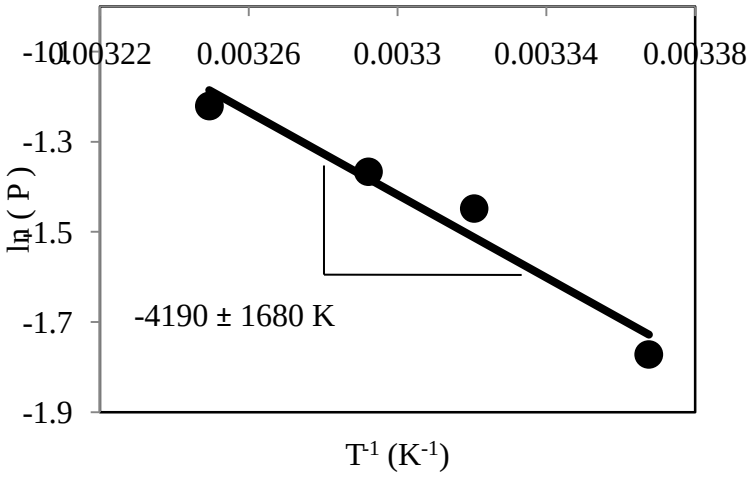

Figure 4.15. Ln P (from Langmuir Freundlich Prediction) versus T^{-1} Plot for DMHP Adsorption onto m-ZrO_2.

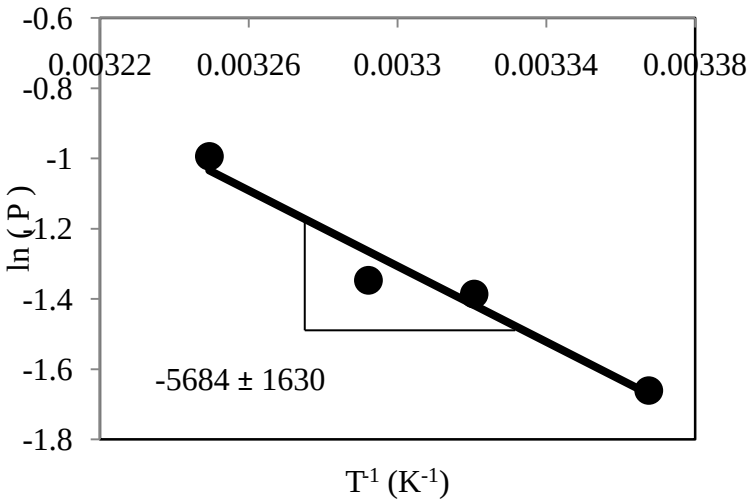

Figure 4.16. Ln P (from Langmuir Freundlich Prediction) versus T^{-1} Plot for DMMP Adsorption onto m-ZrO_2

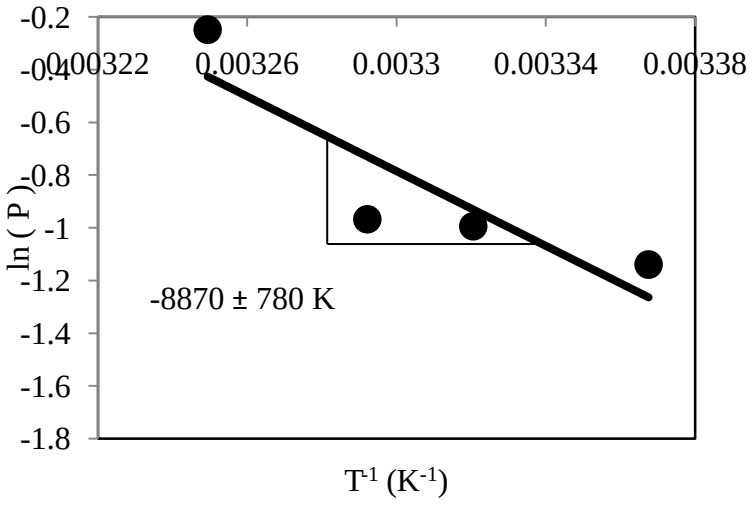

Figure 4.17. Ln P (from Langmuir Freundlich Prediction) versus T^{-1} Plot for TEP Adsorption onto m-ZrO_2

The isosteric heats of adsorption for TEP, DMMP, and DMHP as calculated from Figures 4.15 – 4.17 and the Clausius-Clapeyron equation are listed in Table 4.8.

Table 4.8. Isosteric Heat of Adsorption for m-ZrO_2 Adsorption of OPs at N = $5x10^{-7}$ mole of OPs adsorbed / m^2

OP compound	**Isosteric heat of adsorption ± 1σ (kcal/mol)**
DMHP	-7.96 ± 3.19
DMMP	-10.8 ± 3.10
TEP	-16.9 ± 1.48

Considering the adsorption onto m-ZrO_2, the isosteric heat of adsorption was more negative for TEP as compared to DMMP, and more negative for DMMP as

compared to DMHP. These data indicated that TEP has a stronger interaction with m-ZrO_2 as compared to either DMMP or DMHP.

For comparison, the a-SiO_2 isotherm data presented in Chapter 2 were normalized by its respective surface area and the isosteric heats of adsorption were recalculated at the same N value. For all three OP compounds, the isosteric heats of adsorption were more negative (stronger interaction) for m-ZrO_2 as compared with adsorption onto a-SiO_2 (ΔH_{ads} between -4.94 ± 0.47 to -5.99 ± 0.08 kcal/mol). This trend between m-ZrO_2 and a-SiO_2 was in agreement with the computational predictions presented in Chapter 3.

It is notable that although the trend is in agreement with the computational predictions, the magnitude of the heat of adsorption for m-ZrO_2 adsorption of the OPs differed from the results of the DFT study. This difference was also observed for a-SiO_2, and as mentioned in Chapter 2, and it was a result of energetic heterogeneity. In the case of m-ZrO_2, interactions between the OPs and any surface bound water (e.g. associated in the form of H_2O or dissociated in the form of -OH) and other less favorable interactions (i.e. interaction via methoxy O or interaction with other active sites) could serve as sources of discrepancies. Energetic heterogeneity from the presence of water will be subsequently discussed. Nevertheless, monoclinic zirconia nanoparticles were shown to be able to adsorb OPs in this first experimental evaluation of the material.

TGA / RGA analysis of m-ZrO_2 for DMMP Adsorption from an Air Mixture

The monoclinic zirconia nanoparticles synthesized in this work were exposed to a gaseous mixture of OP and air to determine the performance of the zirconia material when utilized for the desired application (i.e. OP pollution control). DMMP was utilized as the representative OP molecule for this evaluation. The mixture contained ~45 ppm of DMMP and atmospheric constituents from the air (i.e. the mixture was not generated from high purity air). The ability for zirconia to adsorb gas-phase DMMP from a flowing stream of air was probed by thermal gravimetric analysis (TGA) and residual gas analysis (RGA).

A zirconia sample exposed to the air / DMMP mixture and a zirconia sample exposed only to the air were heated to 700°C at the same heating rate and portions of both samples analyzed by TGA. Based on the TGA results, mass loss could be observed even at room temperature. When heated to 700°C, a 2.4% mass loss was observed from the zirconia sample exposed only to air and a 2.2% mass loss was observed from the zirconia sample exposed to the air / DMMP mixture. For the sample mass analyzed (i.e. ~100 mg), a 2.8% difference in mass loss, or ~ 2800 μg in mass loss, could be expected if all of the DMMP was adsorbed from the air / DMMP mixture and desorbed upon heating during TGA. The difference in mass loss between the two samples was much less than 2.8%, thereby suggesting that negligible DMMP was present. To further probe for the presence of DMMP, another portion of the sample was also analyzed by RGA and the mass spectra of the zirconia sample which was exposed to the air / DMMP mixture are shown in Figure 4.18.

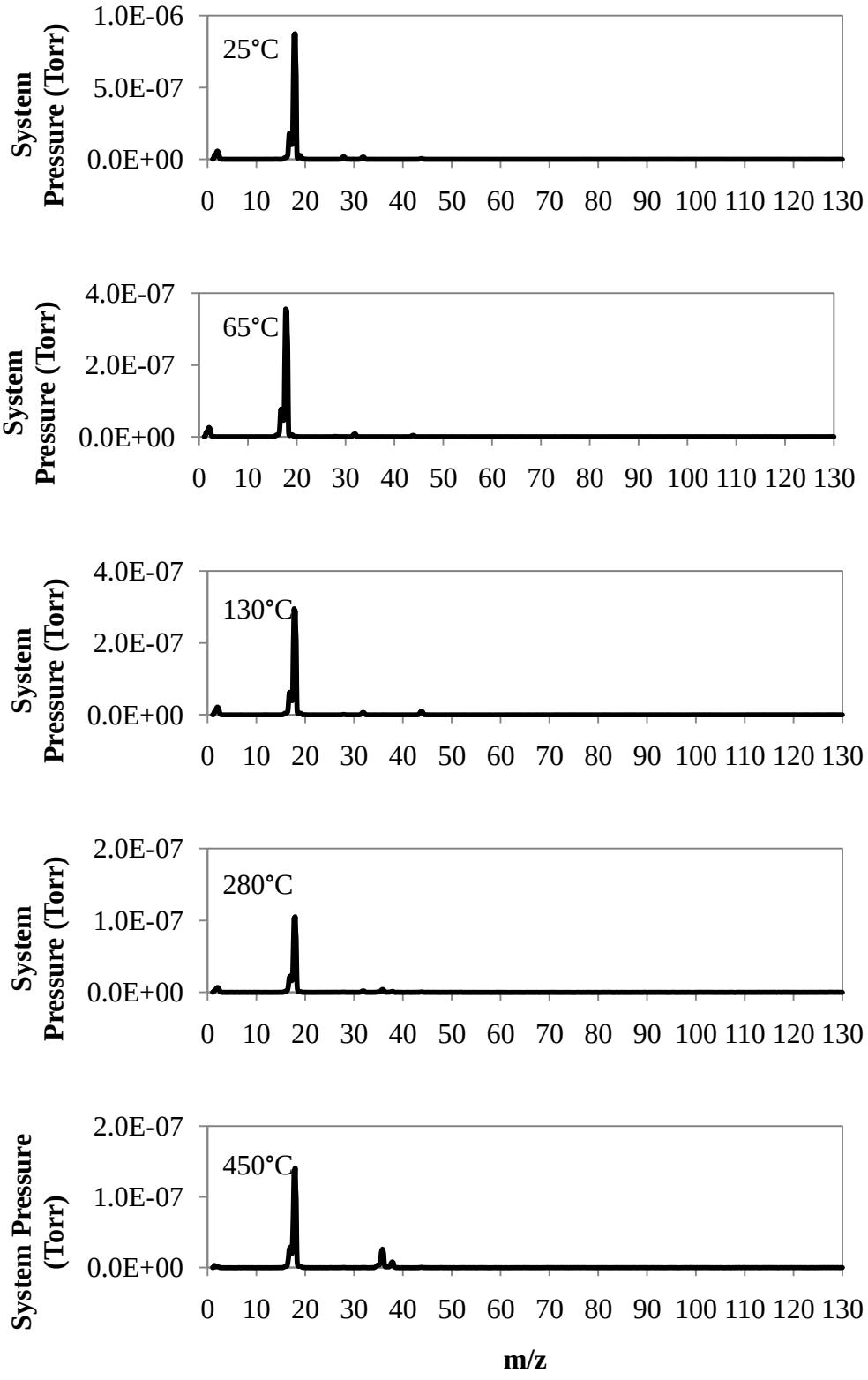

Figure 4.18. Residual Gas Analysis of m-ZrO_2 exposed to DMMP (ppm range) and Air Mixture

The spectra were compared with a mass spectrum of DMMP shown in Figure 4.19 and a spectrum of the background in Figure 4.20.

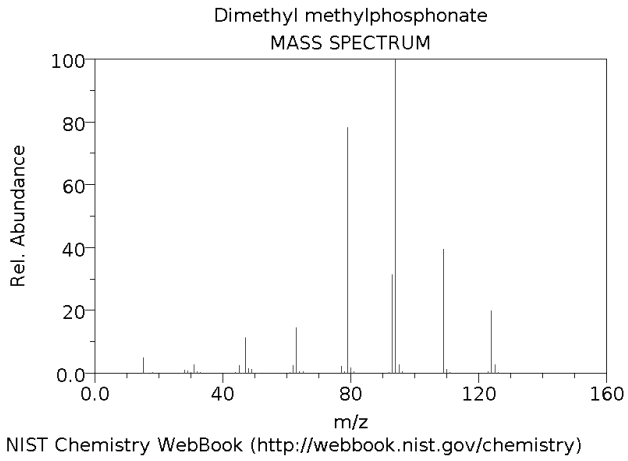

Figure 4.19. Reference Spectrum of DMMP (normalized)

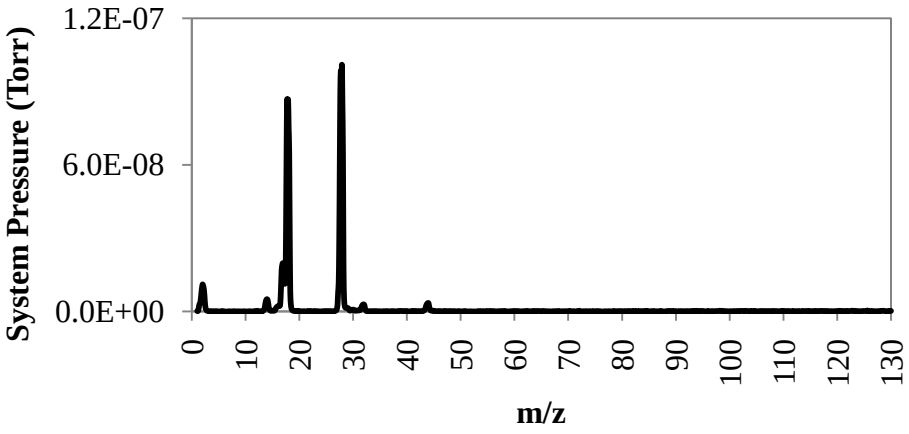

Figure 4.20. Background Spectrum of Residual Gas Analyzer Signal

It is notable that in comparing the spectra obtained from heating m-ZrO_2 to various temperatures, shown in Figure 4.18, and the background spectrum in Figure 4.20, a higher system pressure resulted from a mass / charge peak corresponding to water. Additionally, it is important to note that based on the

mass spectra shown in Figure 4.18, water was the only detectable species that desorbed from the zirconia nanoparticles. This suggested that water could potentially be interfering with the adsorption of DMMP or similar OPs.

To verify that the technique utilized could indeed detect DMMP when a sufficient amount of the OP was present, a sample of the m-ZrO_2, preheated in the same manner as the samples utilized for the adsorption isotherm measurement, was exposed to a dose of the pure gaseous DMMP. RGA was utilized to evaluate the sample and the mass spectra obtained are shown in Figure 4.21. In comparing the spectra shown in Figure 4.21 with the background spectrum in Figure 4.20 and the reference spectrum of DMMP in Figure 4.19, it can be observed that mass / charge peaks associated with the desorption of DMMP and water were present. This indicated that the m-ZrO_2 nanoparticles which were preheated at 105°C for 45 minutes prior to exposure still contained surface bound water. As previously mentioned, the magnitude of the experimental heats of adsorption differed from the computational predictions presented in Chapter 3. The desorption of water as observed from the RGA result indicated that the mismatch might be attributed to the energetic heterogeneity resulting from the interaction of the OP with surface bound water (versus interaction of the OP with the zirconia surface). The presence of surface bound water could additionally contribute to the saturation behavior observed from the adsorption isotherm measurements (i.e. limited amount of active sites available for DMMP or limited amount of DMMP interacting with surface bound water).

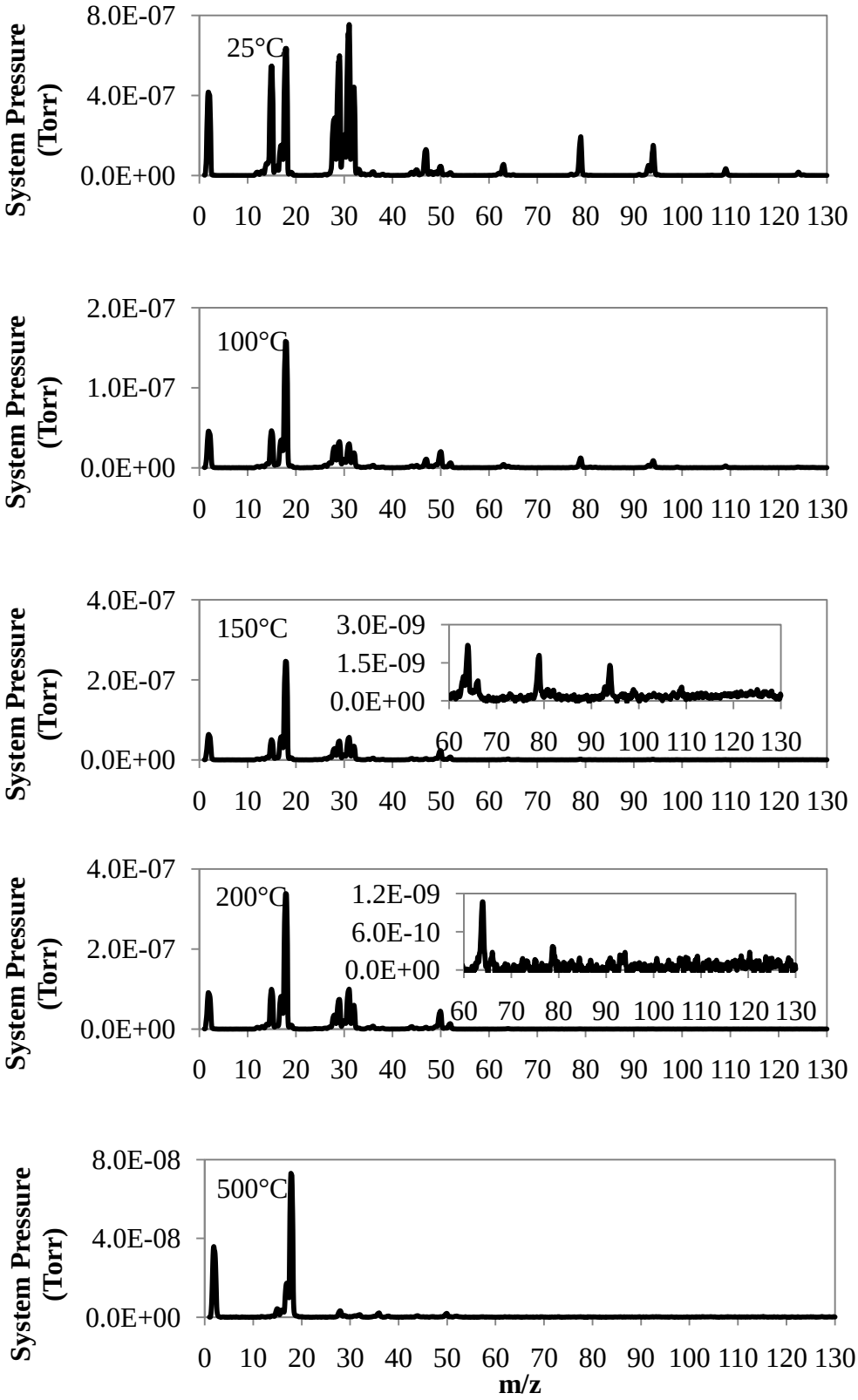

Figure 4.21. Residual Gas Analysis of m-ZrO_2 exposed to Single-Component Gaseous DMMP

Further observation indicated that the desorption of DMMP and water begin at room temperature and the last traces of all detectable (beyond the sensitivity of the instrument, i.e. 10^{-10} Torr) and ionized fragments associated with DMMP were observed at 150°C. The low temperature of desorption for DMMP indicated a weak binding interaction, which provided the reasoning for the lower magnitudes observed for the experimental heats of adsorption as compared with the computationally predicted heats of adsorption obtained from the most favorable and ideal one molecule – one site interaction.

For a final comparison, silica and alumina samples exposed to the air / DMMP mixture and to air only were probed by TGA to determine if significant mass losses could be observed from these samples. Based on the TGA results, negligible differences between the mass losses from the samples which were exposed to DMMP as compared with the samples which were not exposed to DMMP were observed for silica and alumina, similar to results obtained with zirconia. These results were indicative of the absence of DMMP adsorption at low concentration and when other atmospheric constituents were present. Since negligible changes in mass were recorded, RGA was not performed on silica and alumina.

In summary, all three oxides which were probed by TGA indicated that water interfered with the adsorption of low concentrations of DMMP in a flow system. RGA results obtained from zirconia further indicated that water interference continued to be an issue (i.e. adsorption of DMMP observed but water reduced the strength of the interactions) even when pure DMMP was utilized and when

the surface was subjected to preheating. Thus, to effectively apply the material for the application of OP pollution control, water must be eliminated.

4.4 Conclusion

The design and application of monoclinic zirconia (same phase the model investigated in Chapter 3) for the adsorption of the OPs, DMHP, DMMP, DEEP, and TEP were investigated. Monoclinic zirconia nanoparticles were synthesized using hydrothermal methods in the presence of urea, and calcined at various conditions in a first attempt in optimizing the synthesis conditions. Nanoparticles of ~37 nm in size and with a BET surface area of 115.62 ± 0.36 m^2/g were obtained from the calcination condition that was ultimately used (i.e. 400°C for 4h in flowing O_2).

Qualitative adsorption studies were performed by Raman spectroscopy and the results indicated the non-dissociative adsorption of DMHP, DMMP, DEEP, and TEP. Furthermore, Raman results also indicated that adsorption occurred via both the methoxy O atom and the phosphoryl O atom. Quantitative measurements of the amounts of OPs adsorbed were also made for the interaction of DMHP, DMMP, and TEP with the m-ZrO_2 synthesized in this work. Heats of adsorption were determined from the quantitative measurements, and the experimental results ranged from –7.96 to –16.9 kcal/mol, with the strongest interaction corresponding to TEP and the weakest interaction corresponding to DMHP. This trend was similar to that observed for a-SiO_2 as presented in Chapter 2 and was as expected based on the vapor pressures of the OPs. The magnitudes of the heats of

adsorption obtained experimentally differed from the values predicted from the DFT study in Chapter 3. As explained in Chapter 2, this can be attributed to energetic heterogeneity.

The presence of energetic heterogeneity was apparent when zirconia was probed by thermal gravimetric analysis (TGA) and residual gas analysis (RGA). In the analysis of the m-ZrO_2 synthesized in this work which was preheated and exposed to pure gaseous DMMP, the simultaneous desorption of DMMP and water were observed, even at room temperature. This result indicated that surface bound water remained on the nanoparticles despite preheating. DMMP interaction with the surface bound water as opposed to interaction with the zirconia surface active sites led to the lower magnitudes for the experimentally determined heats of adsorption as compared with the computational predictions. The presence of water was additionally problematic when the zirconia samples were utilized to adsorb low concentrations of DMMP in air through the use of a flow system. Surface-bound DMMP was not detectable when low concentrations of DMMP were employed. This issue was observed for silica, alumina, and zirconia. Based on these results, interference from water should be addressed in order to extend the utility of the oxide of interest as an OP pollution control technology to low OP concentrations. Nevertheless, this first experimental investigation demonstrated that monoclinic zirconia nanoparticles have the ability to adsorb the OPs.

CHATPER 5

FUTURE WORK AND CONSIDERATIONS IN APPLICATION

In Chapter 4, monoclinic zirconia nanoparticles were synthesized hydrothermally in the presence of urea (concentration of 4M) and a first attempt at optimization was presented. The interactions between the material and the OPs of interest were characterized. The nanoparticles demonstrated an ability to adsorb the OPs, however, the presence of water was found to be problematic. Failure to eliminate surface bound water resulted in weaker interactions between the monoclinic zirconia nanoparticles and the OPs as compared to the heat of interaction predicted from the computational chemistry calculations discussed in Chapter 3. Thus, future work would focus on the synthesis of an improved material that would allow zirconia to interact with the OPs by a more ideal interaction mechanism (e.g. solely through selective bond formation with the phosphonyl O atom of the P=O group of the OPs). The primary goal of the future work is to eliminate interferences from water. Different strategies are proposed to address the presence of water.

5.1 Pre-filtering of Water from Zirconia

A highly hydrophilic material, such as other oxides or commercially available desiccants, can be utilized in a sequential fashion in conjunction with zirconia. The effectiveness of pre-filtering can be examined by placing the highly hydrophilic material and zirconia in a packed bed arrangement and exposing the two materials to an air / OP mixture in a flow system. The zirconia material could be retrieved subsequent to exposure and a TGA / RGA analysis can be performed

and compared with results obtained from zirconia only. The drawback to this strategy is that water that is inherently present on zirconia will remain on the surface unless the material was pretreated at elevated temperature until all of the water molecules are desorbed. Nevertheless, some improvements can be expected from pre-filtering.

5.2 Synthesis of Zirconia Nanoparticles in a Water-Sensitive Matrix

A strategy to address the presence of surface bound water that was found on the zirconia surface is to synthesize the particles in the pores of a water-sensitive matrix. A water-sensitive matrix could be hydrophilic and preferentially adsorb water onto its surface or hydrophobic and repel water from the material. For example, small nanoparticles of zirconia can be synthesized from zirconium precursors in the pores of a porous oxide to eliminate exposure to water upon their formation. On the contrary, zirconia nanoparticles could also be synthesized in situ in a hydrophobic matrix such as porous carbon. The concept is illustrated in Figure 5.1.

Concerning the synthesis of the proposed material, the in situ formation of oxide nanoparticles in a porous oxide have been reported in the literature[218]. In particular, Mn_3O_4 nanoparticles were reportedly anchored to mesoporous silica by thermolysis of a magnetic manganese precursor linked to a SBA-15 mesoporous silica modified with –COOH functional groups. The in situ formation of RuO_2 by a spontaneous reduction of ruthenium tetraoxide in the presence of organics into the pores of a commercially available $LiMn_2O_4$ has also been reported[219]. Similar

techniques could be applied to the simultaneous formation and encapsulation of zirconia nanoparticles. Other reactions that do not involve the introduction of water into the pores (i.e. reaction based on hydrolysis or reaction leading to the release of water during formation) could also be employed.

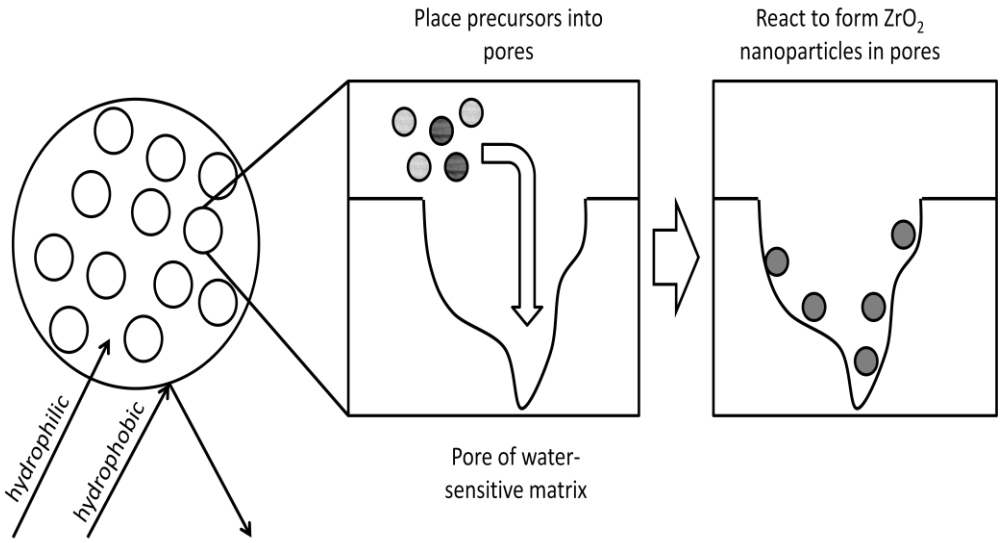

Figure 5.1. Synthesis of Zirconia Nanoparticles in Water-Sensitive Matrix

Extensive characterization would be required to determine the interaction of the water-sensitive matrix with OPs and water, as well as to determine the quality of the nanoparticles which would result from an in situ synthesis technique.

5.3 Design of Material with Alternate Active Sites

Zirconia modified with functional groups or additional active sites could alternately be investigated. Using computational chemistry tools, which were shown to be effective for the purpose of providing trends, the zirconia model constructed in Chapter 3 could be modified with alternate active sites. The modification of the zirconia surface with alternate functional groups as well as

modification of the zirconia surface with two different types of active sites are of interest. By modifying zirconia with alternate functional groups, one might be able to design a material that forms a stronger interaction with the OPs. Alternately, by introducing two different types of active sites, one could obtain information about the selectivity of the sites toward water and OPs. Two examples are illustrated in Figure 5.2 where an –OH functional could be compared with a $–CH_3$ group or a –COOH group to determine if the alternate sites preferentially adsorb water. Hydrophilicity decreases from –COOH to –OH to $–CH_3$. Thus, H_2O could potentially prefer an interaction with a more hydrophilic site and allow the OPs to interact with the less hydrophilic sites.

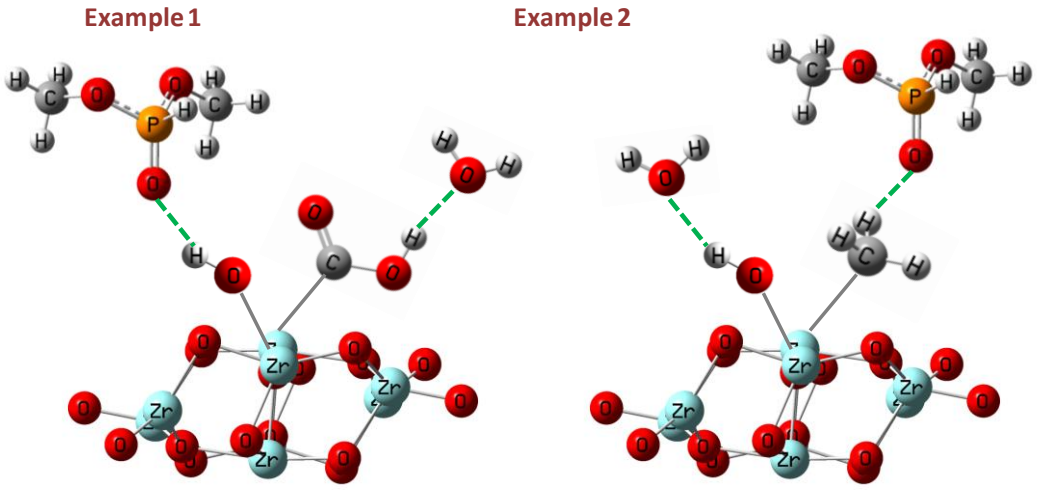

Figure 5.2. Design of a Material with Alternate Active Sites

5.4 Considerations in Application

In conclusion, considering the application of the amorphous silica (a-SiO_2) and the monoclinic zirconia (m-ZrO_2) which were investigated in this work, a-SiO_2 offers a cost benefit in a practical setting whereas m-ZrO_2 offers a thermodynamic advantage (i.e. superior interaction strengths), as determined from the empirical heats of adsorption presented in Chapter 4. Specifically, in comparing the cost of the material on a mass basis, silica is currently commercially available at $0.05 per gram as compared to the ~ $100 required to produce a gram of pure m-zirconia in this small scale laboratory synthesis. Commercial zirconia is currently available, but it offers low surface area and contains impurities. When accounting for their respective adsorption capacity (i.e. 10^7 moles per m^2 of silica and 10^6 moles per m^2 of zirconia) and the difference in their surface areas (i.e. 284 m^2 per gram of silica and 116 m^2 per gram of zirconia) the large difference in cost could not be compensated. Hence, when making a comparison between the commercially available silica material utilized in this work and the monoclinic zirconia material synthesized in this work, silica is superior for practical applications. Nevertheless, strategies for improvement to the synthesis of zirconia are available and are recommended to capitalize on its thermodynamic advantage.

REFERENCES

1. Bermudez, V. M., Computational study of the adsorption of trichlorophosphate, dimethyl methylphosphonate, and sarin on amorphous SiO2. *Journal of Physical Chemistry C* **2007,** *111* (26), 9314-9323.

2. Butrow, A. B.; Buchanan, J. H.; Tevault, D. E., Vapor Pressure of Organophosphorus Nerve Agent Simulant Compounds. *Journal of Chemical and Engineering Data* **2009,** *54* (6), 1876-1883.

3. Tevault, D. E.; Buchanan, J. H.; Buettner, L. C., Ambient volatility of DMMP. *International Journal of Thermophysics* **2006,** *27* (2), 486-493.

4. Bartelt-Hunt, S. L.; Knappe, D. R. U.; Barlaz, M. A., A review of chemical warfare agent simulants for the study of environmental behavior. *Critical Reviews in Environmental Science and Technology* **2008,** *38* (2), 112-136.

5. Snow, E. S.; Perkins, F. K.; Houser, E. J.; Badescu, S. C.; Reinecke, T. L., Chemical detection with a single-walled carbon nanotube capacitor. *Science* **2005,** *307* (5717), 1942-1945.

6. Tzou, T. Z.; Weller, S. W., CATALYTIC-OXIDATION OF DIMETHYL METHYLPHOSPHONATE. *Journal of Catalysis* **1994,** *146* (2), 370-374.

7. Christensen, A.; Carter, E. A., First-principles study of the surfaces of zirconia. *Physical Review B* **1998,** *58* (12), 8050-8064.

8. Kumari, L.; Li, W. Z.; Xu, J. M.; Leblanc, R. M.; Wang, D. Z.; Li, Y.; Guo, H. Z.; Zhang, J. D., Controlled Hydrothermal Synthesis of Zirconium Oxide Nanostructures and Their Optical Properties. *Crystal Growth & Design* **2009,** *9* (9), 3874-3880.

9. Feigenbrugel, V.; Le Person, A.; Le Calve, S.; Mellouki, A.; Munoz, A.; Wirtz, K., Atmospheric fate of dichlorvos: Photolysis and OH-initiated oxidation studies. *Environmental Science & Technology* **2006,** *40* (3), 850-857.

10. Aschmann, S. M.; Tuazon, E. C.; Atkinson, R., Atmospheric chemistry of diethyl methylphosphonate, diethyl ethylphosphonate, and triethyl phosphate. *Journal of Physical Chemistry A* **2005,** *109* (10), 2282-2291.

11. Kiely, T.; Donaldson, D.; Grube, A. *Pesticides Industry Sales and Usage: 2000 and 2001 Market Estimates*; Biological and Economic Analysis Division Office of Pesticide Programs Office of Prevention, Pesticides, and Toxic Substances U.S. Environmental Protection Agency: 2004.

12. Manthripragada, A. D.; Costello, S.; Cockburn, M. G.; Bronstein, J. M.; Ritz, B., Paraoxonase 1, Agricultural Organophosphate Exposure, and Parkinson Disease. *Epidemiology* **2010,** *21* (1), 87-94.

13. Harnly, M.; McLaughlin, R.; Bradman, A.; Anderson, M.; Gunier, R., Correlating agricultural use of organophosphates with outdoor air concentrations: A particular concern for children. *Environmental Health Perspectives* **2005,** *113* (9), 1184-1189.

14. Fukuto, T. R., MECHANISM OF ACTION OF ORGANOPHOSPHORUS AND CARBAMATE INSECTICIDES. *Environmental Health Perspectives* **1990,** *87*, 245-254.

15. Roldan-Tapia, L.; Parron, T.; Sanchez-Santed, F., Neuropsychological effects of long-term exposure to organophosphate pesticides. *Neurotoxicology and Teratology* **2005,** *27* (2), 259-266.

16. Reemtsma, T.; Quintana, J. B.; Rodil, R.; Garcia-Lopez, M.; Rodriguez, I., Organophosphorus flame retardants and plasticizers in water and air I. Occurrence and fate. *Trac-Trends in Analytical Chemistry* **2008,** *27* (9), 727-737.

17. Segal-Rosenheimer, M.; Dubowski, Y., Photolysis of methyl-parathion thin films: Products, kinetics and quantum yields under different atmospheric conditions. *Journal of Photochemistry and Photobiology a-Chemistry* **2010,** *209* (2-3), 193-202.

18. Aschmann, S. M.; Long, W. D.; Atkinson, R., Temperature-dependent rate constants for the gas-phase reactions of OH radicals with 1,3,5-trimethylbenzene, triethyl phosphate, and a series of alkylphosphonates. *Journal of Physical Chemistry A* **2006,** *110* (23), 7393-7400.

19. Seinfeld, J. H.; Pandis, S. N., *Atmospheric chemistry and physics : from air pollution to climate change*. 2nd ed.; Wiley: Hoboken, N.J., 2006; p xxviii, 1203 p.

20. van Dijk, H. F. G.; Guicherit, R., Atmospheric dispersion of current-use pesticides: A review of the evidence from monitoring studies. *Water Air and Soil Pollution* **1999,** *115* (1-4), 21-70.

21. Aschmann, S. M.; Tuazon, E. C.; Atkinson, R., Atmospheric chemistry of dimethyl phosphonate, dimethyl methylphosponate, and dimethyl ethylphosphonate. *Journal of Physical Chemistry A* **2005,** *109* (51), 11828-11836.

22. Bermudez, V. M., Adsorption on carbon nanotubes studied using polarization-modulated infrared reflection-absorption spectroscopy. *Journal of Physical Chemistry B* **2005,** *109* (20), 9970-9979.

23. Saxena, A.; Singh, B.; Sharma, A.; Dubey, V.; Semwal, R. P.; Suryanarayana, M. V. S.; Rao, V. K.; Sekhar, K., Adsorption of dimethyl methylphosphonate on metal impregnated carbons under static conditions. *Journal of Hazardous Materials* **2006,** *134* (1-3), 104-111.

24. Sheinker, V. N.; Mitchell, M. B., Quantitative study of the decomposition of dimethyl methylphosphonate (DMMP) on metal oxides at room temperature and above. *Chemistry of Materials* **2002,** *14* (3), 1257-1268.

25. Ferguson-McPherson, M. K.; Low, E. R.; Esker, A. R.; Morris, J. R., Sorption of dimethyl methylphosphonate within Langmuir-Blodgett films of trisilanolphenyl polyhedral oligomeric silsesquioxane. *Journal of Physical Chemistry B* **2005,** *109* (40), 18914-18920.

26. Novak, J. P.; Snow, E. S.; Houser, E. J.; Park, D.; Stepnowski, J. L.; McGill, R. A., Nerve agent detection using networks of single-walled carbon nanotubes. *Applied Physics Letters* **2003,** *83* (19), 4026-4028.

27. Wang, Y. Y.; Zhou, Z. H.; Yang, Z.; Chen, X. H.; Xu, D.; Zhang, Y. F., Gas sensors based on deposited single-walled carbon nanotube networks for DMMP detection. *Nanotechnology* **2009,** *20* (34).

28. Kong, L. T.; Wang, J.; Luo, T.; Meng, F. L.; Chen, X.; Li, M. Q.; Liu, J. H., Novel pyrenehexafluoroisopropanol derivative-decorated single-walled carbon nanotubes for detection of nerve agents by strong hydrogen-bonding interaction. *Analyst* **2010,** *135* (2), 368-374.

29. Kong, L. T.; Wang, J.; Fu, X. C.; Zhong, Y.; Meng, F. L.; Luo, T.; Liu, J. H., p-Hexafluoroisopropanol phenyl covalently functionalized single-walled carbon nanotubes for detection of nerve agents. *Carbon* **2010,** *48* (4), 1262-1270.

30. Fogler, H. S., *Elements of chemical reaction engineering*. 4th ed.; Prentice Hall PTR: Upper Saddle River, NJ, 2006; p xxxii, 1080 p.

31. Smith, J. M.; Van Ness, H. C.; Abbott, M. M., *Introduction to chemical engineering thermodynamics*. 7th ed.; McGraw-Hill: Boston, 2005; p xviii, 817 p.

32. Jonas, L. A.; Rehrmann, J. A., KINETICS OF ADSORPTION OF ORGANO-PHOSPHORUS VAPORS FROM AIR MIXTURES BY ACTIVATED CARBONS. *Carbon* **1972,** *10* (6), 657-&.

33. Kaplan, D.; Nir, I.; Shmueli, L., Effects of high relative humidity on the dynamic adsorption of dimethyl methylphosphonate (DMMP) on activated carbon. *Carbon* **2006,** *44* (15), 3247-3254.

34. Jang, S.; Kim, J.; Koh, Y.; Ko, Y. C.; Woo, H. G.; Sohn, H., Multi-encoded rugate porous silicon as nerve agents sensors. *Journal of Nanoscience and Nanotechnology* **2007,** *7* (11), 4049-4052.

35. Bertilsson, L.; Potje-Kamloth, K.; Liess, H. D.; Liedberg, B., On the adsorption of dimethyl methylphosphonate on self-assembled alkanethiolate monolayers: Influence of humidity. *Langmuir* **1999,** *15* (4), 1128-1135.

36. Bertilsson, L.; Engquist, I.; Liedberg, B., Interaction of dimethyl methylphosphonate with alkanethiolate monolayers studied by temperature-

programmed desorption and infrared spectroscopy. *Journal of Physical Chemistry B* **1997,** *101* (31), 6021-6027.

37. Bertilsson, L.; Potje-Kamloth, K.; Liess, H. D.; Engquist, I.; Liedberg, B., Adsorption of dimethyl methylphosphonate on self-assembled alkanethiolate monolayers. *Journal of Physical Chemistry B* **1998,** *102* (7), 1260-1269.

38. Templeton, M. K.; Weinberg, W. H., ADSORPTION AND DECOMPOSITION OF DIMETHYL METHYLPHOSPHONATE ON AN ALUMINUM-OXIDE SURFACE. *Journal of the American Chemical Society* **1985,** *107* (1), 97-108.

39. Aurianblajeni, B.; Boucher, M. M., INTERACTION OF DIMETHYL METHYLPHOSPHONATE WITH METAL-OXIDES. *Langmuir* **1989,** *5* (1), 170-174.

40. Davies, P. R.; Newton, N. G., The chemisorption of organophosphorus compounds at an Al(111) surface. *Applied Surface Science* **2001,** *181* (3-4), 296-306.

41. Mitchell, M. B.; Sheinker, V. N.; Mintz, E. A., Adsorption and decomposition of dimethyl methylphosphonate on metal oxides. *Journal of Physical Chemistry B* **1997,** *101* (51), 11192-11203.

42. Kim, C. S.; Lad, R. J.; Tripp, C. P., Interaction of organophosphorous compounds with TiO2 and WO3 surfaces probed by vibrational spectroscopy. *Sensors and Actuators B-Chemical* **2001,** *76* (1-3), 442-448.

43. Mera, N.; Hirakawa, T.; Sano, T.; Takeuchi, K.; Seto, Y.; Negishi, N., Removal of high concentration dimethyl methylphosphonate in the gas phase by repeated-batch reactions using TiO2. *Journal of Hazardous Materials* **2010,** *177* (1-3), 274-280.

44. Moss, J. A.; Szczepankiewicz, S. H.; Park, E.; Hoffmann, M. R., Adsorption and photodegradation of dimethyl methylphosphonate vapor at TiO2 surfaces. *Journal of Physical Chemistry B* **2005,** *109* (42), 19779-19785.

45. Panayotov, D. A.; Morris, J. R., Thermal Decomposition of a Chemical Warfare Agent Simulant (DMMP) on TiO2: Adsorbate Reactions with Lattice Oxygen as Studied by Infrared Spectroscopy. *Journal of Physical Chemistry C* **2009,** *113* (35), 15684-15691.

46. Panayotov, D. A.; Morris, J. R., Uptake of a Chemical Warfare Agent Simulant (DMMP) on TiO2: Reactive Adsorption and Active Site Poisoning. *Langmuir* **2009,** *25* (6), 3652-3658.

47. Rusu, C. N.; Yates, J. T., Adsorption and decomposition of dimethyl methylphosphonate on TiO2. *Journal of Physical Chemistry B* **2000,** *104* (51), 12292-12298.

48. Rusu, C. N.; Yates, J. T., Photooxidation of dimethyl methylphosphonate on TiO2 powder. *Journal of Physical Chemistry B* **2000,** *104* (51), 12299-12305.

49. Sharabi, D.; Paz, Y., Preferential photodegradation of contaminants by molecular imprinting on titanium dioxide. *Applied Catalysis B-Environmental* **2010,** *95* (1-2), 169-178.

50. Trubitsyn, D. A.; Vorontsov, A. V., Experimental study of dimethyl methylphosphonate decomposition over anatase TiO2. *Journal of Physical Chemistry B* **2005,** *109* (46), 21884-21892.

51. Zhou, J.; Varazo, K.; Reddic, J. E.; Myrick, M. L.; Chen, D. A., Decomposition of dimethyl methylphosphonate on TiO2(110): principal component analysis applied to X-ray photoelectron spectroscopy. *Analytica Chimica Acta* **2003,** *496* (1-2), 289-300.

52. Kanan, S. M.; Tripp, C. P., An infrared study of adsorbed organophosphonates on silica: A prefiltering strategy for the detection of nerve agents on metal oxide sensors. *Langmuir* **2001,** *17* (7), 2213-2218.

53. Kanan, S. M.; Tripp, C. P., Prefiltering strategies for metal oxide based sensors: The use of chemical displacers to selectively dislodge adsorbed organophosphonates from silica surfaces. *Langmuir* **2002,** *18* (3), 722-728.

54. Henderson, M. A.; Jin, T.; White, J. M., A TPD/AES STUDY OF THE INTERACTION OF DIMETHYL METHYLPHOSPHONATE WITH ALPHA-FE2O3 AND SIO2. *Journal of Physical Chemistry* **1986,** *90* (19), 4607-4611.

55. Zhao, Q.; Zhu, Q.; Shih, W. Y.; Shih, W. H., Array adsorbent-coated lead zirconate titanate (PZT)/stainless steel cantilevers for dimethyl methylphosphonate (DMMP) detection. *Sensors and Actuators B-Chemical* **2006,** *117* (1), 74-79.

56. Waghe, A.; Kanan, S. M.; Abu-Yousef, I.; Jensen, B.; Tripp, C. P., Infrared study of UV-irradiated tungsten trioxide powders containing adsorbed dimethyl methyl phosphonate and trimethyl phosphate. *Research on Chemical Intermediates* **2006,** *32* (7), 613-623.

57. Zhao, Y. Q.; He, J. H.; Yang, M. Q.; Gao, S.; Zuo, G. M.; Yan, C. X.; Cheng, Z. X., Single crystal WO3 nanoflakes as quartz crystal microbalance sensing layer for ultrafast detection of trace sarin simulant. *Analytica Chimica Acta* **2009,** *654* (2), 120-126.

58. Zhao, Y. Q.; Chen, H. M.; Wang, X. Y.; He, J. H.; Yu, Y. B.; He, H., Flower-like tungsten oxide particles: Synthesis, characterization and dimethyl methylphosphonate sensing properties. *Analytica Chimica Acta* **2010,** *675* (1), 36-41.

59. Kanan, S. M.; Lu, Z. X.; Tripp, C. P., A comparative study of the adsorption of chloro- and non-chloro-containing organophosphorus compounds on WO3. *Journal of Physical Chemistry B* **2002,** *106* (37), 9576-9580.

60. Kanan, S. M.; Waghe, A.; Jensen, B. L.; Tripp, C. P., Dual WO3 based sensors to selectively detect DMMP in the presence of alcohols. *Talanta* **2007,** *72* (2), 401-407.

61. Kanan, S. M.; Tripp, C. P., Synthesis, FTIR studies and sensor properties of WO3 powders. *Current Opinion in Solid State & Materials Science* **2007,** *11* (1-2), 19-27.

62. Kanan, S. M.; El-Kadri, O. M.; Abu-Yousef, I. A.; Kanan, M. C., Semiconducting Metal Oxide Based Sensors for Selective Gas Pollutant Detection. *Sensors* **2009,** *9* (10), 8158-8196.

63. Tomchenko, A. A.; Harmer, G. P.; Marquis, B. T., Detection of chemical warfare agents using nanostructured metal oxide sensors. *Sensors and Actuators B-Chemical* **2005,** *108* (1-2), 41-55.

64. Gordon, W. O.; Tissue, B. M.; Morris, J. R., Adsorption and decomposition of dimethyl methylphosphonate on Y2O3 nanoparticles. *Journal of Physical Chemistry C* **2007,** *111* (8), 3233-3240.

65. Chen, D. A.; Ratliff, J. S.; Hu, X. F.; Gordon, W. O.; Senanayake, S. D.; Mullins, D. R., Dimethyl methylphosphonate decomposition on fully oxidized and partially reduced ceria thin films. *Surface Science* **2010,** *604* (5-6), 574-587.

66. Mitchell, M. B.; Sheinker, V. N.; Tesfamichael, A. B.; Gatimu, E. N.; Nunley, M., Decomposition of dimethyl methylphosphonate (DMMP) on supported cerium and iron co-impregnated oxides at room temperature. *Journal of Physical Chemistry B* **2003,** *107* (2), 580-586.

67. Mitchell, M. B.; Sheinker, V. N.; Cox, W. W.; Gatimu, E. N.; Tesfamichael, A. B., The room temperature decomposition mechanism of dimethyl methylphosphonate (DMMP) on alumina-supported cerium oxide - Participation of nano-sized cerium oxide domains. *Journal of Physical Chemistry B* **2004,** *108* (5), 1634-1645.

68. Mitchell, M. B.; Sheinker, V. N.; Cox, W. W., Room temperature reaction of ozone and dimethyl methylphosphonate (DMMP) on alumina-supported iron oxide. *Journal of Physical Chemistry C* **2007,** *111* (26), 9417-9426.

69. Sberveglieri, G.; Baratto, C.; Comini, E.; Faglia, G.; Ferroni, M.; Pardo, M.; Ponzoni, A.; Vomiero, A., Semiconducting tin oxide nanowires and thin films for Chemical Warfare Agents detection. *Thin Solid Films* **2009,** *517* (22), 6156-6160.

70. Brunol, E.; Berger, F.; Fromm, A.; Planade, R., Detection of dimethyl methylphosphonate (DMMP) by tin dioxide-based gas sensor: Response curve and understanding of the reactional mechanism. *Sensors and Actuators B-Chemical* **2006,** *120* (1), 35-41.

71. Li, Y. X.; Koper, O.; Atteya, M.; Klabunde, K. J., ADSORPTION AND DECOMPOSITION OF ORGANOPHOSPHORUS COMPOUNDS ON NANOSCALE METAL-OXIDE PARTICLES - INSITU GC-MS STUDIES OF PULSED MICROREACTIONS OVER MAGNESIUM-OXIDE. *Chemistry of Materials* **1992,** *4* (2), 323-330.

72. Lee, W. S.; Lee, S. C.; Lee, S. J.; Lee, D. D.; Huh, J. S.; Jun, H. K.; Kim, J. C., The sensing behavior of SnO2-based thick-film gas sensors at a low concentration of chemical agent simulants. *Sensors and Actuators B-Chemical* **2005,** *108* (1-2), 148-153.

73. Lee, W. S.; Choi, H. Y.; Lee, S. C.; Lee, S. J.; Lee, D. D.; Huh, J. S.; Kim, J. C., Recoverable SnO2-based sensors promoted with MoO3 and Sb2O3 for the detection of DMMP. *Rare Metal Materials and Engineering* **2006,** *35*, 155-156.

74. Ponzoni, A.; Baratto, C.; Bianchi, S.; Comini, E.; Ferroni, M.; Pardo, M.; Vezzoli, M.; Vomiero, A.; Faglia, G.; Sberveglieri, G., Metal oxide nanowire and thin-film-based gas sensors for chemical warfare simulants detection. *Ieee Sensors Journal* **2008,** *8* (5-6), 735-742.

75. Oh, S. W.; Kim, Y. H.; Yoo, D. J.; Oh, S. M.; Park, S. J., SENSING BEHAVIOR OF SEMICONDUCTING METAL-OXIDES FOR THE DETECTION OF ORGANOPHOSPHORUS COMPOUNDS. *Sensors and Actuators B-Chemical* **1993,** *13* (1-3), 400-403.

76. Ma, S.; Zhou, J.; Kang, Y. C.; Reddic, J. E.; Chen, D. A., Dimethyl methylphosphonate decomposition on Cu surfaces: Supported Cu nanoclusters and films on TiO2(110). *Langmuir* **2004,** *20* (22), 9686-9694.

77. Panayotov, D. A.; Morris, J. R., Catalytic degradation of a chemical warfare agent simulant: Reaction mechanisms on TiO2-supported Au nanoparticles. *Journal of Physical Chemistry C* **2008,** *112* (19), 7496-7502.

78. Ratliff, J. S.; Tenney, S. A.; Hu, X. F.; Conner, S. F.; Ma, S. G.; Chen, D. A., Decomposition of Dimethyl Methylphosphonate on Pt, Au, and Au-Pt Clusters Supported on. TiO2(110). *Langmuir* **2009,** *25* (1), 216-225.

79. Li, X. G.; Dutta, P. K., Interaction of Dimethylmethylphosphonate with Zeolite Y: Impedance-Based Sensor for Detecting Nerve Agent Simulants. *Journal of Physical Chemistry C* **2010,** *114* (17), 7986-7994.

80. Xie, H. F.; Yang, Q. D.; Sun, X. X.; Yu, T.; Zhou, J.; Huang, Y. P., Gas sensors based on nanosized-zeolite films to identify dimethylmethylphosphonate. *Sensors and Materials* **2005,** *17* (1), 21-28.

81. Knagge, K.; Johnson, M.; Grassian, V. H.; Larsen, S. C., Adsorption and thermal reaction of DMMP in nanocrystalline NaY. *Langmuir* **2006,** *22* (26), 11077-11084.

82. Ferguson-McPherson, M. K.; Low, E. R.; Esker, A. R.; Morris, J. R., Corner capping of silsesquioxane cages by chemical warfare agent simulants. *Langmuir* **2005,** *21* (24), 11226-11231.

83. Wang, W.; He, S. T., Theoretical analysis on response mechanism of polymer-coated chemical sensor based Love wave in viscoelastic media. *Sensors and Actuators B-Chemical* **2009,** *138* (2), 432-440.

84. Ying, Z. H.; Jiang, Y. D.; Du, X. S.; Xie, G. Z.; Yu, J. S.; Wang, H., PVDF coated quartz crystal microbalance sensor for DMMP vapor detection. *Sensors and Actuators B-Chemical* **2007,** *125* (1), 167-172.

85. Bryant, C. K.; LaPuma, P. T.; Hook, G. L.; Houser, E. J., Chemical agent identification by field-based attenuated total reflectance infrared detection and solid-phase microextraction. *Analytical Chemistry* **2007,** *79* (6), 2334-2340.

86. Grate, J. W., Hydrogen-bond acidic polymers for chemical vapor sensing. *Chemical Reviews* **2008,** *108* (2), 726-745.

87. Levitsky, I. A.; Krivoshlykov, S. G. Method for detection of organic vapors based on fluorescence enhancement in porphyrin aggregates. US 6623973.

88. Levitsky, I.; Krivoshlykov, S. G.; Grate, J. W., Rational design of a Nile Red/polymer composite film for fluorescence sensing of organophosphonate vapors using hydrogen bond acidic polymers. *Analytical Chemistry* **2001,** *73* (14), 3441-3448.

89. Huang, J.; Jiang, Y. D.; Du, X. S.; Bi, J., A new siloxane polymer for chemical vapor sensor. *Sensors and Actuators B-Chemical* **2010,** *146* (1), 388-394.

90. Zimmermann, C.; Mazein, P.; Rebiere, D.; Dejous, C.; Pistre, J.; Planade, R., Detection of GB and DMMP vapors by love wave acoustic sensors using strong acidic fluoride polymers. *Ieee Sensors Journal* **2004,** *4* (4), 479-488.

91. Du, X. S.; Ying, Z. H.; Jiang, Y. D.; Liu, Z. X.; Yang, T. J.; Xie, G. Z., Synthesis and evaluation of a new polysiloxane as SAW sensor coatings for DMMP detection. *Sensors and Actuators B-Chemical* **2008,** *134* (2), 409-413.

92. Du, X. S.; Wang, Z. D.; Huang, J.; Tao, S. L.; Tang, X. Z.; Jiang, Y. D., A new polysiloxane coating on QCM sensor for DMMP vapor detection. *Journal of Materials Science* **2009,** *44* (21), 5872-5876.

93. Liu, M. M.; Zeng, Z. R.; Wang, C. L.; Tan, Y. J.; Liu, H., Solid-phase microextraction of phosphate and methylphosphonate using novel fibers coated

with a sol-gel-derived silicone divinyl benzene co-polymer. *Chromatographia* **2003,** *58* (9-10), 597-605.

94. Riter, L. S.; Takats, Z.; Cooks, R. G., Single-sided membrane introduction mass spectrometry for on-line determination of semi-volatile organic compounds in air. *Analyst* **2001,** *126* (11), 1980-1984.

95. He, W.; Liu, Z. X.; Du, X. S.; Jiang, Y. D.; Xiao, D., Analytical application of poly{methyl 3-(2-hydroxy-3,4-difluoro)phenyl propyl siloxane} as a QCM coating for DMMP detection. *Talanta* **2008,** *76* (3), 698-702.

96. Manginell, R. P.; Adkins, D. R.; Moorman, M. W.; Hadizadeh, R.; Copic, D.; Porter, D. A.; Anderson, J. M.; Hietala, V. M.; Bryan, J. R.; Wheeler, D. R.; Pfeifer, K. B.; Rumpf, A., Mass-Sensitive Microfabricated Chemical Preconcentrator. *Journal of Microelectromechanical Systems* **2008,** *17* (6), 1396-1407.

97. Khalil, S.; Bansal, L.; El-Sherif, M., Intrinsic fiber optic chemical sensor for the detection of dimethyl methylphosphonate. *Optical Engineering* **2004,** *43* (11), 2683-2688.

98. Hartmann-Thompson, C.; Keeley, D. L.; Rousseau, J. R.; Dvornic, P. R., Fluorescent Dendritic Polymers and Nanostructured Coatings for the Detection of Chemical Warfare Agents and Other Analytes. *Journal of Polymer Science Part a-Polymer Chemistry* **2009,** *47* (19), 5101-5115.

99. Wen, W.; He, S. T.; Li, S. Z.; Liu, M. H.; Yong, P., Enhanced sensitivity of SAW gas sensor coated molecularly imprinted polymer incorporating high frequency stability oscillator. *Sensors and Actuators B-Chemical* **2007,** *125* (2), 422-427.

100. Collins, G. E.; Buckley, L. J., Conductive polymer-coated fabrics for chemical sensing. *Synthetic Metals* **1996,** *78* (2), 93-101.

101. Chang, C. P.; Yuan, C. L., The fabrication of a MWNTs-polymer composite chemoresistive sensor array to discriminate between chemical toxic agents. *Journal of Materials Science* **2009,** *44* (20), 5485-5493.

102. Reid, V. R.; Crank, J. A.; Armstrong, D. W.; Synovec, R. E., Characterization and utilization of a novel triflate ionic liquid stationary phase for use in comprehensive two-dimensional gas chromatography. *Journal of Separation Science* **2008,** *31* (19), 3429-3436.

103. Bungabong, M. L.; Ong, P. B.; Yang, K. L., Using copper perchlorate doped liquid crystals for the detection of organophosphonate vapor. *Sensors and Actuators B-Chemical* **2010,** *148* (2), 420-426.

104. Cadwell, K. D.; Lockwood, N. A.; Nellis, B. A.; Alf, M. E.; Willis, C. R.; Abbott, N. L., Detection of organophosphorous nerve agents using liquid crystals

supported on chemically functionalized surfaces. *Sensors and Actuators B-Chemical* **2007,** *128* (1), 91-98.

105. Sridharamurthy, S. S.; Cadwell, K. D.; Abbott, N. L.; Jiang, H., A microstructure for the detection of vapor-phase analytes based on orientational transitions of liquid crystals. *Smart Materials & Structures* **2008,** *17* (1).

106. Yang, K. L.; Cadwell, K.; Abbott, N. L., Use of self-assembled monolayers, metal ions and smectic liquid crystals to detect organophosphonates. *Sensors and Actuators B-Chemical* **2005,** *104* (1), 50-56.

107. Rekha, K.; Gouda, M. D.; Thakur, M. S.; Karanth, N. G., Ascorbate oxidase based amperometric biosensor for organophosphorous pesticide monitoring. *Biosensors & Bioelectronics* **2000,** *15* (9-10), 499-502.

108. Deo, R. P.; Wang, J.; Block, I.; Mulchandani, A.; Joshi, K. A.; Trojanowicz, M.; Scholz, F.; Chen, W.; Lin, Y. H., Determination of organophosphate pesticides at a carbon nanotube/organophosphorus hydrolase electrochemical biosensor. *Analytica Chimica Acta* **2005,** *530* (2), 185-189.

109. Mansee, A. H.; Chen, W.; Mulchandani, A., Detoxification of the organophosphate nerve agent coumaphos using organophosphorus hydrolase immobilized on cellulose materials. *Journal of Industrial Microbiology & Biotechnology* **2005,** *32* (11-12), 554-560.

110. Lin, Y. H.; Lu, F.; Wang, J., Disposable carbon nanotube modified screen-printed biosensor for amperometric detection of organophosphorus pesticides and nerve agents. *Electroanalysis* **2004,** *16* (1-2), 145-149.

111. Simonian, A. L.; Flounders, A. W.; Wild, J. R., FET-based biosensors for the direct detection of organophosphate neurotoxins. *Electroanalysis* **2004,** *16* (22), 1896-1906.

112. Viveros, L.; Paliwal, S.; McCrae, D.; Wild, J.; Simonian, A., A fluorescence-based biosensor for the detection of organophosphate pesticides and chemical warfare agents. *Sensors and Actuators B-Chemical* **2006,** *115* (1), 150-157.

113. Lei, Y.; Mulchandani, P.; Wang, J.; Chen, W.; Mulchandani, A., Highly sensitive and selective amperometric microbial biosensor for direct determination of p-nitrophenyl-substituted organophosphate nerve agents. *Environmental Science & Technology* **2005,** *39* (22), 8853-8857.

114. Zourob, M.; Ong, K. G.; Zeng, K. F.; Mouffouk, F.; Grimes, C. A., A wireless magnetoelastic biosensor for the direct detection of organophosphorus pesticides. *Analyst* **2007,** *132* (4), 338-343.

115. Huo, D. Q.; Yang, L. M.; Hou, C. J., Optical Detection of Dimethyl Methyl-Phosphonate with Monosulfonate Tetraphenyl Porphyrin-Plant-Esterase Complex. *Sensor Letters* **2009,** *7* (1), 72-78.

116. Fierro, J. L. G., *Metal oxides : chemistry and applications*. Taylor & Francis: Boca Raton, FL, 2006; p xxi, 783 p.

117. Wahl, J. H.; Colburn, H. A., Extraction of chemical impurities for forensic investigations: A case study for indoor releases of a sarin surrogate. *Building and Environment* **2010,** *45* (5), 1339-1345.

118. Du, D.; Ye, X. P.; Zhang, J. D.; Zeng, Y.; Tu, H. Y.; Zhang, A. D.; Liu, D. L., Stripping voltammetric analysis of organophosphate pesticides based on solid-phase extraction at zirconia nanoparticles modified electrode. *Electrochemistry Communications* **2008,** *10* (5), 686-690; Liu, G. D.; Lin, Y. H., Electrochemical sensor for organophosphate pesticides and nerve agents using zirconia nanoparticles as selective sorbents. *Analytical Chemistry* **2005,** *77* (18), 5894-5901; Liu, G. D.; Wang, J.; Barry, R.; Petersen, C.; Timchalk, C.; Gassman, P. L.; Lin, Y. H., Nanoparticle-Based Electrochemical Immunosensor for the Detection of Phosphorylated Acetylcholinesterase: An Exposure Biomarker of Organophosphate Pesticides and Nerve Agents. *Chemistry-a European Journal* **2008,** *14* (32), 9951-9959.

119. Tan, X. H.; Li, B. H.; Zhan, G. Q.; Li, C. Y., Sensitive Voltammetric Determination of Methyl Parathion Using a Carbon Paste Electrode Modified with Mesoporous Zirconia. *Electroanalysis* **2010,** *22* (2), 151-154.

120. Parham, H.; Rahbar, N., Square wave voltammetric determination of methyl parathion using ZrO2-nanoparticles modified carbon paste electrode. *Journal of Hazardous Materials* **2010,** *177* (1-3), 1077-1084.

121. Bermudez, V. M., Quantum-chemical study of the adsorption of DMMP and sarin on gamma-Al2O3. *Journal of Physical Chemistry C* **2007,** *111* (9), 3719-3728.

122. Bermudez, V. M., Energy-level alignment in the adsorption of phosphonyl reagents on gamma-Al2O3. *Surface Science* **2008,** *602* (11), 1938-1947.

123. Bermudez, V. M., Computational Study of Environmental Effects in the Adsorption of DMMP, Sarin, and VX on gamma-Al2O3: Photolysis and Surface Hydroxylation. *Journal of Physical Chemistry C* **2009,** *113* (5), 1917-1930.

124. Sing, K. S. W., REPORTING PHYSISORPTION DATA FOR GAS SOLID SYSTEMS - WITH SPECIAL REFERENCE TO THE DETERMINATION OF SURFACE-AREA AND POROSITY. *Pure and Applied Chemistry* **1982,** *54* (11), 2201-2218.

125. Sing, K. S. W.; Everett, D. H.; Haul, R. A. W.; Moscou, L.; Pierotti, R. A.; Rouquerol, J.; Siemieniewska, T., REPORTING PHYSISORPTION DATA FOR

GAS SOLID SYSTEMS WITH SPECIAL REFERENCE TO THE DETERMINATION OF SURFACE-AREA AND POROSITY (RECOMMENDATIONS 1984). *Pure and Applied Chemistry* **1985,** *57* (4), 603-619.

126. Cramer, C. J.; Truhlar, D. G., Density functional theory for transition metals and transition metal chemistry. *Physical Chemistry Chemical Physics* **2009,** *11* (46), 10757-10816.

127. Singh, J., *Smart electronic materials : fundamentals and applications*. Cambridge University Press: Cambridge ; New York, 2005; p xxii, 408 p.

128. Heiz, U.; Landman, U., *Nanocatalysis*. Springer: Berlin, 2007; p xvi, 503 p.

129. Frisch, M. J. T., G. W.; Schlegel, H. B.; Scuseria, G. E.; Robb, M. A.; Cheeseman, J. R.; Montgomery, J., J. A.; Vreven, T.; Kudin, K. N.; Burant, J. C.; Millam, J. M.; Iyengar, S. S.; Tomasi, J.; Barone, V.; Mennucci, B.; Cossi, M.; Scalmani, G.; Rega, N.; Petersson, G. A.; Nakatsuji, H.; Hada, M.; Ehara, M.; Toyota, K.; Fukuda, R.; Hasegawa, J.; Ishida, M.; Nakajima, T.; Honda, Y.; Kitao, O.; Nakai, H.; Klene, M.; Li, X.; Knox, J. E.; Hratchian, H. P.; Cross, J. B.; Bakken, V.; Adamo, C.; Jaramillo, J.; Gomperts, R.; Stratmann, R. E.; Yazyev, O.; Austin, A. J.; Cammi, R.; Pomelli, C.; Ochterski, J. W.; Ayala, P. Y.; Morokuma, K.; Voth, G. A.; Salvador, P.; Dannenberg, J. J.; Zakrzewski, V. G.; Dapprich, S.; Daniels, A. D.; Strain, M. C.; Farkas, O.; Malick, D. K.; Rabuck, A. D.; Raghavachari, K.; Foresman, J. B.; Ortiz, J. V.; Cui, Q.; Baboul, A. G.; Clifford, S.; Cioslowski, J.; Stefanov, B. B.; Liu, G.; Liashenko, A.; Piskorz, P.; Komaromi, I.; Martin, R. L.; Fox, D. J.; Keith, T.; Al-Laham, M. A.; Peng, C. Y.; Nanayakkara, A.; Challacombe, M.; Gill, P. M. W.; Johnson, B.; Chen, W.; Wong, M. W.; Gonzalez, C.; and Pople, J. A., *Gaussian 03, Revision C.02*. Wallingford, CT: Gaussian, Inc., 2004.

130. Ochterski, J. W. *Thermochemistry in Gaussian*; Gaussian, Inc.: 2000.

131. Cuisset, A.; Mouret, G.; Pirali, O.; Roy, P.; Cazier, F.; Nouali, H.; Demaison, J., Gas-phase vibrational spectroscopy and ab initio study of organophosphorous compounds: Discrimination between species and conformers. *Journal of Physical Chemistry B* **2008,** *112* (39), 12516-12525.

132. DaBell, R. S.; Suenram, R. D.; Lavrich, R. J.; Lochner, J. M.; Ellzy, M. W.; Sumpter, K.; Jensen, J. O.; Samuels, A. C., The geometry of organophosphonates: Fourier-transform microwave spectroscopy and ab initio study of diethyl methylphosphonate, diethyl ethylphosphonate, and diisopropyl methylphosphonate. *Journal of Molecular Spectroscopy* **2004,** *228* (2), 230-242.

133. Sundararajan, K.; Sankaran, K., Conformations of dimethylhydrogen phosphonate (DMHP): A matrix isolation infrared and ab initio study. *Journal of Physical Chemistry A* **2008,** *112* (26), 5917-5924.

134. Suenram, R. D.; Lovas, F. J.; Plusquellic, D. F.; Lesarri, A.; Kawashima, Y.; Jensen, J. O.; Samuels, A. C., Fourier transform microwave spectrum and ab initio study of dimethyl methylphosphonate. *Journal of Molecular Spectroscopy* **2002,** *211* (1), 110-118.

135. Yang, L.; Shroll, R. M.; Zhang, J. X.; Lourderaj, U.; Hase, W. L., Theoretical Investigation of Mechanisms for the Gas-Phase Unimolecular Decomposition of DMMP. *Journal of Physical Chemistry A* **2009,** *113* (49), 13762-13771.

136. Martin-Samos, L.; Limoge, Y.; Roma, G., Defects in amorphous SiO2: Valence alternation pair model. *Physical Review B* **2007,** *76* (10).

137. Mysovsky, A. S.; Sushko, P. V.; Mukhopadhyay, S.; Edwards, A. H.; Shluger, A. L., Calibration of embedded-cluster method for defect studies in amorphous silica. *Physical Review B* **2004,** *69* (8), 10.

138. Sushko, P. V.; Mukhopadhyay, S.; Mysovsky, A. S.; Sulimov, V. B.; Taga, A.; Shluger, A. L., Structure and properties of defects in amorphous silica: new insights from embedded cluster calculations. *Journal of Physics-Condensed Matter* **2005,** *17* (21), S2115-S2140.

139. Pasquarello, A.; Sarnthein, J.; Car, R., Dynamic structure factor of vitreous silica from first principles: Comparison to neutron-inelastic-scattering experiments. *Physical Review B* **1998,** *57* (22), 14133-14140.

140. Pasquarello, A., Analysis of structural and dynamic properties by molecular dynamics ab initio: Application to glasses and vitreous liquids. *Journal De Physique Iv* **2003,** *111*, 373-393.

141. Sarnthein, J.; Pasquarello, A.; Car, R., MODEL OF VITREOUS SIO2 GENERATED BY AN AB-INITIO MOLECULAR-DYNAMICS QUENCH FROM THE MELT. *Physical Review B* **1995,** *52* (17), 12690-12695.

142. Sarnthein, J.; Pasquarello, A.; Car, R., STRUCTURAL AND ELECTRONIC-PROPERTIES OF LIQUID AND AMORPHOUS SIO2 - AN AB-INITIO MOLECULAR-DYNAMICS STUDY. *Physical Review Letters* **1995,** *74* (23), 4682-4685.

143. Giacomazzi, L.; Umari, P.; Pasquarello, A., Medium-range structure of vitreous SiO2 obtained through first-principles investigation of vibrational spectra. *Physical Review B* **2009,** *79* (6).

144. Cabriolu, R.; Ballone, P., Thermodynamic properties and atomistic structure of the dry amorphous silica surface from a reactive force field model. *Physical Review B* **2010,** *81* (15), 12.

145. Charpentier, T.; Kroll, P.; Mauri, F., First-Principles Nuclear Magnetic Resonance Structural Analysis of Vitreous Silica. *Journal of Physical Chemistry C* **2009,** *113* (18), 7917-7929.

146. Uchino, T.; Yoko, T., Localized low-frequency dynamics in SiO2 glass. *Journal of Chemical Physics* **1998,** *108*, 8130-8138.

147. Uchino, T.; Kitagawa, Y.; Yoko, T., Structure, energies, and vibrational properties of silica rings in SiO2 glass. *Physical Review B* **2000,** *61* (1), 234-240.

148. Uchino, T., Ab initio cluster calculations on point defects in amorphous SiO2. *Current Opinion in Solid State & Materials Science* **2001,** *5* (6), 517-523.

149. Benoit, M.; Ispas, S.; Jund, P.; Jullien, R., Model of silica glass from combined classical and ab initio molecular-dynamics simulations. *European Physical Journal B* **2000,** *13* (4), 631-636.

150. Huff, N. T.; Demiralp, E.; Cagin, T.; Goddard, W. A., Factors affecting molecular dynamics simulated vitreous silica structures. *Journal of Non-Crystalline Solids* **1999,** *253*, 133-142.

151. Mei, Q.; Benmore, C. J.; Sen, S.; Sharma, R.; Yarger, J. L., Intermediate range order in vitreous silica from a partial structure factor analysis. *Physical Review B* **2008,** *78* (14).

152. Mischler, C.; Kob, W.; Binder, K., Classical and ab-initio molecular dynamic simulation of an amorphous silica surface. *Computer Physics Communications* **2002,** *147* (1-2), 222-225.

153. Hung, P. K.; Nhan, N. T., Polyamorphism in the silica glass. *Scripta Materialia* **2010,** *63* (1), 12-15.

154. Van Ginhoven, R. M.; Jonsson, H.; Corrales, L. R., Silica glass structure generation for ab initio calculations using small samples of amorphous silica. *Physical Review B* **2005,** *71* (2).

155. Woodcock, L. V.; Angell, C. A.; Cheeseman, P., MOLECULAR-DYNAMICS STUDIES OF VITREOUS STATE - SIMPLE IONIC SYSTEMS AND SILICA. *Journal of Chemical Physics* **1976,** *65* (4), 1565-1577.

156. Zhang, R. Q.; Fan, W. J., Structures and properties of silicon oxide clusters by theoretical investigations. *Journal of Cluster Science* **2006,** *17* (4), 541-563.

157. Song, J. Y.; Choi, M., Stability of elongated and compact types of structures in SiO2 nanoparticles. *Physical Review B* **2002,** *65* (24).

158. Lucovsky, G.; Mowrer, T.; Sremaniak, L. S.; Whitten, J. L., Local atomic structure and infrared effective charges in tetrahedrally-bonded glasses from ab

initio theory electronic structure calculations. *Journal of Non-Crystalline Solids* **2004,** *338*, 155-158.

159. Tielens, F.; Gervais, C.; Lambert, J. F.; Mauri, F.; Costa, D., Ab initio study of the hydroxylated surface of amorphous silica: A representative model. *Chemistry of Materials* **2008,** *20* (10), 3336-3344.

160. Ugliengo, P.; Sodupe, M.; Musso, F.; Bush, I. J.; Orlando, R.; Dovesi, R., Realistic Models of Hydroxylated Amorphous Silica Surfaces and MCM-41 Mesoporous Material Simulated by Large-scale Periodic B3LYP Calculations. *Advanced Materials* **2008,** *20* (23), 4579-4583.

161. Cheng, H. P.; Barnett, R. N.; Landman, U., Structure, collective hydrogen transfer, and formation of Si(OH)(4) in SiO2-(H2O)(n) clusters. *Journal of Chemical Physics* **2002,** *116* (21), 9300-9304.

162. Ma, Y. C.; Foster, A. S.; Nieminen, R. M., Reactions and clustering of water with silica surface. *Journal of Chemical Physics* **2005,** *122* (14), 9.

163. Van Ginhoven, R. M.; Jonsson, H.; Park, B.; Corrales, L. R., Cleavage and recovery of molecular water in silica. *Journal of Physical Chemistry B* **2005,** *109* (21), 10936-10945.

164. Leed, E. A.; Sofo, J. O.; Pantano, C. G., Electronic structure calculations of physisorption and chemisorption on oxide glass surfaces. *Physical Review B* **2005,** *72* (15).

165. Hamann, D. R., Generalized gradient theory for silica phase transitions. *Physical Review Letters* **1996,** *76* (4), 660-663.

166. Demuth, T.; Jeanvoine, Y.; Hafner, J.; Angyan, J. G., Polymorphism in silica studied in the local density and generalized-gradient approximations. *Journal of Physics-Condensed Matter* **1999,** *11* (19), 3833-3874.

167. Sevik, C.; Bulutay, C., Theoretical study of the insulating oxides and nitrides: SiO2, GeO2, Al2O3, Si3N4, and Ge3N4. *Journal of Materials Science* **2007,** *42* (16), 6555-6565.

168. Civalleri, B.; Casassa, S.; Garrone, E.; Pisani, C.; Ugliengo, P., Quantum mechanical ab initio characterization of a simple periodic model of the silica surface. *Journal of Physical Chemistry B* **1999,** *103* (12), 2165-2171.

169. Cabriolu, R.; Del Popolo, M. G.; Ballone, P., Melting of a tetrahedral network model of silica. *Physical Chemistry Chemical Physics* **2009,** *11* (46), 10820-10823.

170. Ehrburger-Dolle, F., A new way to analyze adsorption isotherms. *Langmuir* **1999,** *15* (18), 6004-6015.

171. Toth, J., UNIFORM INTERPRETATION OF GAS-SOLID ADSORPTION. *Advances in Colloid and Interface Science* **1995,** *55*, 1-239.

172. Flood, E. A., *The solid-gas interface*. M. Dekker: New York,, 1967; p 2 v.

173. Dabrowski, A., Adsorption - from theory to practice. *Advances in Colloid and Interface Science* **2001,** *93* (1-3), 135-224.

174. Timmermann, E. O., Multilayer sorption parameters: BET or GAB values? *Colloids and Surfaces a-Physicochemical and Engineering Aspects* **2003,** *220* (1-3), 235-260.

175. Aranovich, G. L.; Donohue, M. D., Predictions of multilayer adsorption using lattice theory. *Journal of Colloid and Interface Science* **1997,** *189* (1), 101-108.

176. Kim, D., Statistically modeled adsorption isotherms for the multilayer gas molecules adsorbed on non-porous solid adsorbents of two and three groups sites. *Korean Journal of Chemical Engineering* **2000,** *17* (2), 156-168.

177. Yang, R. T., *Adsorbents : fundamentals and applications*. Wiley-Interscience: Hoboken, N.J., 2003; p xii, 410 p.

178. Tóth, J., *Adsorption : theory, modeling, and analysis*. Marcel Dekker: New York, 2002; p viii, 878 p.

179. Zhou, W.; Wu, H.; Hartman, M. R.; Yildirim, T., Hydrogen and methane adsorption in metal-organic frameworks: A high-pressure volumetric study. *Journal of Physical Chemistry C* **2007,** *111*, 16131-16137.

180. Goss, K. U.; Eisenreich, S. J., Adsorption of VOCs from the gas phase to different minerals and a mineral mixture. *Environmental Science & Technology* **1996,** *30* (7), 2135-2142.

181. Ewing, K. J.; Dagenais, D. M.; Bucholtz, F.; Aggarwal, I. D., Fiber-optic Raman detection of trace levels of phosphonate vapors chemisorbed onto an alumina substrate. *Applied Spectroscopy* **1996,** *50* (5), 614-618.

182. Kuwabara, A.; Tohei, T.; Yamamoto, T.; Tanaka, I., Ab initio lattice dynamics and phase transformations of ZrO2. *Physical Review B* **2005,** *71* (6).

183. Zhao, X. Y.; Vanderbilt, D., Phonons and lattice dielectric properties of zirconia. *Physical Review B* **2002,** *65* (7).

184. Zhao, X. Y.; Ceresoli, D.; Vanderbilt, D., Structural, electronic, and dielectric properties of amorphous ZrO2 from ab initio molecular dynamics. *Physical Review B* **2005,** *71* (8).

185. Vanderbilt, D.; Zhao, X. Y.; Ceresoli, D., Structural and dielectric properties of crystalline and amorphous ZrO2. *Thin Solid Films* **2005,** *486* (1-2), 125-128.

186. Parlinski, K.; Li, Z. Q.; Kawazoe, Y., First-principles determination of the soft mode in cubic ZrO2. *Physical Review Letters* **1997,** *78* (21), 4063-4066.

187. Sternik, M.; Parlinski, K., Lattice vibrations in cubic, tetragonal, and monoclinic phases of ZrO2. *Journal of Chemical Physics* **2005,** *122* (6).

188. Rignanese, G. M.; Detraux, F.; Gonze, X.; Pasquarello, A., First-principles study of dynamical and dielectric properties of tetragonal zirconia. *Physical Review B* **2001,** *64* (13).

189. Rignanese, G. M.; Gonze, X.; Jun, G.; Cho, K. J.; Pasquarello, A., First-principles investigation of high-kappa dielectrics: Comparison between the silicates and oxides of hafnium and zirconium. *Physical Review B* **2004,** *69* (18).

190. Ching, W. Y.; Ouyang, L. Z.; Rulis, P.; Yao, H. Z., Ab initio study of the physical properties of gamma-Al2O3: Lattice dynamics, bulk properties, electronic structure, bonding, optical properties, and ELNES/XANES spectra. *Physical Review B* **2008,** *78* (1).

191. Pinto, H. P.; Nieminen, R. M.; Elliott, S. D., Ab initio study of gamma-Al2O3 surfaces. *Physical Review B* **2004,** *70* (12).

192. Mo, S. D.; Xu, Y. N.; Ching, W. Y., Electronic and structural properties of bulk gamma-Al2O3. *Journal of the American Ceramic Society* **1997,** *80* (5), 1193-1197.

193. Gutierrez, G.; Taga, A.; Johansson, B., Theoretical structure determination of gamma-Al2O3. *Physical Review B* **2002,** *65* (1).

194. Menendez-Proupin, E.; Gutierrez, G., Electronic properties of bulk gamma-Al2O3. *Physical Review B* **2005,** *72* (3), 9.

195. Paglia, G.; Buckley, C. E.; Rohl, A. L.; Hunter, B. A.; Hart, R. D.; Hanna, J. V.; Byrne, L. T., Tetragonal structure model for boehmite-derived gamma-alumina. *Physical Review B* **2003,** *68* (14), 11.

196. Paglia, G.; Rohl, A. L.; Buckley, C. E.; Gale, J. D., Determination of the structure of gamma-alumina from interatomic potential and first-principles calculations: The requirement of significant numbers of nonspinel positions to achieve an accurate structural model. *Physical Review B* **2005,** *71* (22), 16.

197. Krokidis, X.; Raybaud, P.; Gobichon, A. E.; Rebours, B.; Euzen, P.; Toulhoat, H., Theoretical study of the dehydration process of boehmite to gamma-alumina. *Journal of Physical Chemistry B* **2001,** *105* (22), 5121-5130.

198. Digne, M.; Sautet, P.; Raybaud, P.; Euzen, P.; Toulhoat, H., Use of DFT to achieve a rational understanding of acid-basic properties of gamma-alumina surfaces. *Journal of Catalysis* **2004,** *226* (1), 54-68.

199. Digne, M.; Raybaud, P.; Sautet, P.; Rebours, B.; Toulhoat, H., Comment on "Examination of spinel and nonspinel structural models for gamma-Al2O3 by DFT and Rietveld refinement simulations". *Journal of Physical Chemistry B* **2006,** *110* (41), 20719-20720.

200. Sun, M. Y.; Nelson, A. E.; Adjaye, J., Examination of spinel and nonspinel structural models for gamma-Al2O3 by DFT and Rietveld refinement simulations. *Journal of Physical Chemistry B* **2006,** *110* (5), 2310-2317.

201. Paglia, G.; Buckley, C. E.; Rohl, A. L., Comment on "Examination of spinel and nonspinel structural models for gamma-Al2O3 by DFT and rietveld refinement simulations". *Journal of Physical Chemistry B* **2006,** *110* (41), 20721-20723.

202. Ganduglia-Pirovano, M. V.; Hofmann, A.; Sauer, J., Oxygen vacancies in transition metal and rare earth oxides: Current state of understanding and remaining challenges. *Surface Science Reports* **2007,** *62* (6), 219-270.

203. Orlando, R.; Pisani, C.; Roetti, C.; Stefanovich, E., ABINITIO HARTREE-FOCK STUDY OF TETRAGONAL AND CUBIC PHASES OF ZIRCONIUM DIOXIDE. *Physical Review B* **1992,** *45* (2), 592-601.

204. Orlando, R.; Pisani, C.; Ruiz, E.; Sautet, P., ABINITIO STUDY OF THE BARE AND HYDRATED (001) SURFACE OF TETRAGONAL ZIRCONIA. *Surface Science* **1992,** *275* (3), 482-492.

205. Hofmann, A.; Clark, S. J.; Oppel, M.; Hahndorf, I., Hydrogen adsorption on the tetragonal ZrO2(101) surface: a theoretical study of an important catalytic reactant. *Physical Chemistry Chemical Physics* **2002,** *4* (14), 3500-3508.

206. Haase, F.; Sauer, J., The surface structure of sulfated zirconia: Periodic ab initio study of sulfuric acid adsorbed on ZrO2(101) and ZrO2(001). *Journal of the American Chemical Society* **1998,** *120* (51), 13503-13512.

207. Okamoto, Y., First-principles molecular dynamics simulation of O-2 reduction on ZrO2 ((1)over-bar 1 1) surface. *Applied Surface Science* **2008,** *255* (5), 3434-3441.

208. Diaz-Dieza, M. A.; Macias-Garcia, A.; Silvero, G.; Gordillo, R.; Caruso, R., Theoretical study of the molecular structure for zirconium complexes. *Ceramics International* **2003,** *29* (4), 471-475.

209. Trubelja, M. P.; Potter, D.; Helble, J. J., Effect of process conditions on phase mixtures of sol-gel-synthesized nanoscale orthorhombic, tetragonal, and monoclinic zirconia. *Journal of Materials Science* **2010,** *45* (16), 4480-4489.

210. Li, W. Z.; Huang, H.; Li, H. J.; Zhang, W.; Liu, H. C., Facile synthesis of pure monoclinic and tetragonal zirconia nanoparticles and their phase effects on the behavior of supported molybdena catalysts for methanol-selective oxidation. *Langmuir* **2008,** *24* (15), 8358-8366.

211. Rashad, M. M.; Baioumy, H. M., Effect of thermal treatment on the crystal structure and morphology of zirconia nanopowders produced by three different routes. *Journal of Materials Processing Technology* **2008,** *195* (1-3), 178-185.

212. Tyagi, B.; Sidhpuria, K.; Shaik, B.; Jasra, R. V., Synthesis of nanocrystalline zirconia using sol-gel and precipitation techniques. *Industrial & Engineering Chemistry Research* **2006,** *45* (25), 8643-8650.

213. Jung, K. T.; Bell, A. T., The effects of synthesis and pretreatment conditions on the bulk structure and surface properties of zirconia. *Journal of Molecular Catalysis a-Chemical* **2000,** *163* (1-2), 27-42.

214. Matos, J. M. E.; Anjos, F. M.; Cavalcante, L. S.; Santos, V.; Leal, S. H.; Santos, L. S.; Santos, M.; Longo, E., Reflux synthesis and hydrothermal processing of ZrO2 nanopowders at low temperature. *Materials Chemistry and Physics* **2009,** *117* (2-3), 455-459.

215. Arantes, T. M.; Mambrini, G. P.; Stroppa, D. G.; Leite, E. R.; Longo, E.; Ramirez, A. J.; Camargo, E. R., Stable colloidal suspensions of nanostructured zirconium oxide synthesized by hydrothermal process. *Journal of Nanoparticle Research* **2010,** *12* (8), 3105-3110.

216. Daturi, M.; Cremona, A.; Milella, F.; Busca, G.; Vogna, E., Characterisation of zirconia-titania powders prepared by coprecipitation. *Journal of the European Ceramic Society* **1998,** *18* (8), 1079-1087.

217. Valmalette, J. C.; Isa, M., Size effects on the stabilization of ultrafine zirconia nanoparticles. *Chemistry of Materials* **2002,** *14* (12), 5098-5102.

218. Folch, B.; Larionova, J.; Guari, Y.; Guerin, C.; Mehdi, A.; Reye, C., Formation of Mn3O4 nanoparticles from the cluster Mn12O12(C2H5COO)(16)(H2O)(3) anchored to hybrid mesoporous silica. *Journal of Materials Chemistry* **2004,** *14* (17), 2703-2711.

219. Carewska, M.; Appetecchi, G. B.; Cardellini, F.; Passerini, S., Synthesis of a bicontinuous electrically conductive nanocomposite via in-situ formation of RuO2 nanoparticles. *Solid State Ionics* **2001,** *139* (3-4), 211-218.

APPENDIX I

SUPPLEMENTAL FIGURES AND TABLES

Figure A.1 is a plot of the adsorption of DEEP onto amorphous silica (a-SiO_2) at varying temperatures. Taking into account the uncertainties in the measurements, the differences in the amount of DEEP adsorbed at a specific starting DEEP pressure were negligible with changes in temperature. Based on the vapor pressure results that were determined in this work and are presented for DEEP in Chapter 2, DEEP has the lowest vapor pressure out of all of the test compounds studied. Figure A.1 thus illustrates the challenges that are apparent when measuring the adsorption of exceptionally low vapor pressure OP compounds onto a-SiO_2 using the experimental apparatus developed for this work and described in Chapter 2.

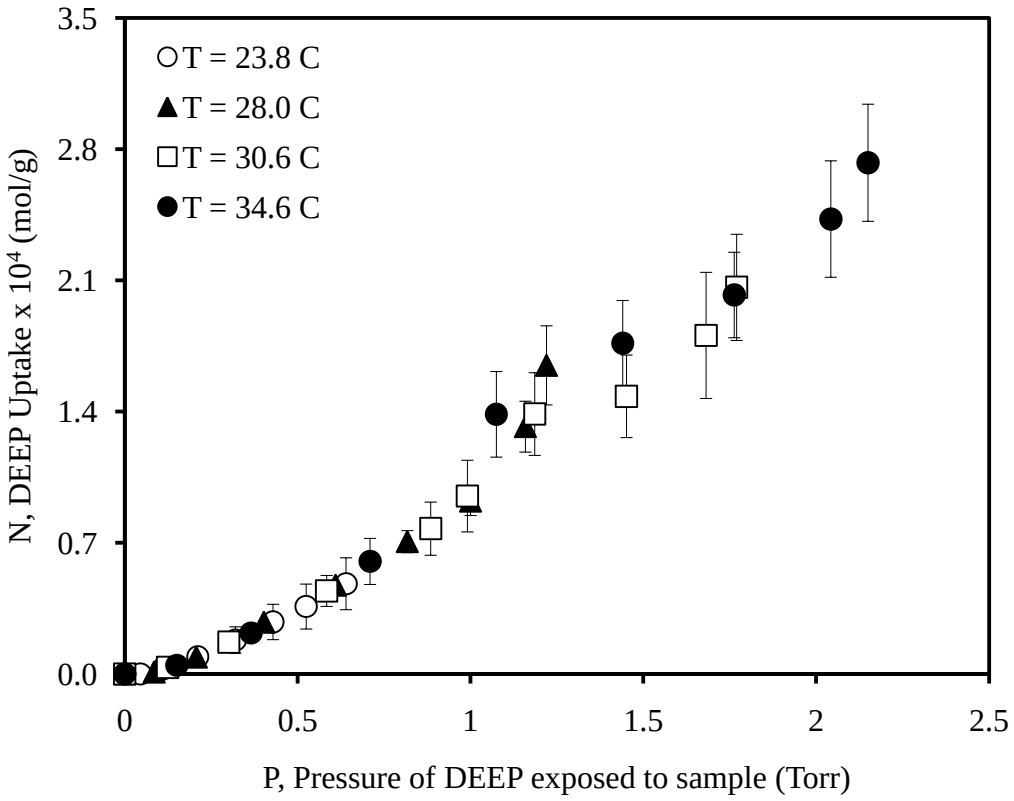

Figure A.1. a-SiO_2 adsorption of DEEP at 23.8 (○), 28.0 (▲), 30.6 (■), and 34.6 °C (●).

Tables A.1, A.2, and A.3 list the values for the adsorption isotherm parameters determined for a-SiO_2 adsorption of DMHP, DMMP, and TEP, respectively, at varying temperatures. The errors in the table represent one standard deviation. Adsorption isotherm parameters were determined for four multilayer isotherm models including the BET, the nBET, the BDDT, and the Huttig models. Multilayer isotherm models were chosen for the multilayer adsorption behavior observed experimentally, as shown in Chapter 2. The parameters were obtained using non-linear regression analyses performed with the Igor Pro 6.03 software. The chi-square values (χ^2) as well as results from F-tests are also presented in the tables.

Table A.1. Adsorption isotherm parameters (±1σ) and χ^2 for a-SiO_2 adsorption of DMHP

Adsorption Isotherm Model:		BET	nBET	BDDT	Huttig
Temperature	a_m	$1.61 \times 10^{-5} \pm 1.43 \times 10^{-6}$	$1.92 \times 10^{-4} \pm 1.05 \times 10^{-3}$	$3.16 \times 10^{-4} \pm 1.15 \times 10^{-3}$	$1.20 \times 10^{-3} \pm 2.55 \times 10^{-1}$
	K	10.1 ± 4.40	0.396 ± 2.30	□.171 ± 0.854	$9.57 \times 10^{-3} \pm 0.204$
23.8 °C	n	-	3.86 ± 10.0	2.27 ± 2.80	-
	q	-	-	3.30 ± 4.72	-
	χ^2	60.5	1.84	0.997	14.0
	P < 0.05 from F-test	No	Yes	Yes	Yes
	a_m	$1.86 \times 10^{-5} \pm 1.38 \times 10^{-6}$	$2.24 \times 10^{-4} \pm 1.22 \times 10^{-3}$	$2.61 \times 10^{-4} \pm 2.24 \times 10^{-3}$	$5.13 \times 10^{-3} \pm 3.21 \times 10^{-2}$
	K	$507 \pm 7.21 \times 10^{3}$	0.607 ± 3.60	0.515 ± 4.73	0.032 ± 0.205
28.0 °C	n	-	3.21 ± 9.80	3.97 ± 8.91	-
	q	-	-	$3.82 \times 10^{-17} \pm 4.53$	-
	χ^2	79.7	0.916	0.917	2.27
	P < 0.05 from F-test	No	Yes	Yes	Yes
	a_m	$1.88 \times 10^{-5} \pm 1.44 \times 10^{-6}$	$2.26 \times 10^{-4} \pm 1.10 \times 10^{-3}$	$2.45 \times 10^{-4} \pm 5.75 \times 10^{-4}$	$8.19 \times 10^{-3} \pm 7.06 \times 10^{-2}$
	K	17.7 ± 7.08	0.548 ± 2.80	0.398 ± 1.34	0.018 ± 0.153
30.6 °C	n	-	3.09 ± 7.82	2.19 ± 2.59	-
	q	-	-	2.70 ± 2.40	-
	χ^2	99.9	1.93	0.754	5.83
	P < 0.05 from F-test	No	Yes	Yes	Yes
	a_m	$1.10 \times 10^{-4} \pm 8.18 \times 10^{-4}$	$2.05 \times 10^{-4} \pm 7.16 \times 10^{-4}$	$3.81 \times 10^{-4} \pm 6.58 \times 10^{-4}$	$5.49 \times 10^{-4} \pm 1.94 \times 10^{-4}$
	K	$7.80 \times 10^{-3} \pm 6.65 \times 10^{-2}$	0.851 ± 3.24	0.030 ± 1.87	0.353 ± 0.147
34.6□ °C	n	-	2.72 ± 6.00	1.45 ± 1.27	-
	q	-	-	$29.3 \pm 1.80 \times 10^{3}$	-
	χ^2	918	2.□3	0.563	5.36
	P < 0.05 from F-test	No	Yes	Yes	Yes

Table A.2. Adsorption isotherm parameters (±1σ) and χ^2 for a-SiO_2 adsorption of DMMP

Temperature	Adsorption Isotherm Model:		BET	nBET	BDDT	Huttig
23.8 °C		a_m	$4.45 \times 10^{-5} \pm 1.44 \times 10^{-6}$	$7.67 \times 10^{-5} \pm 1.12 \times 10^{-5}$	$6.79 \times 10^{-5} \pm 2.18 \times 10^{-5}$	$5.12 \times 10^{-4} \pm 3.87 \times 10^{-4}$
		K	5.02 ± 0.864	1.20 ± 0.345	1.44 ± 0.766	0.243 ± 0.206
		n	-	8.56 ± 1.86	7.54 ± 1.48	-
		q	-	-	3.60 ± 5.35	-
		χ^2	245	5.72	5.51	48.96
		P < 0.05 from F-test	No	Yes	Yes	Yes
28.0 °C		a_m	$2.68 \times 10^{-5} \pm 1.97 \times 10^{-6}$	$3.20 \times 10^{-4} \pm 1.17 \times 10^{-3}$	$1.09 \times 10^{-4} \pm 1.64 \times 10^{-4}$	$1.20 \times 10^{-3} \pm 2.38 \times 10^{-3}$
		K	11.0 ± 3.87	0.330 ± 1.22	1.07 ± 1.90	0.119 ± 0.247
		n	-	2.82 ± 3.57	4.75 ± 2.17	-
		q	-	-	1.60 ± 8.08	-
		χ^2	126	2.71	3.29	8.31
		P < 0.05 from F-test	No	Yes	Yes	Yes
30.6 °C		a_m	$2.30 \times 10^{-5} \pm 1.86 \times 10^{-6}$	$1.09 \times 10^{-4} \pm 4.06 \times 10^{-5}$	$1.07 \times 10^{-4} \pm 7.89 \times 10^{-5}$	$3.62 \times 10^{-3} \pm 1.32 \times 10^{-2}$
		K	38.4 ± 30.2	1.73 ± 0.921	1.77 ± 1.69	0.050 ± 0.185
		n	-	5.89 ± 2.42	5.71 ± 7.67	-
		q	-	-	1.18 ± 12.8	-
		χ^2	67.0	3.19	3.24	2.60
		P < 0.05 from F-test	No	Yes	Yes	Yes
34.6 °C		a_m	$4.20 \times 10^{-5} \pm 4.93 \times 10^{-6}$	$3.87 \times 10^{-4} \pm 2.55 \times 10^{-3}$	$6.03 \times 10^{-4} \pm 2.62 \times 10^{-3}$	$6.76 \times 10^{-3} \pm 4.07 \times 10^{-2}$
		K	12.0 ± 3.99	0.572 ± 3.94	0.208 ± 2.03	0.036 ± 0.216
		n	-	2.77 ± 9.12	1.64 ± 2.81	-
		q	-	-	3.34 ± 19.2	-
		χ^2	56.0	1.05	0.417	2.45
		P < 0.05 from F-test	No	Yes	Yes	Yes

Table A.3. Adsorption isotherm parameters (±1σ) and χ^2 for a-SiO_2 adsorption of TEP

Temperature	Adsorption Isotherm Model:		BET	nBET	BDDT	Huttig
	23.8 °C	a_m	2.95 x 10^{-5} ± 1.95 x 10^{-6}	1.89 x 10^{-4} ± 9.21 x 10^{-4}	8.52 x 10^{-5} ± 2.36 x 10^{-4}	2.02 x 10^{-4} ± 1.20 x 10^{-4}
		K	2.68 ± 0.285	0.292 ± 1.47	0.641 ± 2.02	0.328 ± 0.206
		n	-	2.88 ± 4.05	2.95 ± 3.40	-
		q	-	-	2.14 ± 3.67	-
		χ^2	97.0	1.23	1.15	51.3
		P < 0.05 from F-test	No	Yes	Yes	Yes
	28.0 °C	a_m	2.93 x 10^{-5} ± 3.40 x 10^{-6}	2.55 x 10^{-4} ± 1.35 x 10^{-3}	4.09 x 10^{-4} ± 9.89 x 10^{-4}	2.66 x 10^{-3} ± 2.06 x 10^{-2}
		K	4.19 ± 1.25	0.323 ± 1.18	0.066 ± 0.341	0.044 ± 0.344
		n	-	4.00 ± 8.94	1.93 ± 1.05	-
		q	-	-	8.74 ± 26.0	-
		χ^2	61.5	8.66	4.78	22.6
		P < 0.05 from F-test	No	Yes	Yes	Yes
	30.6 °C	a_m	2.27 x 10^{-5} ± 1.95 x 10^{-6}	2.00 x 10^{-4} ± 8.27 x 10^{-4}	2.56 x 10^{-4} ± 7.77 x 10^{-4}	3.69 x 10^{-3} ± 9.33 x 10^{-3}
		K	4.15 x 10^{-3} ± 1.18 x 10^{-5}	0.658 ± 2.96	0.384 ± 1.95	0.041 ± 0.107
		n	-	3.13 ± 7.46	2.10 ± 3.63	-
		q	-	-	2.47 ± 5.60	-
		χ^2	382	3.35	1.77	9.63
		P < 0.05 from F-test	No	Yes	Yes	Yes
	34.6 °C	a_m	2.50 x 10^{-5} ± 3.25 x 10^{-6}	1.25 x 10^{-3} ± 8.85 x 10^{-6}	4.63 x 10^{-4} ± 1.65 x 10^{-3}	1.42 x 10^{-3} ± 4.55 x 10^{-3}
		K	7.52 ± 3.02	0.098 ± 1.17	0.029 ± 0.945	0.104 ± 0.345
		n	-	2.02 ± 10.6	?.54 ± 1.52	-
		q	-	-	20.8 ± 598	-
		χ^2	43.5	3.18	1.06	5.34
		P < 0.05 from F-test	No	Yes	Yes	Yes

Samples of hydrophilic silica containing surface hydroxyl groups and samples of alumina containing Al Lewis acid sites were exposed to four pure and gaseous OPs, DMHP, DMMP, DEEP, and TEP. The samples were probed before and after exposure to the OPs using Raman spectroscopy as discussed in Chapter 2. The Raman spectra for silica are shown in Figure A.2 to A.5 and the Raman spectra for alumina are shown in Figure A.6 to A.9. Exposure to the OPs resulted in multiple peak formations. The corresponding frequencies for the new peaks are shown in Figure A.2 to Figure A.9.

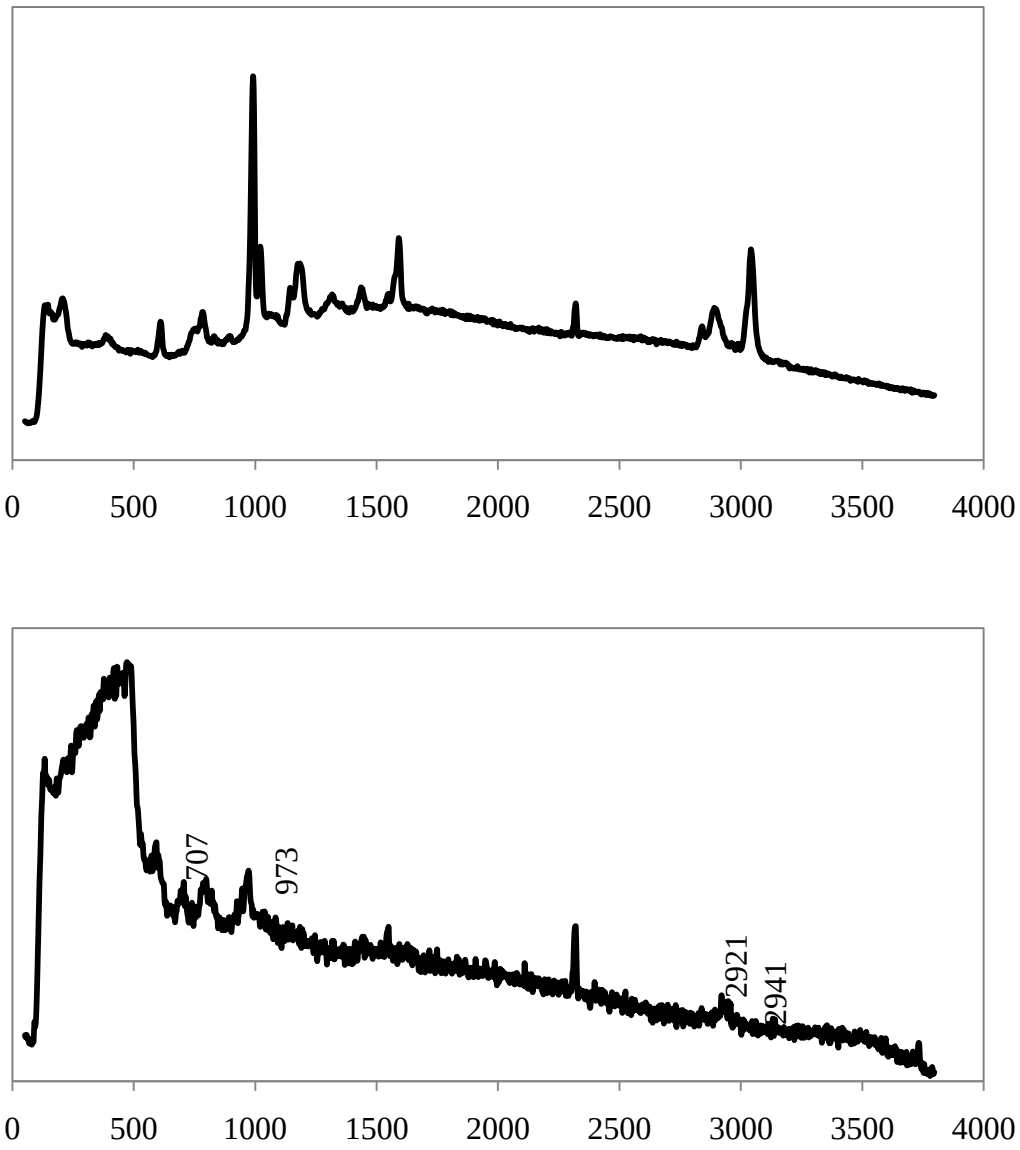

Figure A.2. Raman Spectra of SiO_2 (a) before and (b) after exposure to DMHP

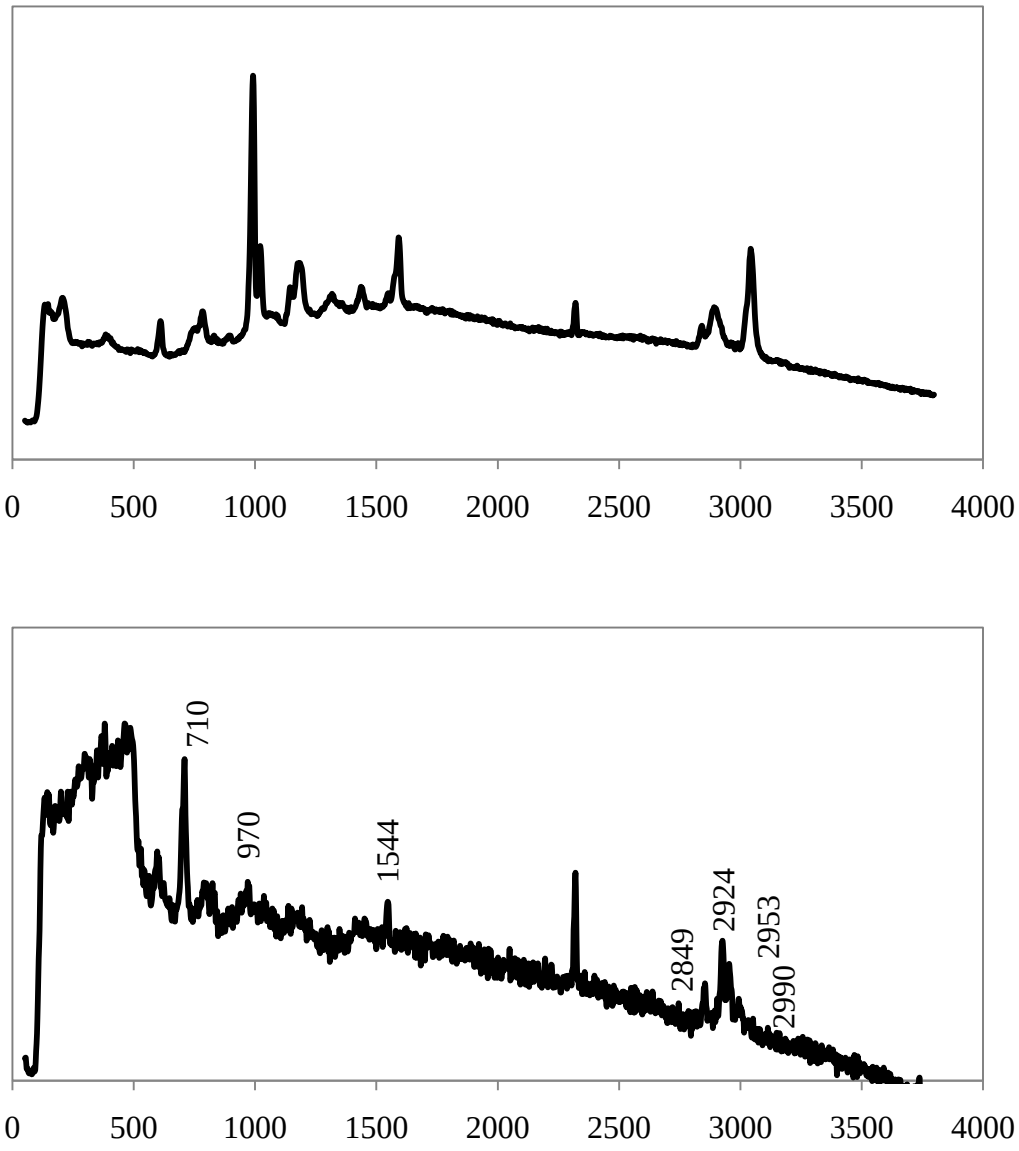

Figure A.3. Raman Spectra of SiO_2 (a) before and (b) after exposure to DMMP

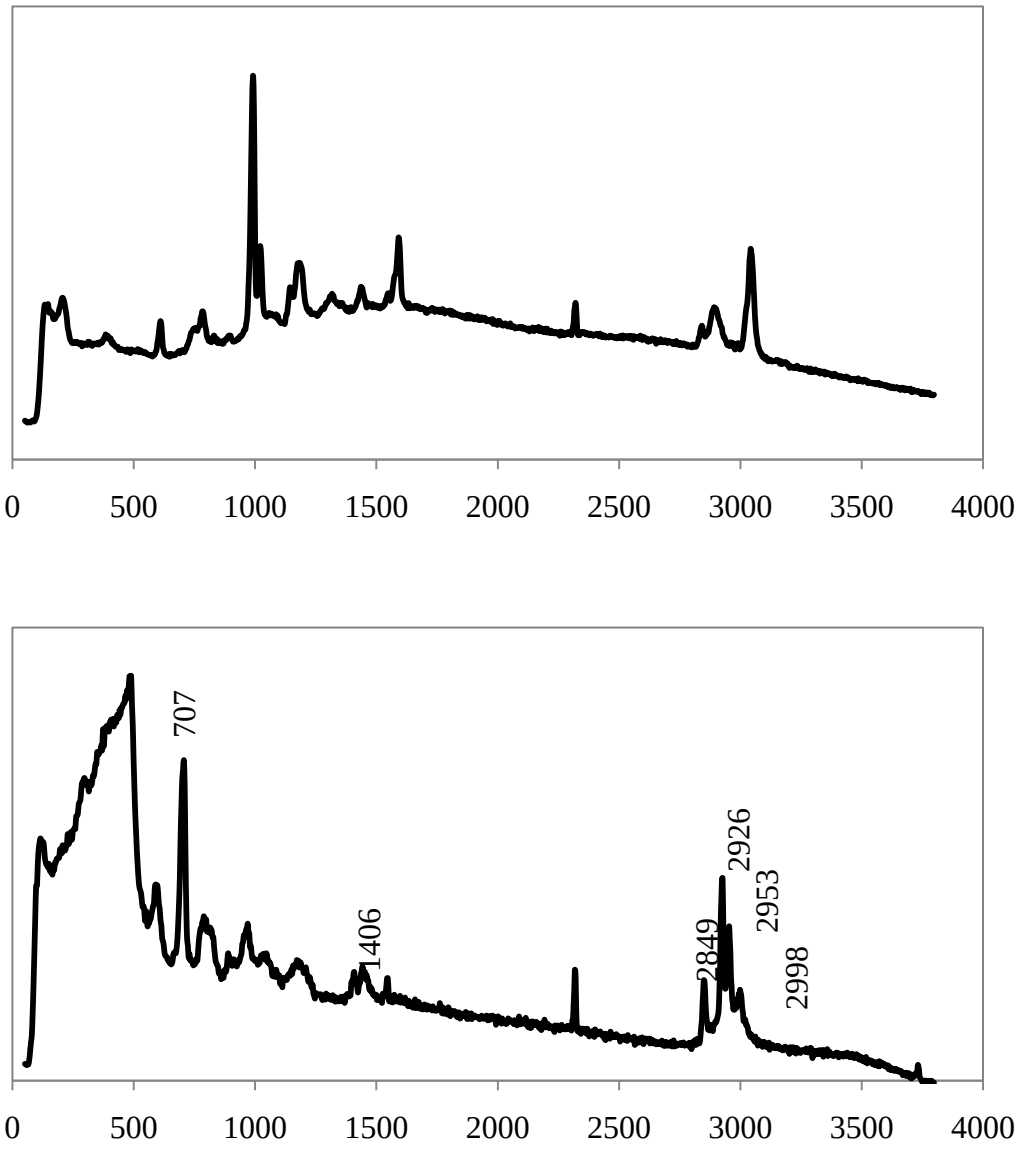

Figure A.4. Raman Spectra of SiO_2 (a) before and (b) after exposure to DEEP

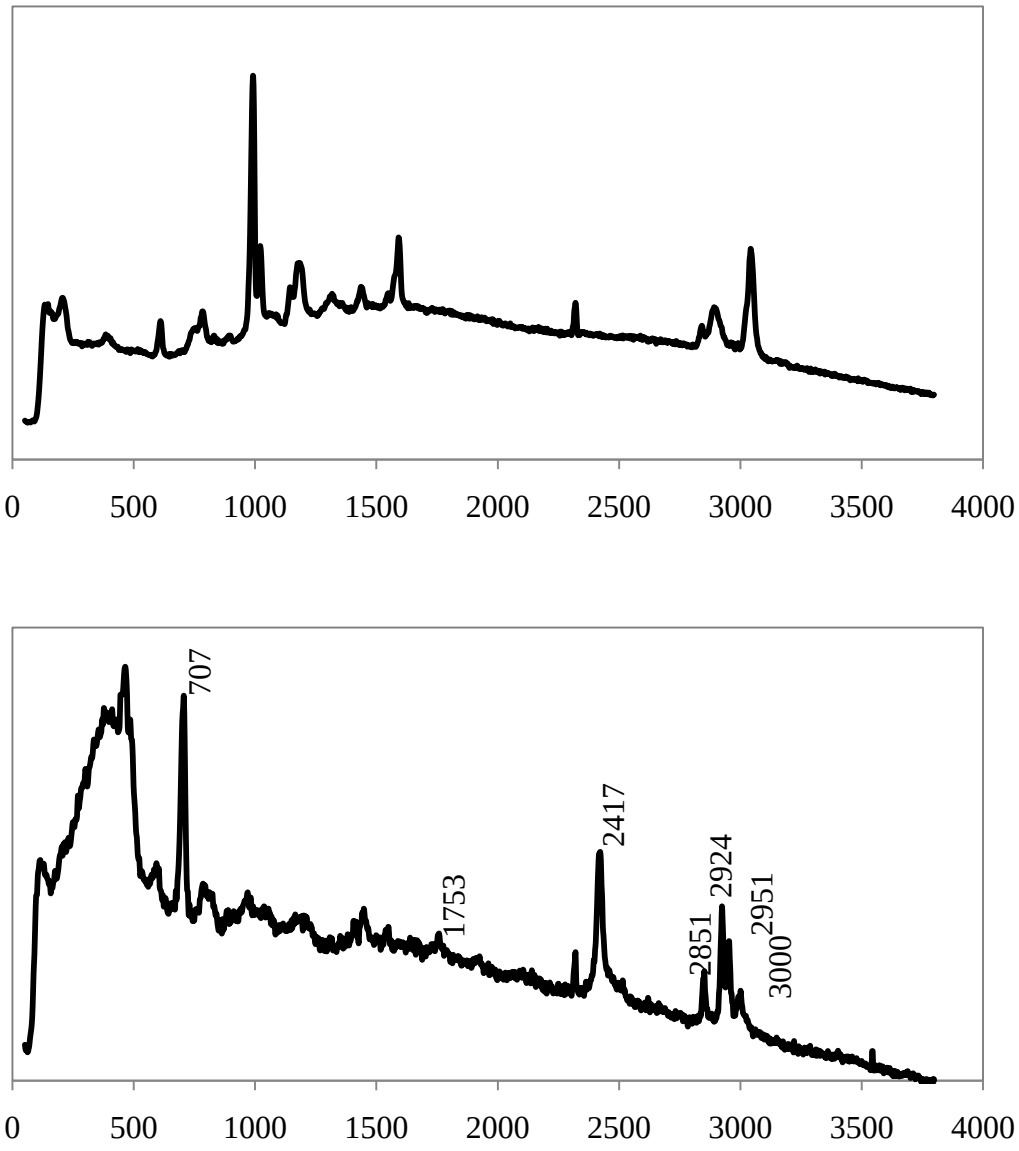

Figure A.5. Raman Spectra of SiO_2 (a) before and (b) after exposure to TEP

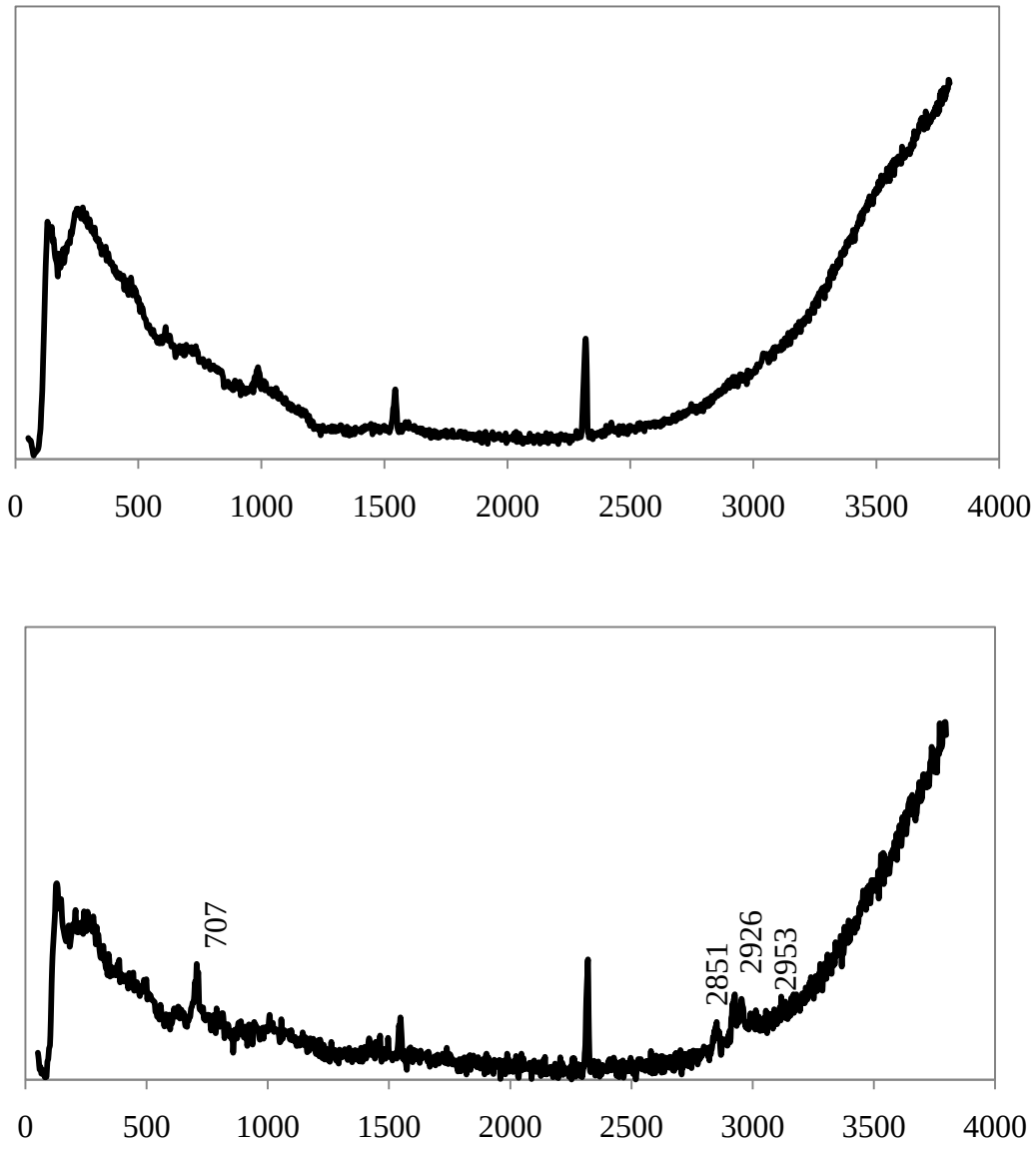

Figure A.6. Raman spectra of Al_2O_3 (a) before and (b) after exposure to DMHP

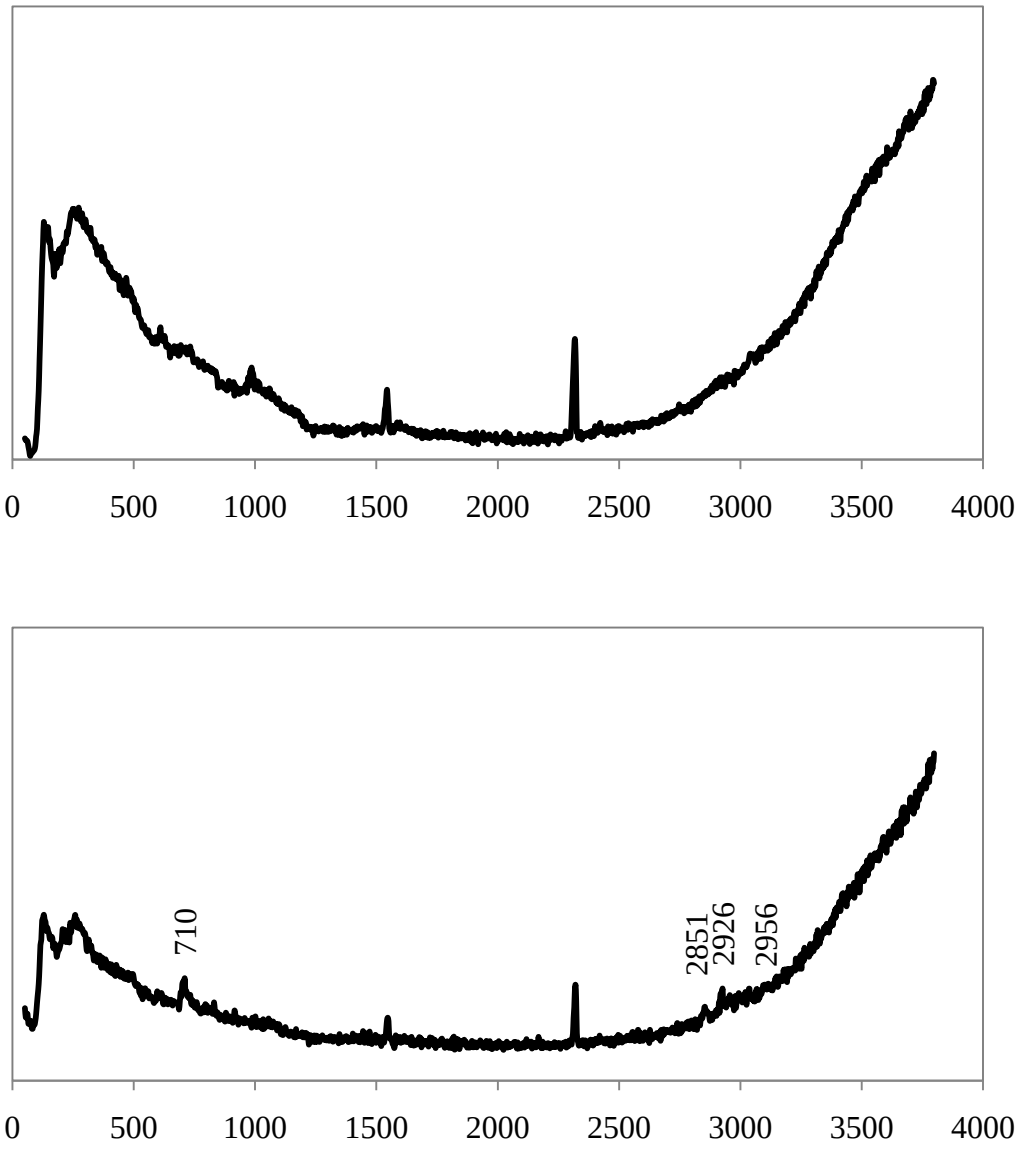

Figure A.7. Raman spectra of Al_2O_3 (a) before and (b) after exposure to DMMP

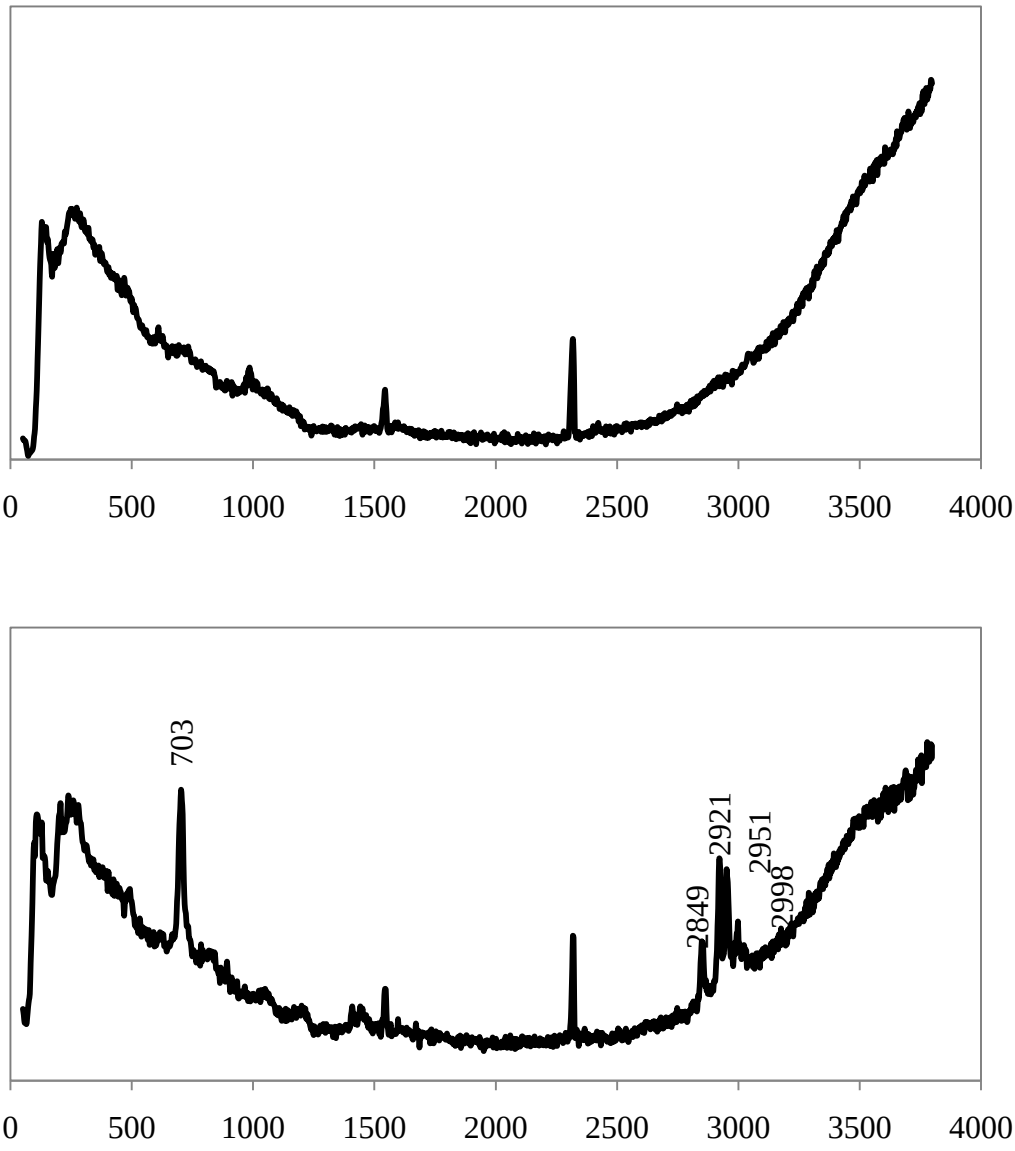

Figure A.8. Raman spectra of Al_2O_3 (a) before and (b) after exposure to DEEP

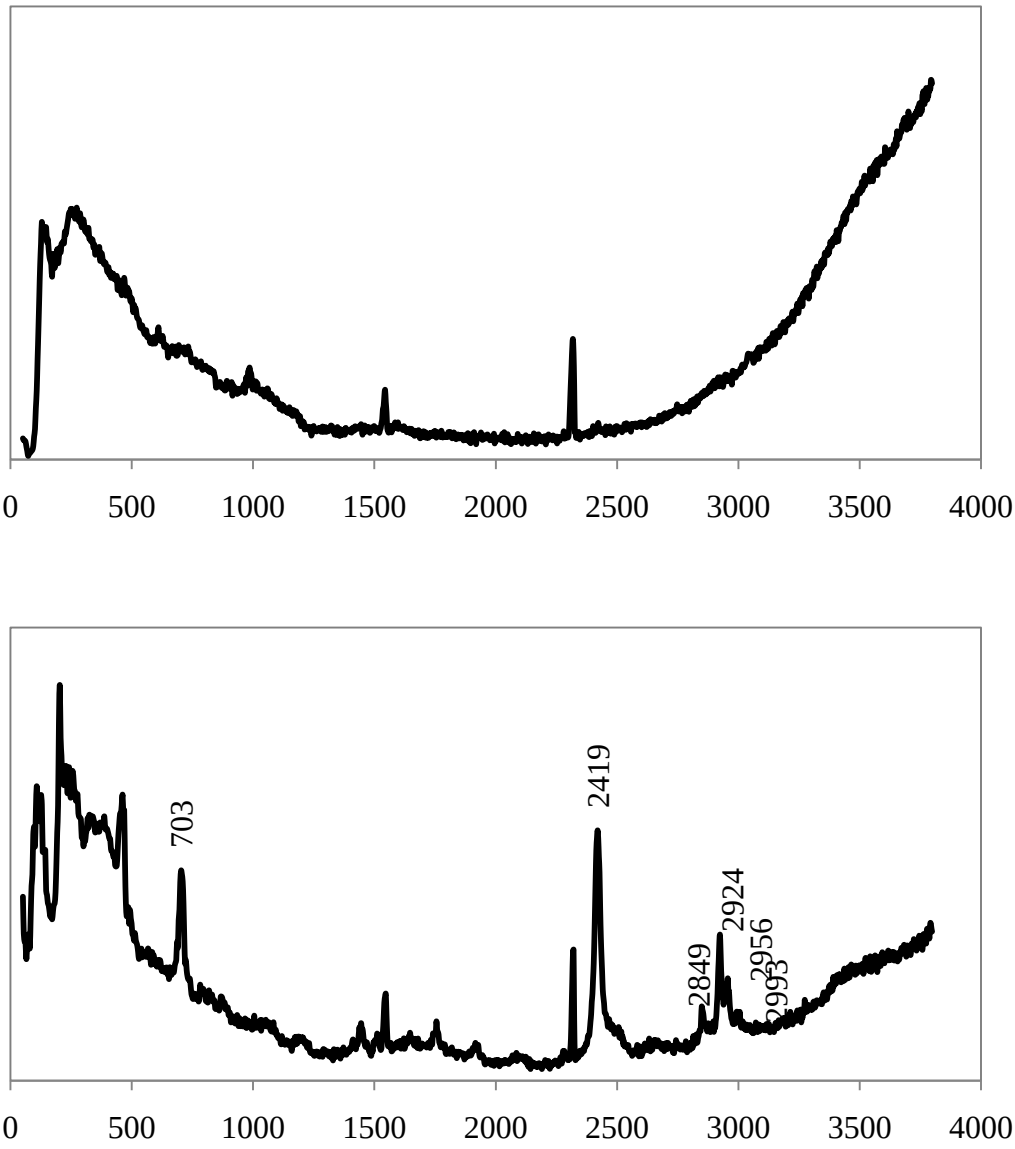

Figure A.9. Raman spectra of Al_2O_3 (a) before and (b) after exposure to TEP

Liquid samples of DMHP, DMMP, DEEP, and TEP were probed using Raman spectroscopy to determine the frequencies associated with the various bonds in the OP molecules. The Raman spectra for DMHP, DMMP, DEEP, and TEP are shown in Figure A.10 to Figure A.13, respectively. Note that the lower frequency peaks are obscured for TEP.

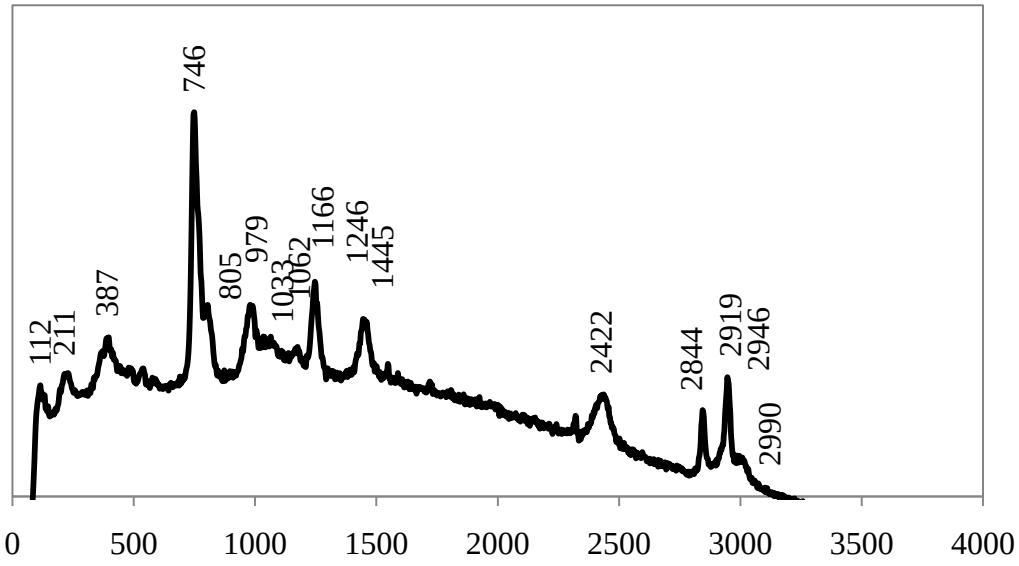

Figure A.10. Raman spectrum of liquid DMHP

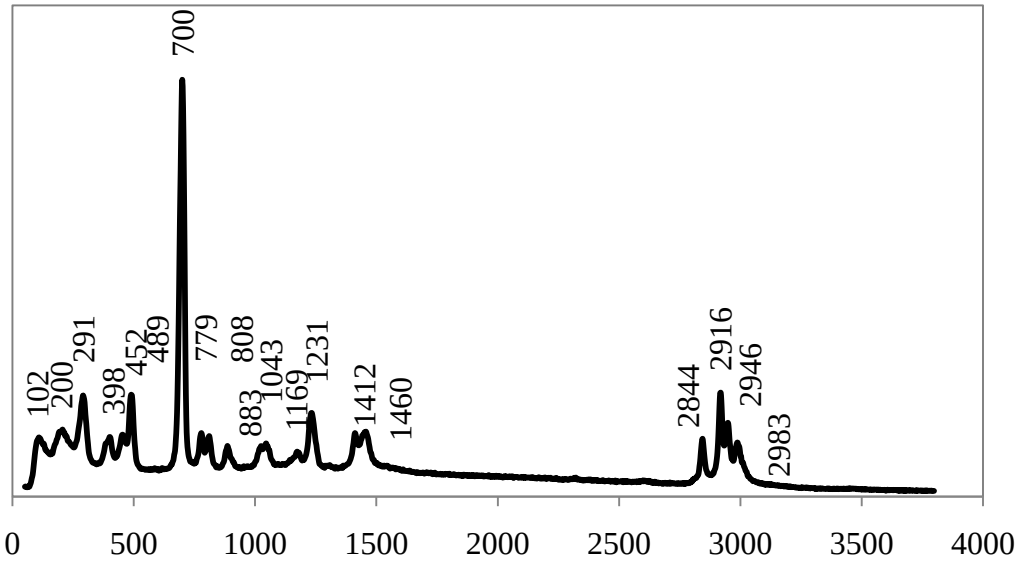

Figure A.11. Raman spectrum of liquid DMMP

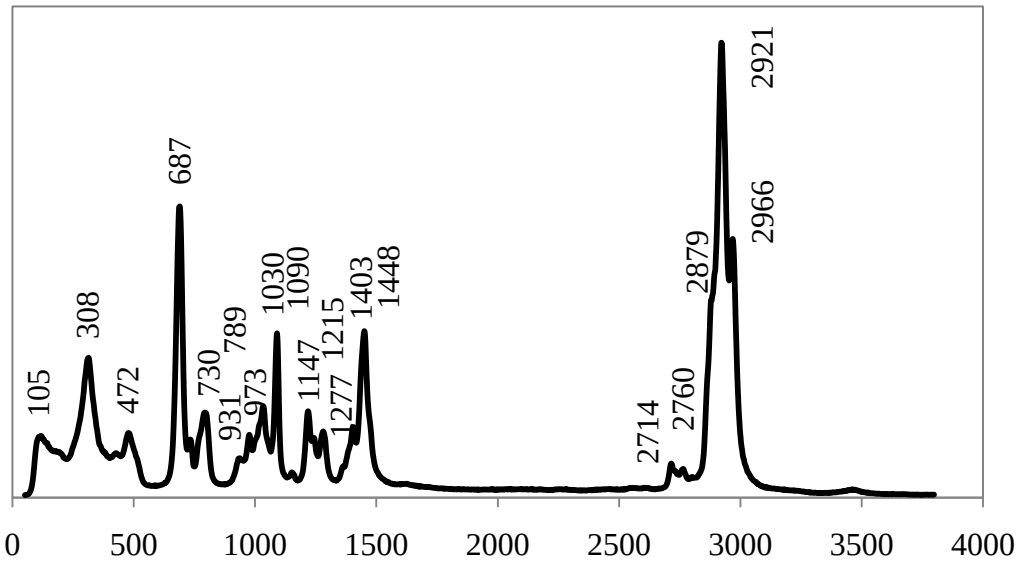

Figure A.12. Raman spectrum of liquid DEEP

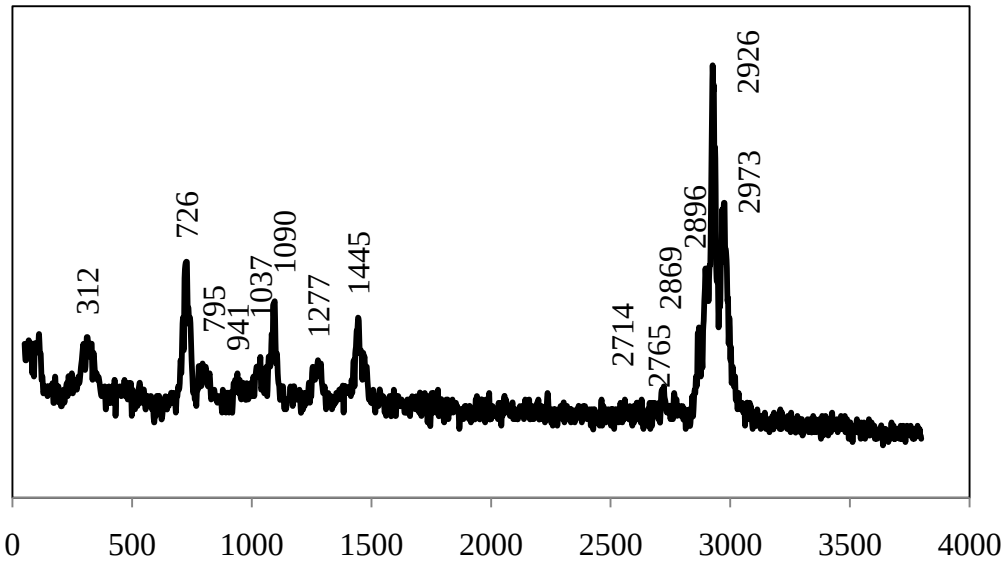

Figure A.13. Raman spectrum of liquid TEP

Table A.4 to A.8 lists the bond lengths and bond angle associated with the interaction between DMHP, DMMP, DMEP, DEEP, TEP, and both zirconia and alumina, respectively. Changes to the bond lengths and bond angles subsequent to adsorption are also presented. These results are predicted by the computational chemistry tool, Gaussian, as discussed in Chapter 3.

In Table A.4 to A.8, atoms which are affected by the bonding interactions with zirconia include the O atom (denoted O1) of the phosphonyl group (i.e. P=O1), the O atom (denoted O2) of the alkoxy groups (i.e. –O2-R), and the C atom (denoted C1) of the alkoxy group (i.e. $–O2-C1_xH_{2x+1}$). The bond lengths and bond angles of the m-Zr_8O_{16}-OP complexes (denoted Z-OP) and of the isolated OPs are shown in Tables A.4 to A.8. The changes resulting from the formations of the Z-OP complexes (denoted ΔZ) are proportional to the strengths of the interactions. A positive ΔZ associated with bond lengths indicates an enlargement of the bond, which in turn results in weakening of the bond as compared with the isolated OPs. Greater magnitudes for ΔZ associated with bond angles indicate greater stresses or strains on the intramolecular bonds, again, leading to the weakening of the structures of the OPs. For all five of the OPs investigated, the intramolecular bonds of the OP molecules are weakened by the interaction with m-Zr_8O_{16}.

Atoms which are affected by the bonding interactions with alumina include the O atom (denoted O1) of the phosphonyl (i.e. P=O1) group, the O atom (denoted O2)

of the alkoxy (i.e. –O2-R) groups, the C atom (denoted C1) of the alkoxy (i.e. –O2-$C1_xH_{2x+1}$) group, and the C atom (denoted C2) of the alkyl (i.e. –$C2_xH_{2x+1}$) group. The changes to bond lengths (denoted ΔA) and to the bond angles of the intramolecular bonds of the OPs due to the formations of the γ-Al_8O_{12}-OP complexes (denoted A-OP) are also shown in Tables A.4 – A.8.

In comparison to the interaction with m-Zr_8O_{16}, adsorption by γ-Al_8O_{12} led to both bond strengthening and weakening. In particular, the P-O2 bonds and for the cases where the C2 atoms are affected by the second H-bond interactions, the P-C2 bonds, are strengthened from the interactions. On the contrary, the P-O2 bonds were weakened for all of the OPs when interacted with m-Zr_8O_{16}. The P=O1 bonds are weakened for interaction with both oxides, however, the magnitude of the bond enlargements are greater for m-Zr_8O_{16} as compared with γ-Al_8O_{12}. In general, the extents to which the bond angles become stressed or strained are also greater for m-Zr_8O_{16} as compared with γ-Al_8O_{12}. Collectively, these results suggest that zirconia is likely to be superior to alumina for the decomposition of OP compounds.

Table A.4. Geometry of isolated DMHP, the adsorbed DMHP (Z-DMHP and A-DMHP), and the resulting distortions (ΔA and ΔZ)

	Z-DMHP	A-DMHP	DMHP	ΔZ	ΔA
bond length (Å)					
D(P=O1)	1.618	1.529	1.482	0.136	0.047
D(P-O2)	1.677	1.579	1.620	0.057	-0.041
D(O2-C1)	1.501	1.466	1.439	0.062	0.027
bond angles (°)				|ΔZ|	|ΔA|
(P-O2-C1)	125.5	124.0	120.0	5.5	4
(O1-P-O2)	111.2	113.7	114.9	3.7	1.2

Table A.5. Geometry of isolated DMMP, the adsorbed DMMP (Z-DMMP and A-DMMP), and the resulting distortions (ΔA and ΔZ)

	Z-DMMP	A-DMMP	DMMP	ΔZ	ΔA
bond length (Å)					
D(P=O1)	1.622	1.534	1.496	0.126	0.038
D(P-O2)	1.684	1.572	1.629	0.055	-0.057
D(O2-C1)	1.495	1.467	1.437	0.058	0.030
bond angles (°)				|ΔZ|	|ΔA|
(P-O2-C1)	124.3	124.5	120.0	4.3	4.5
(O1-P-O2)	109.4	116.1	113.9	4.5	2.2

Table A.6. Geometry of isolated DMEP, the adsorbed DMEP (Z-DMEP and A-DMEP), and the resulting distortions (ΔA and ΔZ)

	Z-DMEP	A-DMEP	DMEP	ΔZ	ΔA
bond length (Å)					
D(P=O1)	1.624	1.542	1.487	0.137	0.055
D(P-O2)	1.684	1.577	1.632	0.052	-0.055
D(O2-C1)	1.494	1.461	1.437	0.057	0.024
D (P-C2)	-	1.804	1.818	-	-0.014
bond angles (°)				|ΔZ|	|ΔA|
(P-O2-C1)	124.8	123.2	120.2	4.6	3
(O1-P-O2)	109.3	114.7	113.8	4.5	0.9
(O1-P-C2)	-	112.5	116.0	-	3.5

Table A.7. Geometry of isolated DEEP, the adsorbed DEEP (Z-DEEP and A-DEEP), and the resulting distortions (ΔA and ΔZ)

	Z-DEEP	A-DEEP	DEEP	ΔZ	ΔA
bond length (Å)					
D(P=O1)	1.630	1.543	1.487	0.143	0.056
D(P-O2)	1.681	1.575	1.631	0.050	-0.056
D(O2-C1)	-	1.479	1.447	-	0.032
D (P-C2)	-	1.805	1.819	-	-0.014
bond angles (°)				|ΔZ|	|ΔA|
(P-O2-C1)	-	123.3	120.5	-	2.8
(O1-P-O2)	109.8	114.6	113.9	4.1	0.7
(O1-P-C2)	-	112.1	115.7	-	3.6

Table A.8. Geometry of isolated TEP, the adsorbed TEP (Z-TEP and A-TEP), and the resulting distortions (ΔA and ΔZ)

	Z-TEP	A-TEP	TEP	ΔZ	ΔA
bond length (Å)					
D(P=O1)	1.614	1.528	1.483	0.131	0.045
D(P-O2)	1.659	1.568	1.607	0.052	-0.039
D(O2-C1)	-	1.483	1.450	-	0.033
bond angles (°)				|ΔZ|	|ΔA|
(P-O2-C1)	-	124.8	119.2	-	5.6
(O1-P-O2)	111.8	114.8	116.3	4.5	1.5

Tables A.9 to A.13 lists the charges of the atoms in the OPs, DMHP, DMMP, DMEP, DEEP, and TEP, and charges of the atoms on the surface of zirconia and alumina, respectively. The resulting changes to the charges of the atom due to adsorption are also listed. The total charge transfers associated with the interactions are summed and provide a quantitative indication of the strength of interaction between the OPs and the surfaces (i.e. the larger the magnitude of charge transfer, the stronger the interaction) as discussed in Chapter 3.

The surface atoms involved in charge transfer includes the Zr Lewis acidity, the Al Lewis acidity, the O atoms involved with hydrogen bonding interactions (denoted Oa) with the alkoxy groups, and the O atoms involved with hydrogen bonding interactions (denoted Ob) with the alkyl groups. For interactions with m-Zr_8O_{16}, the chemical bond formations resulted in an increase on the positive charge of the Zr atom and a more negative charge for the O1 atom. The hydrogen bonding interaction resulted in an increase on the positive charge of the bonding H atom and a more negative charge for the surface Oa atom. These charge changes resulting from electron transfers are proportional to the strengths of the bonds. In all cases, the electron transfers with the Zr atom is greater in magnitude than the electron transfers with the surface Oa atom, thereby indicating that the bond formation with the Zr site is the primary mechanism for stabilization of the OP interactions. Similarly, these trends were also observed for the Al site.

In comparing the charge transfers between the OPs and m-Zr_8O_{16} to the charge transfers with γ-Al_8O_{12}, in particular for the O1 atom and the H atoms which

participate directly in the bonding interactions, the magnitude of the total charge transfer is greater for m-Zr_8O_{16} as compared with γ-Al_8O_{12} for all of the OPs investigated. The observed trend could be attributed to the charges of the native Zr and Al Lewis acid sites. The Zr and Al Lewis acidities carry positive charges of 1.686 and 1.102 e, respectively. Larger positive charges on the metal centers are associated with stronger bonding capability. This result suggests that Zr sites form stronger interactions with the OPs than Al sites. It should be noted that in all cases except for the m-Zr_8O_{16} interactions with DEEP and TEP where dissociation occurred, the adsorbed OPs carry a net positive charge. This indicates that electrons are transferred from the OP molecules to the oxides, which is in agreement with the nature of the active sites (i.e. electron acceptors).

In general, the magnitude of the total charge transfers with the O1 and H atoms increases with the basicity (i.e. the negative charge of the O1 atom) of the isolated OPs with the exception of the most basic OP (i.e. TEP). The energetic associated with the interactions are subsequently discussed and can be expected to follow the same trend.

Table A.9. Charges of the of isolated DMHP, the adsorbed DMHP (Z-DMHP and A-DMHP), the surface atoms, and the resulting changes in charge (ΔA and ΔZ)

	Charges of the OP and surface atoms (e)								
	Z-DMHP	A-DMHP	DMHP	Z	A	ΔZ	ΔA	|ΔZ|	|ΔA|
OP compound									
P	1.290	1.202	1.024	-	-	0.266	0.178		
O1	-0.838	-0.601	-0.559	-	-	-0.279	-0.042	0.279	0.042
O2	-0.548	-0.509	-0.526	-	-	-0.022	0.017		
C1	-0.435	-0.278	-0.222	-	-	-0.213	-0.056		
H (of C1)	0.312	0.263	0.188	-	-	0.124	0.075	0.124	0.075
Surface									
Zr or Al	1.824	1.053	-	1.686	1.102	-0.138	0.049		
Oa	-0.776	-0.706	-	-0.723	-0.673	0.053	0.033		
						total charge transfer		0.403	0.117

Table A.10. Charges of the of isolated DMMP, the adsorbed DMMP (Z-DMMP and A-DMMP), the surface atoms, and the resulting changes in charge (ΔA and ΔZ)

	Charges of the OP and surface atoms (e)								
	Z-DMMP	A-DMMP	DMMP	Z	A	ΔZ	ΔA	|ΔZ|	|ΔA|
OP compound									
P	1.394	1.297	1.109	-	-	0.285	0.188		
O1	-0.871	-0.631	-0.568	-	-	-0.303	-0.063	0.303	0.063
O2	-0.547	-0.502	-0.537	-	-	-0.010	0.035		
C1	-0.433	-0.278	-0.219	-	-	-0.214	-0.059		
H (of C1)	0.286	0.270	0.187	-	-	0.099	0.083	0.099	0.083
Surface									
Zr or Al	1.824	1.055	-	1.686	1.102	-0.138	0.047		
Oa	-0.761	-0.708	-	-0.723	-0.673	0.038	0.035		
					total charge transfer			0.402	0.146

Table A.11. Charges of the of isolated DMEP, the adsorbed DMEP (Z-DMEP and A-DMEP), the surface atoms, and the resulting changes in charge (ΔA and ΔZ)

	Charges of the OP and surface atoms (e)								
	Z-DMEP	A-DMEP	DMEP	Z	A	ΔZ	ΔA	|ΔZ|	|ΔA|
OP compound									
P	1.403	1.346	1.133	-	-	0.270	0.213		
O1	-0.882	-0.651	-0.567	-	-	-0.315	-0.084	0.315	0.084
O2	-0.553	-0.510	-0.548	-	-	-0.005	0.038		
C1	-0.432	-0.266	-0.220	-	-	-0.212	-0.046		
H (of C1)	0.293	0.248	0.163	-	-	0.130	0.085	0.13	0.085
C2	-	-0.540	-0.473	-	-	-	-0.067		
H (of C2)	-	0.273	0.178	-	-	-	0.095		0.095
Surface									
Zr or Al	1.812	1.047	-	1.686	1.102	-0.126	0.055		
Oa	-0.766	-0.705	-	-0.723	-0.673	0.043	0.032		
Ob	-	-0.706	-	-	-0.673	-	0.033		
						total charge transfer		0.445	0.264

Table A.12. Charges of the of isolated DEEP, the adsorbed DEEP (Z-DEEP and A-DEEP), the surface atoms, and the resulting changes in charge (ΔA and ΔZ)

	Charges of the OP and surface atoms (e)								
	Z-DEEP	A-DEEP	DEEP	Z	A	ΔZ	ΔA	|ΔZ|	|ΔA|
OP compound									
P	1.416	1.349	1.134	-	-	0.282	0.215		
O1	-0.873	-0.655	-0.570	-	-	-0.303	-0.085	0.303	0.085
O2	-0.578	-0.520	-0.556	-	-	-0.022	0.036		
C1	-0.179	-0.089	-0.040	-	-	-0.139	-0.049		
H (of C1)	0.301	0.239	0.160	-	-	0.141	0.079	0.141	0.079
C2	-	-0.539	-0.473	-	-	-	-0.066		
H (of C2)	-	0.270	0.177	-	-	-	0.093		0.093
Surface									
Zr or Al	1.784	1.050	-	1.686	1.102	-0.098	0.052		
Oa	-0.781	-0.705	-	-0.723	-0.673	0.058	0.032		
Ob	-	-0.705	-	-	-0.673	-	0.032		
						total charge transfer		0.444	0.257

Table A.13. Charges of the of isolated TEP, the adsorbed TEP (Z-TEP and A-TEP), the surface atoms, and the resulting changes in charge (ΔA and ΔZ)

	Charges of the OP and surface atoms (e)								
	Z-TEP	A-TEP	TEP	Z	A	ΔZ	ΔA	|ΔZ|	|ΔA|
OP compound									
P	1.536	1.386	1.198	-	-	0.338	0.188		
O1	-0.858	-0.626	-0.591	-	-	-0.267	-0.035	0.267	0.035
O2	-0.546	-0.510	-0.515	-	-	-0.031	0.005		
C1	-0.169	-0.104	-0.038	-	-	-0.131	-0.066		
H (of C1)	0.272	0.245	0.171	-	-	0.101	0.074	0.101	0.074
Surface									
Zr or Al	1.798	1.050	-	1.686	1.102	-0.112	0.052		
Oa	-0.787	-0.706	-	-0.723	-0.673	0.064	0.033		
						total charge transfer		0.368	0.109